SURFACE WAVE TECHNIQUES FOR THE STUDY OF ENGINEERING

STRUCTURES AND MATERIALS

by

JOSEPH YUK FU CHEN

Submitted for the Degree of Doctor of Philosophy

at

The University of Aston in Birmingham

May 1979

SURFACE WAVE TECHNIQUES FOR THE STUDY OF ENGINEERING STRUCTURES AND MATERIALS

by

JOSEPH YUK FU CHEN

Submitted for the Degree of Doctor of Philosophy

at

The University of Aston in Birmingham

May 1979

PREFACE

The contents of Chapters 2 and 6 of this thesis have been accepted for the following publications:

"A model for the behaviours of Mechanical Resonators suitable for Computer Graphics"

J.F.W.Bell, J.Y.F.Chen, S.A.C.Sanders, D.C.Simpson

The 3rd British Conference on Teaching of Vibration and Noise, July 1979.

"Elastic Constants of Refractory Materials at High Temperatures"

J.F.W.Bell, J.Y.F.Chen, K.R.Chaplain

The American Journal of N.D.T., June 1979.

ACKNOWLEDGEMENTS

SURFACE WAVE TECHNIQUES FOR THE STUDY OF

ENGINEERING STRUCTURES AND MATERIALS

J. Y. F. Chen

Doctor of Philosophy 1979

Summary

A wire drive pulse echo method of measuring the spectrum of solid bodies is described. Using an 's' plane representation, a general analysis of the transient response of such solids has been carried out. This was used for the study of the stepped amplitude transient of high order modes of disks and for the case where there are two adjacent resonant frequencies. The techniques developed have been applied to the measurement of the elasticities of refractory materials at high temperatures.

In the experimental study of the high order in-plane resonances of thin disks it was found that the energy travelled at the edge of the disk and this initiated the work on one dimensional Rayleigh waves. Their properties were established for the straight edge condition by following an analysis similar to that of the two dimensional case. Experiments were then carried out on the velocity dispersion of various circuits including the disk and a hole in a large plate - the negative curvature condition. Theoretical analysis established the phase and group velocities for these cases and experimental tests on aluminium and glass gave good agreement with theory. At high frequencies all velocities approach that of the one dimensional Rayleigh waves.

When applied to crack detection it was observed that a signal burst travelling round a disk showed an anomalous amplitude effect. In certain cases the signal which travelled the greater distance had the greater amplitude. An experiment was designed to investigate the phenomenon and it was established that the energy travelled in two modes with different velocities. It was found by analysis that as well as the Rayleigh surface wave on the edge, a second mode travelling at about the shear velocity was excited and the calculated results gave reasonable agreement with the experiments.

SURFACE WAVE, MODE PROPAGATION, MATERIAL CHARACTERISATION

CONTENTS

from the spectrum. Because of this importance, the coupling term (expressed as a 'Q' factor) has been calculated as described in Chapter 2 from the theoretical equations for the radial and tangential components of vibration of a variety of modes. Of these the radial expansion and the three nodal diameter distortion modes are particularly important as they are the best pair for elasticity measurements. Unfortunately, in metals, the frequencies are sufficiently close to prevent direct measurement and only by comparison of theoretical responses obtained from the model with those obtained experimental can true values of the frequency be obtained.

To perform the inversion of this 's' plane model with several complex pole and zero pairs is a formidable task. However, the coupling term is very small compared to mode frequencies and this enables the inversion to be made by using an on-line mini-computer which provides an output to the graphical display unit. The pattern normally takes 1~3 minutes to plot and can be compared directly to the oscilloscope display. This computer programme was used to resolve the adjacent frequency modes referred to above providing an improved method of measuring Poisson's ratio. In later investigation, it was found that anisotropy of the material results in split modes and again this technique was used to resolve them.

In Chapter 6, this technique is extended to measure the elastic constants of materials at high temperatures since the electronic equipment is remote from the resonator. Various

materials, for example, hot-pressed silicon nitride, silica, graphite etc, had been studied.

When investigating high order in-plane modes on disks, it was at once apparent that these were equivalent to two surface waves travelling in opposite directions. It was decided to investigate these one dimensional waves in more detail. For the case of a straight edge, a double wire drive was used. The results showed the characteristic fall off with depth of the vertical and horizontal components of displacement and a velocity equal to that of one dimensional Rayleigh wave. The wave of this type was first described by Mason and Ash in their micro-sound waveguides. A theoretical and experimental discussion of one dimensional Rayleigh wave is given in Chapter 3.

One dimensional surface waves also exists on edges with curvature but are dispersive. The dispersion can be described by the use of phase and group velocities. Theoretical and experimental studies of wave propagating on the edges of disks, holes, ends of cylindrical shell are presented in Chapter 4. A simple polynominal expression is obtained to show how the wave velocities converge to their asymptotic values.

The edge surface waves have been applied successfully to detect and locate very shallow surface cracks. In studying signal amplitude, a crack was produced on the edge of a disk giving two echoes, one having travelled a greater distance than the other. An unusual phenomenon was observed; the wave travelling a longer distance has a larger amplitude than that

of a short distance. The phenomenon occurs because the
waves leaving the drive source can be divided into several
modes which travel at different velocities but all modes are
confined to the surface. This effect appears on positive
curvature only. The existence of high order modes is
analogous to the 'whispering gallery effect' first described
by Lord Rayleigh using a ray theory. A study of additional
roots in the disk frequency equation and their longitudinal
and shear potentials gives the velocity and fall off
characteristic with depth. The waves travel at different
velocities and result in a periodic increase and decrease in
amplitude analogous to a beating effect. Comparison of
experimental and theoretical echo amplitude gave good
qualitative agreement. This effect is discussed in Chapter 5.

Another phenomenon exhibiting very similar characteristic
in nature to that of surface wave is end resonance. The
propagation of this wave is associated with the complex
propagation constants and its precise eigenvalues for strips
were obtained by Bell and Karlmarczie. A 45° drive to the
width end of a strip excites the end resonance mode efficiently.
Their results were normalised, as is usual to the shear
velocity in the material. When normalised to the one
dimensional Rayleigh wave velocity the eigenvalues obtained
were much less dependent on Poisson's ratio. This indicated
that all end resonance phenomena might better be investigated
by a surface wave approach . Measurement of elastic constants
based on the end resonance is proposed and included in
Chapter 6.

CHAPTER 2

A MODEL FOR THE TRANSIENT BEHAVIOUR OF DISTRIBUTED

MECHANICAL RESONATORS

CHAPTER 2

A MODEL FOR THE TRANSIENT BEHAVIOUR OF DISTRIBUTED

MECHANICAL RESONATORS

2.1 Introduction

The pulse-echo technique, originally designed for

Ultrasonic Thermometry[1], can also be used to obtain the

resonant frequency spectrum of solid objects, the geometrical

forms used for material characterisation are thin disks (driven

in plane) or rods driven longitudinally. A schematic diagram

of the pulse-echo system is shown in Fig. 2.1. From the

known spectrum of an isotropic disk, Young's modulus and

Poisson's ratio can be obtained by comparing the mode

frequencies which are governed by different elastic constants

such as the plate and longitudinal modulus. These measurements

can be made with high precision. A long thin line is used to

couple the magnetostrictive transducer to the resonator. This

gives a large separation between the resonator and the signal

equipments and enables measurement to be carried out over a

wide temperature range[2].

To analyse the echo pattern, a mathematical model of a

simple lossless line resonator has been developed by Sharp[3].

This is, in effect, a lumped circuit representation of each

resonance and makes use of a dominant pole in the plane of the

Laplace transform variable 's'. The position of the pole is

determined by the frequency of the resonance being considered

and its coupling to the line. A typical 's' plane diagram

and echo plot using this model are shown in Figs. 2.2 and 2.3. The early part of the echo in Fig. 2.3 shows the transient interaction with the drive frequency and the natural resonant frequency, the late part of the echo shows the approach to the steady state situation. However, it has been observed experimentally that when high order modes are excited, the echo pattern develops a 'stepped' change of amplitude while a computer plot using this simple model gives a pure exponential echo pattern and the stepping effect does not appear. The stepping effect is dominated by the fundamental mode: the step interval for any mode corresponds to the period of the fundamental and the energy transit time. Using this approach, a more detailed 's' plane model for high order modes where each resonance is represented by a pole and zero pair has been developed. With approximation, the complete inversion is possible and shows good agreement with experimental echo patterns.

The spectrum of even simple bodies can be very extensive. Close resonant modes are frequently encountered, particularly when the material is anisotropic and this results in a complex echo pattern which changes rapidly in form with the drive frequency. Typically two closely associated resonances have been analysed by considering the two pairs of poles and zeros. Comparison of the theoretical computer plot and the experimental pattern enables the values of resonant frequencies to be determined.

This 's' plane model can be used with a resonator other than a rod provided that the appropriate coupling value (β)

and the eigenvalues of the vibration modes are known. The model developed by Sharp is obtained by using the mechanical impedance approach from the ratio of force to velocity and expressing the impedance in terms of the coupling and relaxation term in Laplacian form. Consider the thin disk of which the vibrations are two dimensional. To obtain the impedance expression using the previous method would demand laborious mathematical manipulation to express the force and velocity functions. In this case, the coupling factor is obtained in terms of the equivalent mass of a resonant system by employing a Rayleigh's energy method[4] involving energy considerations alone. This method requires only the eigenfunction expression for the velocity function. An 's' plane model is thus developed. The result shows that all the low order distortion modes (nodal diameters only) have the same order of coupling with a small dependence on Poisson's ratio. For metals ($\sigma=0.3$), the changes in coupling value are insignificant.

The echo plots can be obtained from an 'on line' mini-computer graphic unit which allows a direct comparison with the experimental display.

2.2 The Echo Technique and Magnetostrictive Transducer

As shown in Fig. 2.1, a magnetostrictive launcher is used to transmit and receive a burst of high frequency longitudinal stress waves. The acoustic line is made of nickel wire or telcoseal (nickel - iron alloy). The number of oscillations is selected to allow sufficient information to be extracted. The lines are annealled and stretched to minimize the attenuation in the line material and scattering from the grain boundaries. The effect of magnetostriction is quadratic and requires a standing magnetic bias, or where space is limited, a solenoid, concentric with the launching coil, driven by a constant current source is used. The coil design enables full use of the characteristic to be obtained with a swing ±15V. In general, this gives an echo signal to the order of 0.5 volt which is sufficiently strong for electronic noise to be negligible. The presence of the spurious echoes from the line arising from kinks, supports and grains, are the factors which ultimately limit the accuracy. The line is made sufficiently long to avoid standing waves. At the other extreme, the length should not produce the problem of excessive attenuation. Within these limits, line lengths are chosen to suit the physical environment. Typically, a 2 metre line can have a burst of 40 oscillations at 50 kHz before standing waves occur.

For a single open ended launcher, the centre of the coil is positioned $\lambda/4$ from the end of the wire to make use of the

first reinforcement between the forward and reflected wave. This, in effect, doubles both the transmitted and received signal.

The Magnetostrictive Driver, using digital TTL circuits throughout generates a burst of variable frequency pulses in the range of 10 kHz - 1 MHz. The digital techniques employed enable the number of oscillations in the burst and their repetition rate to be preselected. The coil is tuned by means of a decade capacitor.

Resonance occurs when the transmitted frequency is exactly equal to the mode frequency of the resonator. The echo in this situation produces a distinctive, phase sensitive 'null' providing a precise setting of frequency.

The resonator itself can have a variety of geometrical forms which depend upon the parameter to be measured and will also be determined by the availability of empirical or theoretical solutions.

The characteristic of the echo will be discussed in the next section.

2.3 A Rod Resonator Using the Transmission Line Theory

In this analysis, a low impedance transmission line is considered to be terminated by a line resonator of much larger diameter. Plane waves are assumed given the familiar harmonic resonator spectrum. The echo arises from the reflection of a burst of oscillations at the resonator. Only longitudinal propagation is considered. A suitable linearized equation of motion[5] for propagation is given in equation (2.1).

$$\frac{\ddot{u}}{C_o^2} = \frac{\partial^2 u}{\partial z^2} + \frac{H}{C_o^2} \frac{\partial^2 u}{\partial z^2} \qquad (2.1)$$

H is the relaxation term which accounts for material losses. For constant loss angle, H is inversely proportional to frequency.

C_o is the rod velocity of longitudinal plane waves and equals $(E/\rho)^{\frac{1}{2}}$. In this case, C_1 refers to the line and C_2 to the resonator.

Equation (2.1) has the solution of

$$u(z) = (A \exp j(-q_1 z) + B \exp j(q_1 z)) \exp(j\omega t) \qquad (2.2)$$

This is similar to the electrical transmission line theory which represents two waves travelling in opposite directions with the complex propagation constant which is given by equation (2.3)

$$q_1 = \frac{-\omega^2}{C_o^2 + j\omega H} \doteqdot -\left(\frac{2\pi}{\lambda}\right)^2 \left(1 - j\frac{\omega H}{C_o^2}\right) \qquad (2.3)$$

To describe the echo the analysis used the concept of mechanical impedance defined by the ratio of force to displacement velocity. Pollard[6] has obtained the input and transfer impedance equation and the reflection coefficient showing each has a structure identical to those of electrical theory. The reflection coefficient is given as

$$R = \frac{B}{A} = \frac{Z_O - Z_L}{Z_O + Z_L} \qquad (2.4)$$

Z_O is the characteristic impedance and equal to $\rho A_r C_O (1 + \frac{j\omega H}{C_O^2})^{\frac{1}{2}}$ which is in general taken as $\rho C_O A_r$.

Z_L is the load impedance at the end of the line and for a line resonator of finite length L, $Z_L = Z_O \tanh q_1 L$.

Using equations (2.3), (2.4) and the boundary condition, Sharp[3] has obtained the first reflection expression resulting from sinusoidal input in its Laplacian form as

$$R(O,S) = \frac{\omega_s}{s^2 + \omega_s^2} \frac{(s - \beta + n^2\alpha)^2 + \omega_n^2}{(s + \beta + n^2\alpha)^2 + \omega_n^2} \qquad (2.5)$$

where ω_s = angular transmitting frequency

ω_n = angular resonator fundamental frequency

n = mode order

α = $\dfrac{H^2\pi^2}{2L^2}$ = relaxation term which accounts for material loss

β = $\dfrac{C_2}{2L}\log_e(\frac{1}{R})$ = coupling term depends on the reflection R given in equation (2.4).

This is a lumped circuit model having a single resonance. A lumped circuit consisting of the mass spring and dashpot has a similar equivalence to the model developed by Sharp. Equation (2.5) is inverted by using a dominant pole approximation which is valid for the energy in a signal near the resonant frequency being considered and the theorem given in equation (2.6).

$$L^{-1}F(s) = \text{residues of } F(s)\exp(st) \qquad (2.6)$$

The solution to this problem is given in Ref.(3) and for lossless material.

$$R(0,t) = \text{Sin}(\omega_s t + \theta_1) + \frac{4\omega_s \beta S_1}{\omega_n S_2 S_3}\exp(-\beta t)\text{Sin}(\omega_n t + \theta_2)$$

$$(2.7)$$

where $S_1 = (\beta^2 + \omega_n^2)^{\frac{1}{2}}$

$S_2 = (\beta^2 + (\omega_n + \omega_s)^2)^{\frac{1}{2}}$

$S_3 = (\beta^2 + (\omega_n - \omega_s)^2)^{\frac{1}{2}}$

$\theta_1 = 2\tan^{-1}\dfrac{-2\omega_s\beta}{\beta^2 + (\omega_n^2 - \omega_s^2)}$

$\theta_2 = \tan^{-1}\dfrac{\beta\omega_n + \omega_n(\omega_n^2 - \omega_s^2)}{\beta^2 + \omega_n^2 + \omega_s^2}$

Various approximations and simplifications of the equation are dealt with in the next section.

2.4 The Characteristic of the Echo

This section describes the echo in terms of significant parameters and factors. The typical echo shown in Fig. 2.2 essentially consists of two components, the echo signal and echo decrement. The echo signal is the return of the wave incident on the resonator and it is at the transmitted frequency. The echo decrement which follows, is the exponential radiation of the stored energy and is always at the natural frequency of the resonator. Theoretical consideration shows that these two signals from the coupling mismatch and the re-radiation are in anti-phase and the echo return is the difference between the two signals.

The crossover is the most sensitive criterion of resonance, detuning even by 0.1% of the transmitted frequency causes a noticeable change in the crossover. From an experiment, a null crossover is obtained by adjusting the transmitted frequency and this value is equal to the natural resonant frequency.

The resonator is often described in terms of Q factor, frequency or its related parameter, number of oscillations to crossover. In practice, $\omega_n \gg \beta$ and at resonance $\omega_n = \omega_s$, therefore for lossless material $S_1 = \omega_n$, $S_2 = 2\omega_n$, $S_3 = \beta$, $\theta_1 \approx 180^\circ$ and $\theta_2 \approx 0^\circ$, equation (2.7) reduces to

$$R(0,t) = -\text{Sin}\,\omega_s t\,(1 - 2\exp(-\beta t)) \qquad (2.8)$$

The number of oscillations to crossover n_x is obtained by setting the right hand side of equation (2.8) to zero which

leads to equation (2.9).

$$n_x = n \, \frac{\log_e(2)}{\log_e(\frac{1}{R})} \qquad (2.9)$$

It will be seen that n_x is proportional to mode number n and R, being a constant for this particular resonator. This does not necessarily apply to other structures.

In general, the resonant parameters can be expressed with appropriate approximations in terms of acoustic parameters. Thus the term $\dfrac{\pi n}{\log_e(\frac{1}{R})}$ becomes the coupling Q of the system. It is related to the log decrement and can be expressed as

$$\frac{A_1}{A_N} = \exp\left(\frac{\pi N}{Q_c}\right) \qquad (2.10)$$

where A_1 and A_N are the amplitude of first and Nth pulses respectively in exponential decay. In the absence of material loss (H=O), and at crossover $A_1/A_N=2$ giving equation 2.11 which is frequently used in practice.

$$Q_c = \frac{\pi}{\log_e(2)} \, n_x = 4.53 \, n_x \qquad (2.11)$$

2.5 Two Close Modes With Different Coupling

In using the pulse-echo technique, a burst of oscillation at frequency f will contain significant power in band $f(1 \pm \frac{1}{P_n})$ where P_n is the number of oscillations in the burst which will excite any mode close to this frequency band. In general, resonators have very extensive spectra and modes can be sufficiently close to be excited by the same burst. These signals will interact and produce an elaborate echo pattern. In practice, a full analysis for the case of two closely associated modes require knowledge of the respective frequencies and line coupling.

The single mode echo pattern merely shows the transient response of the resonator which is highly dominated by a pair of complex poles and zeros close to the burst frequency. Therefore, the analysis of two interacting resonances can be considered by introducing another pair of complex poles and zeros which is close to it. An appropriate 's' plane diagram is shown in Fig. 2.4.

Using this approach, equation (2.12) gives Laplacian form the first reflection expression for a lossless resonator with two close modes resulting from a burst of sinusoidal input,

$$E_c(0,s) = R_c(0,s) \left[1 - \exp(-sT) \right] \qquad (2.12)$$

where
$$R_c(0,s) = \frac{\omega_s}{s^2 + \omega_s^2} \; \frac{\left[(s-\beta_1)^2 + \omega_1^2 \right] \left[(s-\beta_2)^2 + \omega_2^2 \right]}{\left[(s-\beta_2)^2 + \omega_1^2 \right] \left[(s+\beta_2)^2 + \omega_2^2 \right]}$$

T = burst duration

$R_c(0,s)$ is inverted by summing 6 residues from the poles using equation (2.6).

By means of suitable substitution and space - consuming manipulation, equation (2.13) gives the expression for $E_c(0,t)$.

$$E_c(0,t) = R_c(0,t) - H(t-T)R_c(0,t) \qquad (2.13)$$

where

$$R_c(0,t) = \text{Sin}(\omega_s t+\delta) + \frac{4\beta_1 \omega_s \exp(-\beta_1 t)}{\omega_1} \left(\frac{x_2^2+y_2^2}{u_2^2+v_2^2}\right)^{\frac{1}{2}} \sin(\omega_1 t+\delta_1)$$

$$+ \frac{4\beta_2 \omega_s \exp(-\beta_2 t)}{\omega_2} \left(\frac{x_3^2+y_3^2}{u_3^2+v_3^2}\right)^{\frac{1}{2}} \sin(\omega_2 t+\delta_2)$$

and

$$x_1 = (\beta_1^2+\omega_1^2-\omega_s^2)(\beta_2^2+\omega_2^2-\omega_s^2) - 4\beta_1\beta_2\omega_s^2$$

$$y_1 = 2\omega_s\left[\beta_2(\beta_1^2+\omega_1^2-\omega_s^2)+\beta_1(\beta_2^2+\omega_2^2-\omega_s^2)\right]$$

$$\delta = -2\tan^{-1}\left(\frac{y_1}{x_1}\right)$$

$$x_2 = \beta_1\left[(\beta_1+\beta_2)^2+\omega_2^2-\omega_1^2\right]-2\omega_1^2(\beta_1+\beta_2)$$

$$y_2 = \omega_1\left[(\beta_1+\beta_2)^2+\omega_2^2-\omega_1^2+2\beta_1(\beta_1+\beta_2)\right]$$

$$u_2 = 2\omega_1\left[\beta_1((\beta_2-\beta_1)^2+\omega_2^2-\omega_1^2)-(\beta_2-\beta_1)(\beta_1^2+\omega_s^2-\omega_1^2)\right]$$

$$v_2 = (\beta_1^2+\omega_s^2-\omega_1^2)\left[(\beta_2-\beta_1)^2+\omega_2^2-\omega_1^2\right]+4\omega_1^2\beta_1(\beta_2-\beta_1)$$

$$\delta_1 = \tan^{-1}\left(\frac{u_2}{v_2}\right) - \tan^{-1}\left(\frac{y_2}{x_2}\right)$$

$$x_3 = \beta_2\left[(\beta_1+\beta_2)^2-\omega_2^2+\omega_1^2\right]-2\omega_2^2(\beta_1+\beta_2)$$

$$y_3 = \omega_2\left[(\beta_1+\beta_2)^2-\omega_2^2+\omega_1^2+2\beta_2(\beta_1+\beta_2)\right]$$

$$u_3 = 2\omega_2\left[\beta_2\{(\beta_2-\beta_1)^2-\omega_2^2+\omega_1^2\}+(\beta_2-\beta_1)(\beta_2^2+\omega_s^2-\omega_2^2)\right]$$

$$v_3 = (\beta_2^2 + \omega_s^2 - \omega_2^2)\left[(\beta_2 - \beta_1)^2 - \omega_2^2 + \omega_1^2\right] - 4\omega_2^2\beta_2(\beta_2 - \beta_1)$$

$$\delta_2 = \tan^{-1}\left(\frac{u_3}{v_3}\right) - \tan^{-1}\left(\frac{y_3}{x_3}\right)$$

ω_s = transmitted angular frequency

ω_1, ω_2 = resonant angular frequency of first and second modes

$$\beta_1 = \frac{f_1 \log_e(2)}{n_{x_1}}$$

$$\beta_2 = \frac{f_2 \log_e(2)}{n_{x_2}}$$

f_1, f_2 = resonant frequencies of first and second modes

n_{x_1}, n_{x_2} = number of oscillations to crossover of first and second modes.

In using equation (2.13), Fig. 2.5 shows the echo pattern from an on-line mini-computer graphic unit in which the modal frequencies and the drive frequency are equal. The couplings are assumed to have a ratio of 3 to 1. Two crossovers are observed and each crossover corresponds to one of the modes. A tighter coupling is observed from the pattern and this would require another mathematical interpretation and would not obey the expression given in equation (2.9). The echo pattern has extensive modulations and the apparent steady state amplitude is not necessarily equal to the initial amplitude for a lossless material. Figs. 2.6 to 2.8 show the effect of detuning in the elaborate echo pattern. The two modal frequencies are equal and the drive frequency is 0.5%, 1% and 1.5% higher than the mode frequency. In these cases, no

crossover is observed and the echo pattern changes rapidly as the detuning increases. This illustrates that the crossover is still frequency sensitive.

To simulate the practical situation, the frequency separation of the modal frequencies are fixed at 1 to 5% in interval of 1%. The drive frequency is varied to search for the crossover and the ratio of the coupling is chosen to be 3 to 1. Figs.(2.9) to (2.13) show the echo patterns obtained from the graphic unit. The result shows that a crossover can be obtained at two different drive frequencies neither of which is equal to the mode frequencies. The deviation of the drive frequency to obtain the crossover is sensitive to the percentage separation of the two modal frequencies and the coupling terms have only a small effect on this drive frequency.

When the value of the coupling term is available, a direct comparison between the computer plot and the experimental display allows the values of two close resonant frequencies to be determined.

2.6 The High Order Mode Echo - "Stepped Decrement"

A line resonator has a harmonic spectrum of resonances, so that $\omega_n = n\omega_1$. The computer plot for modes above the fundamental using equation (2.7) gives a pure exponential echo pattern and gives the correct null position but the stepping effect observed experimentally does not appear.

This stepping effect is observed for modes above the fundamental. The step interval is equal to the resonator transit time and hence the number of oscillations per step is approximately equal to the mode number. Strictly speaking, the fundamental is also stepped, having one oscillation per step. The effect is seen to be dominated by the fundamental mode.

Using this ideas, the poles considered in the 's' plane diagram for high order mode is not only the pole adjacent to the transmitted frequency but also all the harmonically related poles below the transmitted frequency. Equation (2.14) gives the general first reflection expression for a 'n' stepped mode resulting from a sinusoidal input in its Laplacian form.

$$R_n(0,s) = \frac{\omega_s}{s^2 + \omega_s^2} \prod_{k=1}^{k=n} \frac{(s-\beta_k)^2 + \omega_k^2}{(s+\beta_k)^2 + \omega_k^2} \qquad (2.14)$$

where $\omega_k' = k\omega_1$ and $n = 1,2,3,\ldots$

The inversion of equation (2.14) is obtained by summing $2(n+1)$ residues from the poles. For mode n=3, the

numbers of summing residues is 8. Fig. 2.14 shows an appropriate 's' plane diagram for mode n=3. The mathematical expression for n⩾3 would be considerably more elaborate than that already obtained and would demand excessive effort to perform if a full solution were attempted. However, the poles and zeros are well separated in frequency and in practice as $\omega_s \gg \beta$; the mathematical term contributed by the lower half plane can be neglected without loss of the essence of the model. With this simplification, the inversion assuming three arbitrary modes, have the form shown in equation (2.15).

$$R_3(0,t) = \sin\left[\omega_s t - 2(a_1 + a_2 + a_3)\right] - \frac{2\ell_6 \ell_7 \ell_8}{\ell_1 \ell_4 \ell_5} \frac{\omega_s}{(\omega_s + \omega_1)}$$

$$\exp(-\beta_1 t) \sin(\omega_1 t + a_7 + a_8 - a_1 - a_4 - a_5)$$

$$+ \frac{2\ell_7 \ell_9 \ell_{10}}{\ell_2 \ell_5 \ell_{11}} \frac{\omega_s}{\omega_s + \omega_2} \exp(-\beta_2 t) \sin(\omega_2 t + a_{10} - a_7 - a_5 - a_2 - a_{11})$$

$$- \frac{2\ell_8 \ell_{10} \ell_{12}}{\ell_3 \ell_4 \ell_{11}} \frac{\omega_s}{\omega_s + \omega_3} \exp(-\beta_3 t) \sin(\omega_s t - a_3 - a_4 - a_8 - a_{11} - a_{10})$$

$$(2.15)$$

where $\ell_1 = \left[\beta_1^2 + (\omega_s - \omega_1)^2\right]^{\frac{1}{2}}$ $\qquad a_1 = \tan^{-1}\dfrac{\omega_s - \omega_1}{\beta_1}$

$\ell_2 = \left[\beta_2^2 + (\omega_s - \omega_2)^2\right]^{\frac{1}{2}}$ $\qquad a_2 = \tan^{-1}\dfrac{\omega_s - \omega_2}{\beta_2}$

$\ell_3 = \left[\beta_3^2 + (\omega_s - \omega_3)^2\right]^{\frac{1}{2}}$ $\qquad a_3 = \tan^{-1}\dfrac{\omega_s - \omega_3}{\beta_3}$

$\ell_4 = \left[(\beta_1 - \beta_3)^2 + (\omega_s - \omega_1)^2\right]^{\frac{1}{2}}$ $\qquad a_4 = \tan^{-1}\dfrac{\omega_3 - \omega_1}{\beta_1 - \beta_3}$

$\ell_5 = \left[(\beta_1 - \beta_2)^2 + (\omega_2 - \omega_1)^2\right]^{\frac{1}{2}}$ $\qquad a_5 = \tan^{-1}\dfrac{\omega_2 - \omega_1}{\beta_1 - \beta_2}$

$\ell_6 = 2\beta_1$

$$\ell_7 = \left[(\beta_1^2 + \beta_2^2) + (\omega_2 - \omega_1)^2 \right]^{\frac{1}{2}} \qquad a_7 = \tan^{-1}\frac{\omega_2 - \omega_1}{\beta_1 + \beta_2}$$

$$\ell_8 = \left[(\beta_1 + \beta_3)^2 + (\omega_s - \omega_1)^2 \right]^{\frac{1}{2}} \qquad a_8 = \tan^{-1}\frac{\omega_3 - \omega_1}{\beta_1 + \beta_3}$$

$$\ell_9 = 2\beta_2$$

$$\ell_{10} = \left[(\beta_2 + \beta_3)^2 + (\omega_3 - \omega_2)^2 \right]^{\frac{1}{2}} \qquad a_{10} = \tan^{-1}\frac{\omega_3 - \omega_2}{\beta_2 - \beta_3}$$

$$\ell_{11} = \left[(\beta_2 - \beta_3)^2 + (\omega_3 - \omega_2)^2 \right]^{\frac{1}{2}} \qquad a_{11} = \tan^{-1}\frac{\omega_3 - \omega_2}{\beta_2 - \beta_3}$$

$$\ell_{12} = 2\beta_3$$

$$\beta_1 = \frac{f_1}{n_{x_1}} \log_e(2)$$

$$\beta_2 = \frac{f_2}{n_{x_2}} \log_2(2)$$

$$\beta_3 = \frac{f_3}{n_{x_3}} \log_e(2)$$

f_1, f_2, f_3 = resonant frequencies of first, second and third modes.

n_{x_1}, n_{x_2}, n_{x_3} = number of oscillations to crossover of first, second and third modes.

For a line resonator has the properties that the overtones are harmonic ($\omega_n = n\omega_1$) and the coupling is such that n_x/n is constant. Equation (2.15) simplifies to equation (2.16).

$$R_3(0,t) = 2r_o \sin(\omega_s t + \theta_o) + 2r_1 \exp(-\beta_1 t) \sin(\omega_1 t + \theta_1)$$

$$+ 2r_2 \exp(-\beta_1 t) \sin(\omega_2 t + \theta_2)$$

$$+ 2r_3 \exp(-\beta_1 t) \sin(\omega_3 t + \theta_3)$$

$$(2.16)$$

where

$$r_o = \tfrac{1}{2}$$

$$\theta_o = \pi - 2(\alpha_1 + \alpha_2 + \alpha_3)$$

$$r_1 = \frac{\omega_s}{(\omega_1 + \omega_s)^2} \frac{L_4 L_5 L_7}{2L_1 L_6^2}$$

$$\theta_1 = \pi - (\alpha_1 - \alpha_4 - \alpha_5)$$

$$r_2 = \frac{\omega_s}{(2\omega_1 + \omega_s)} \frac{L_4^2 L_7}{L_6^2 L_2}$$

$$\theta_2 = -\alpha_2$$

$$r_3 = \frac{\omega_s}{(3\omega_1 + \omega_s)} \frac{L_4 L_5 L_7}{2L_3 L_6^2}$$

$$\theta_3 = \pi - (\alpha_3 + \alpha_4 + \alpha_5)$$

and

$$L_1 = \left[(\omega_s - \omega_1)^2 + \beta_1^2\right]^{\tfrac{1}{2}}$$

$$\alpha_1 = \tan^{-1} \frac{\omega_s - \omega_1}{\beta_1}$$

$$L_2 = \left[(\omega_s - 2\omega_1)^2 + \beta_1^2\right]^{\tfrac{1}{2}}$$

$$\alpha_2 = \tan^{-1} \frac{\omega_s - 2\omega_1}{\beta_1}$$

$$L_3 = \left[(\omega_s - 3\omega_1)^2 + \beta_1^2\right]^{\tfrac{1}{2}}$$

$$\alpha_3 = \tan^{-1} \frac{\omega_s - 3\omega_1}{\beta_1}$$

$$L_4 = \left[\omega_1^2 + (2\beta_1)^2\right]^{\tfrac{1}{2}}$$

$$\alpha_4 = \tan^{-1} \frac{\omega_1}{2\beta_1}$$

$$L_5 = \left[(2\omega_1)^2 + (2\beta_1)^2\right]^{\tfrac{1}{2}}$$

$$\alpha_5 = \tan^{-1} \frac{\omega_1}{\beta_1}$$

$$L_6 = \omega_1$$

$$\beta_1 = \frac{f_1}{n_{x_1}} \log_e(2)$$

$$L_7 = 2\beta_1$$

Numerical solutions of equation (2.15) are shown graphically in Figs. 2.15 and 2.17 where n=2 and 3 respectively. Here the drive and resonant frequencies are equal and the characteristic stepped pattern occurs with the crossover at the calculated values. Figs. 2.16 and 2.18 show corresponding experimental results for n=2 and 3. The agreement between experimental and theoretical patterns are excellent and all

the main features correspond. There is some deviation in
the experimental display due to the inherently finite
bandwidth of the transducer.

2.7   's' Plane Model for the Contour Vibration of Isotropic Disks

2.7.1   Mathematical Analysis

The one dimensional plane wave resonator was analysed by Sharp. The mechanical impedance is obtained from the ratio of force to velocity in Laplacian form and expressed in terms of β value and frictional losses (α). If the echo pattern of any body is konwn, this 's' plane model can be used with the appropriate β value to obtain the response to a known excitation.

The two dimensional resonator represented by a thin disk has been widely used for the precise determination of elastic constant and ultrasonic characterisation of material[7]. The displacement involved in this case are radial (u_r) and tangential (u_θ). The analysis giving the coupling of a thin disk is derived here.

To obtain the model using the previous method would become very complicated and difficult to solve. In this case, the Rayleigh Energy method[4] is employed to express the β value in terms of the equivalent mass at resonance. The equivalent mass (M_{eq}) of a resonant system can be evaluated through equation (2.17).

$$(M_{eq})_x = \frac{\frac{\rho}{2} \iiint \dot{u}^2 \, d_x \, d_y \, d_z}{\frac{1}{2} (\dot{u})_x^2} \qquad (2.17)$$

For a contour extensional vibration of a thin disk which involves no transverse displacement. The radial and tangential displacements are given as[8],[9]

$$u_r = \left[A_1 \frac{dJ_n(Kr/a)}{dr} + \frac{nB_1}{r} J_n(K\theta r/a) \right] \cos n\theta \cos \omega t \quad (2.18)$$

$$u_\theta = \left[\frac{nA_1}{r} J_n(Kr/a) + B_1 \frac{dJ_n(K\theta r/a)}{dr} \right] \sin n\theta \cos \omega t \quad (2.19)$$

where

$$\frac{B_1}{A_1} = \frac{J_n(K)}{J_n(K\theta)} \frac{\frac{1}{2}(K\theta)^2 - n(n+1) + M_n(K)}{n[M_n(K\theta) - (n+1)]}$$

$$K = \frac{\omega a}{C_p} \qquad\qquad \theta^2 = \frac{2}{1-\sigma}$$

r : radial distance

a : radius of the disk

$$M_n(X) = X \frac{J_{n-1}(X)}{J_n(X)}$$

Using equation (2.17), the equivalent mass as seen at the driving point ($\theta = 0^\circ$) on the edge of the disk is given in equation (2.20).

$$M_{eq} = \frac{\rho h \int_o^a \int_o^{2\pi} \left[\left(\frac{\partial u_r}{\partial t}\right)^2 + \left(\frac{\partial u_\theta}{\partial t}\right)^2 \right] r \, dr \, d\theta}{\left(\frac{\partial u_r}{\partial t}\right)^2 + \left(\frac{\partial u_\theta}{\partial t}\right)^2} \quad (2.20)$$

h : thickness of the disk

Equation (2.21) is obtained by inserting equations (2.18) and (2.19) into equation (2.20).

$$M_{eq} = \frac{M\left[I_1(K)+I_2(K)+T_4^2(I_1(K\Theta)+I_2(K\Theta))+2nT_4(I_3+I_4)\right]}{T_1+T_2+T_3}$$

(2.21)

where

$$I_1(K) = \int_0^a \left(\frac{\partial J_n(Kr/a)}{\partial r}\right) \dot{r} \, d_r$$

$$I_2(K) = \int_0^a \frac{n^2 J_n^2(Kr/a)}{r} \, d_r$$

$$I_1(K)+I_2(K) = \frac{1}{8}K^2\{J_{n+1}^2(K)+3J_{n-1}^2(K)-J_n(K)\left[J_{n+2}(K)+3J_{n-2}(K)\right]\}$$

$$I_3(K) = \int_0^a J_n(K\Theta r/a) \frac{\partial J_n(Kr/a)}{\partial r} \, d_r$$

$$I_4(K) = \int_0^a J_n(Kr/a) \frac{\partial J_n(k\Theta r/a)}{\partial r} \, d_r$$

$$I_3(K) + I_4(K) = J_n(K) \, J_n(K\Theta)$$

$$T_1 = \left[a\frac{\partial}{\partial r} J_n(K\frac{r}{a})\right]^2 = \frac{K^2}{4}\left[J_{n-1}(K) - J_{n+1}(K)\right]^2$$

$$T_2 = \left[nT_4 J_n(K\Theta)\right]^2$$

$$T_3 = 2nT_4 a J_n(K\Theta)\frac{\partial}{\partial r} J_n(Kr/a)$$

$$= nKT_4 \, J_n(K\Theta)\left[J_{n-1}(K)-J_{n+1}(K)\right]$$

$$T_4 = \frac{B_1}{A_1} \text{ (as in equation (2.18))}$$

M = static mass of the disk.

A good reference on integrals of Bessel functions could be found in Luke[10].

In addition to the asymmetric modes, the expression of M_{eq} for the pure radial mode at the driving point and on the edge of the disk is reduced to

$$M_{eq} = \frac{2\int_0^a [\frac{\partial J_o(K_{1,R}\frac{r}{a})}{\partial r}]^2 rd_r}{K_{1,R}^2 J_1^2(K_{1,R})} \tag{2.22}$$

Equation (2.18) can be simplified to give

$$\frac{M_{eq}}{M} = 1 - \frac{J_o(K_{1,R})J_2(K_{1,R})}{J_1^2(K_{1,R})} \tag{2.23}$$

and $K_{1,R}$ is determined from the characteristic equation

$$M_1(K_{1,R}) = 1-\sigma \tag{2.23a}$$

Using the same procedure, equation (2.24) gives the ratio of M_{eq}/M for the pure tangential mode.

$$\frac{M_{eq}}{M} = 1 - \frac{J_o(K_{1,T}\theta)J_2(K_{1,T}\theta)}{J_1^2(K_{1,T}\theta)} \simeq 1 \tag{2.24}$$

and $K_{1,T}$ is determined from the characteristic equation

$$M_1(K_{1,T}) = 2 \tag{2.24a}$$

From equation (2.23) the values of M_{eq}/M for the pure radial mode was evaluated and also included in Table 2.1.

In echo systems, the resonator is often described in terms of its coupling Q_c and the number of oscillations

to crossover n_x. Q_c is related to the log decrement by $Q_c = \pi/D_c$ where D_c is log decrement and from equation (2.7), can be shown to be

$$D_c = \frac{\beta}{I} \qquad (2.25)$$

Using equation (2.11), and (2.25), the coupling value of a contour extensional vibration of a thin disk β_d is thus obtained once M_{eq} is known and shown in equation (2.26).

$$\beta_{d,n} = \frac{1}{2} \frac{Z_L}{(M_{eq})_n} \qquad (2.26)$$

$\beta_{d,n}$: coupling value of a thin disk of mode order n

$(M_{eq})_n$: equivalent mass of mode order n on the edge of the disk, radius a

Using equation (2.21), Table 2.1 represents the ratio of $(M_{eq})_n/M$ against mode order n for a useful range of Poisson's ratio in interval of 0.1. Once the choice of dimensions and mode of vibrations corresponding to any frequency have been made, the M_{eq} at the driving point can be evaluated.

An inspection of Table 2.1 reveals some interesting facts. First, the equivalent mass of the lowest order mode (n=2) will have a higher value than half the static mass. The result arises from the fact that the amplitude component reaches a maximum near the periphery and at the drive point,

it has fallen significantly[11]. The value of M_{eq} does

drop as n increases. Second, from the tabulated value of

eigenvalues $K_{1,n}$ for the lowest five modes, the $K_{1,n}(M_{eq})_n$

is approximately constant. This is consistent to the

experience of the author that the coupling of the lowest

five asymmetric - disk eigenmodes are approximately constant.

Fig. 2.19 shows the coupling Q value of a thin disk and

compares to the thin rod. The coupling Q_c is normalised

to Q_c of mode order 2 and the Poisson's ratio is assumed to

be 0.3 (typically of most metal). It can be seen that the

effective change in coupling of a thin disk is small as

compared with the rod resonator and not easily observed if the

n_x value is small.

With the use of derived M_{eq} values, the 's' plane model

for a thin disk is obtained. Equation (2.27) gives the

expression of low order mode for a thin disk in Laplacian form

resulting from a sinusoidal input is

$$R_{(0,s)} = \frac{\omega_s}{s^2 + \omega_s^2} \prod_{k=2}^{n} \frac{(s-\beta_{d,k})^2 + \omega_{1,k}^2}{(s+\beta_{d,k})^2 + \omega_{1,k}^2} \tag{2.27}$$

where $\beta_{d,k}$ = β value of a disk of mode n and derived from

equation (2.26)

The separation of $\omega_{1,k}$ is obtained from the equation

drived by Love[12]. The computer plot can be easily adapted

for this case. Fig. 2.20 shows an 's' plane diagram for

the case of a disk for the asymmetric mode up to four and the

pure radial mode (1,R) is included. As the radial drive to the disk, the asymmetric and the 1,R modes are excited but not to the tangential mode.

2.7.2 Comparison with Experiments

To test the values of equivalent mass derived above, measurements were carried on a series of thin disks. The M_{eq} values can be evaluated by equation (2.26) once the line impedance is known. To determine the accurate line impedance without any known acoustic data, a brass specimen 6.5 mm diameter, 100 mm long had a weight of 25.047 gm was used. A 0.7 mm diameter nickel wire excited the rod longitudinally, the resonant frequencies and the number of oscillations to crossover were measured. For a thin rod resonator, Q_c is proportional to mode number so long as the waves are plane and from equation (2.9), it deduces $n_{xn}=n_{x1}/n$ where n_{xn} is the number of oscillations to crossover of nth mode. It can be shown that the driving line impedance Z_ℓ can be expressed as

$$Z_\ell = \frac{f_n M_1}{n_{xn}} \log_e(2) \qquad\qquad (2.28)$$

where M_1 is the static mass of the rod resonator.

Therefore the acoustic impedance of the line could be found experimentally. The experiment was repeated with a 1 mm diameter nickel wire. Table 2.2 shows these values.

The 0.7 mm line was then fitted radially to the edge of an aluminium thin disk of 35.5 mm diameter and 1.56 mm thick. The disk weighed 3.880 gm. The Poisson's ratio of this specimen was found to be 0.340 using the technique described in a later chapter. The in-plane frequency spectrum and corresponding n_x values for all the low order modes were measured. By substituting the measured values of frequencies and number of oscillations to crossover for each mode into equation (2.11) and (2.28), the value of M_{eq} were found. A comparison was then made with calculated values from equation (2.21). Table 2.3 shows the results. The experiments were repeated for thin brass and steel disks with the 1 mm and 0.7 mm diameter line drive respectively. Table 2.4 and 2.5 show the results.

With the exception of only one mode (for aluminium disk), all the experimental values are considered as satisfactory results. This effect when n=3, is due to the interaction of two modal frequencies. It has been shown earlier that when two modes of equal frequency interacts each other, the resulting value in n_x will be significantly altered depending on their β values. A satisfactory agreement on the ratio of $(M_{eq})_n/M$ between the theory and experiments was obtained. The accuracy is, of course, limited by the uncertainty of $\pm\frac{1}{2}$ on the value of n_x. A large reduction in the acoustic line diameter would minimise the uncertainty of n_x but would require a much longer line which may create inconvenience and problems in measurement. Nevertheless, the deviation in this case is small and good enough to justify the 's' plane model

for a thin disk shown in fig. 2.20.

This model is particularly useful in the analysis of the
signal from two adjacent frequency modes and in giving
details of the stepped signal and decrement which is a
feature of all high order modes. Adjacent frequencies such
as the distortion mode with 3 nodal diameters (1,3) and the
pure radial mode (1,R) for aluminium described above and
possibly of greater importance the two resonances which occurs
when a mode is split due to elastic anisotropy dealt with in
Chapter 6. The Poisson's ratio measurement depends on
obtaining the frequencies of distortion mode 1,3 and the pure
radial mode 1,R. In an experimental test, a 50.8 mm
diameter steel disk was excited by a 1 mm nickel wire, the
modes 1,3 and 1,R were found to interact and have frequencies
of 73.682 kHz and 69.991 kHz respectively. The coupling Q_c
of modes 1,3 and 1,R were found to be 113.25 and 262.74.
The successive computer plots of this particular case show that
the exact values of modes 1,3 and 1,R should be 73.650 kHz
and 70.000 kHz. The actual frequency separation is 4.96%. The
correction obtained from these two modal frequencies enables
an imporved value of Poisson's ratio to be obtained. Figs.
2.21 - 2.24 show the echo patterns of modes 1,3 and 1,R
obtained from the mini-computer graphic unit and the
oscilloscope display.

The experiment was repeated on a 99.99% pure tantalum
disk and the separation of frequencies and couplings were
much closer than the steel disk.   Figs. 2.25 - 2.28 show

the calculated and experimental echo apttern in this case.
The computer plots using the 's' plane model of a disk
produce exactly the same patterns as in the experiments.

2.8 Resonators With Losses

The echo analysis described so far is lossless. Including losses inside the resonator results dramatic changes occur in the shape of the echo. Therefore, a brief analysis is given in terms of the discussion above.

For the material with loss and within the condition $\beta > n^2 \alpha$, the echo expression at resonance from equation (2.5) becomes

$$R(0,t) = - \frac{\beta - n^2 \alpha}{\beta + n^2 \alpha} (1 - \frac{2\beta}{\beta - n^2 \alpha} \exp(-\beta - n^2 \alpha) t) \sin \omega t$$

$$(2.28)$$

Using equations (2.10), (2.15) and (2.18), three Q values are related to the resonator.

$$Q_c = \pi f / \beta = \text{coupling } Q \qquad (2.29a)$$

$$Q_m = \pi f / n^2 \alpha = \text{material } Q \qquad (2.29b)$$

and

$$Q_T = (Q_c^{-1} + Q_m^{-1}) = \text{Total } Q \qquad (2.30)$$

From equation (2.28), the number of oscillations to crossover for the material with losses (n_{xm}) is given in equation (2.31).

$$n_{xm} = \frac{f}{\beta + n^2 \alpha} \left[\log_e (\frac{2\beta}{\beta - n^2 \alpha}) \right] \qquad (2.31)$$

Using the Q relationships, the relative steady state amplitude A_∞ / A_0 can be expressed in terms of Q_c and Q_m as

$$\frac{A_\infty}{A_O} = - \frac{(1 - Q_C/Q_m)}{1 + Q_C/Q_m} \qquad (2.32)$$

Equation (2.32) can be transposed to express Q_C/Q_m in terms of directly observed A_O and A_∞ values.

$$\frac{Q_C}{Q_m} = \frac{1 + A_O/A_\infty}{1 - A_O/A_\infty} \qquad (2.33)$$

Equation (2.31) then becomes [13]

$$n_{xm} = \frac{Q_C}{\pi(1+Q_C/Q_m)} \log_e \left[2/(1-Q_C/Q_m) \right] \qquad (2.34)$$

In the absence of material losses, $A_O = A_\infty$, $Q_m^{-1} = 0$ and $n_{xm} = n_x$. From which it follows that the steady state echo amplitude will decrease and the number of oscillations to crossover will increase because of the lower value of Q_T.

Fig. 2.29 shows the resulting 's' plane diagram with material losses and figs. 2.30-2.32, how the shape of the echo varies with increased losses. Fig. 2.31 shows that if $Q_C = Q_m$, the steady state echo amplitude is zero because the reflected echo amplitude is equal to the steady state echo amplitude inside the resonator. Fig. 2.32 shows that crossover is lost when the large proportions of power is dissipated inside the lossy material and for this case, the zeros in the 's' plane diagram will shift to the left of the frequency axis.

From the echo observations, A_O, A_∞, n_{xm}, Q_T can be obtained directly so the values of material loss Q_m can be measured provided the line is long enough to obtain the steady state amplitude of the echo.

Using this approach, fig. 2.33 shows the variation of Q_m of an aluminium disk against temperature. A locus plot of a single zero corresponding to this case is also given in fig. 2.34.

2.9 Conclusion

This chapter presents a generalised 's' plane model of a resonator. It has been used to analyse the interaction of two modal frequencies and the stepped echo pattern which are frequently encountered in practical case. The coupling values of contour vibrations of isotropic disks which involves two dimensional displacements has been derived. This was necessary for the full 's' plane model of a thin disk to be developed.

The characteristic of the stepped echo pattern plays an important role in studying high order mode vibration which is the limit when n is large results in an explanation of the dispersion of one dimensional edge surface wave which travels round the periphery of various geometrical structures. This will be discussed in the next chapters.
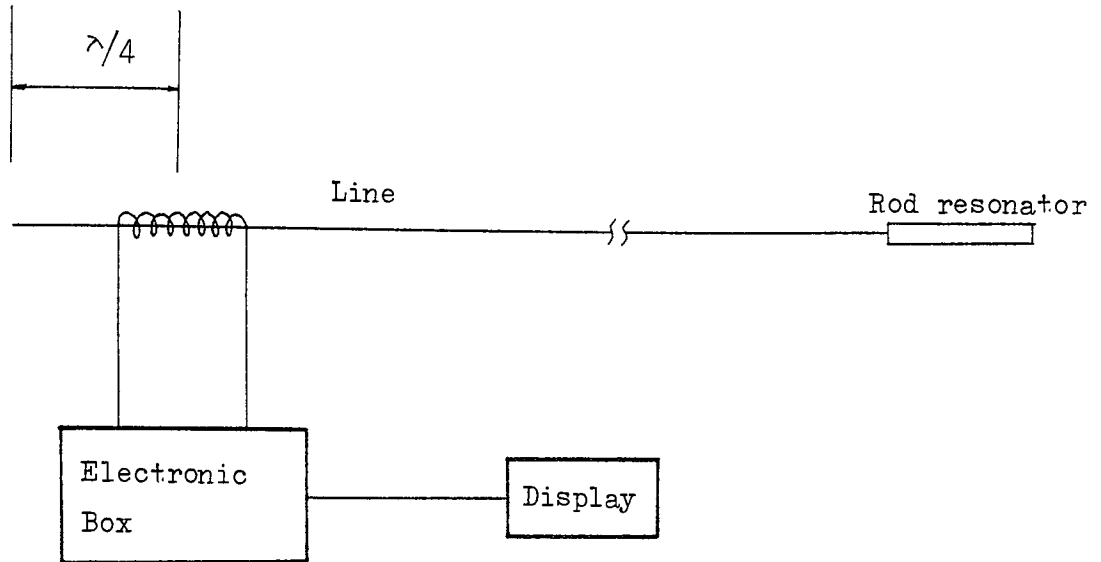
Figure 2.1 Schematic diagram of pulse-echo system.
The magnetostrictive transducer coil allows the generation
and reception of a burst of longitudinal waves in the
acoustic line. The line must be sufficiently long to
separate the transmission from the return echo. The thin
rod resonator shown can be considered as the termination of
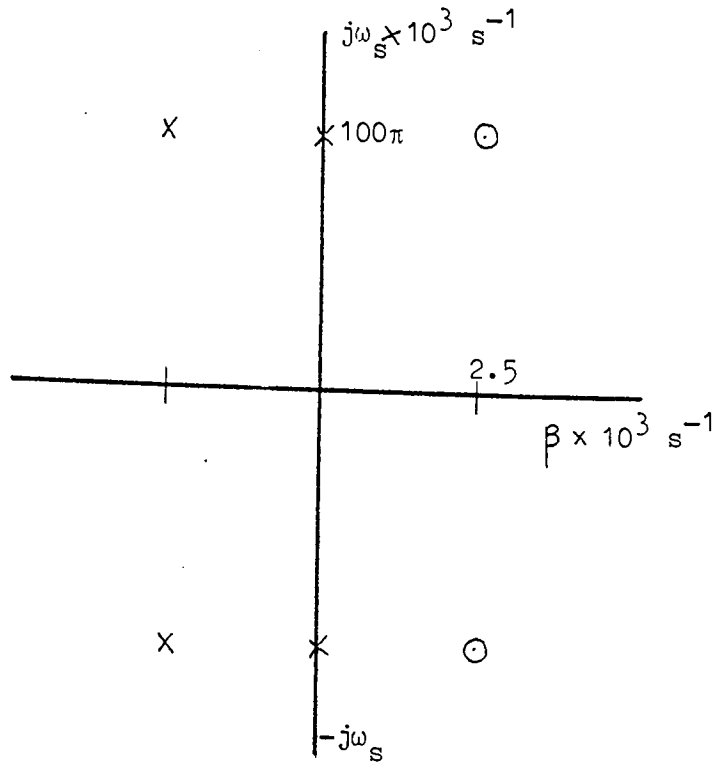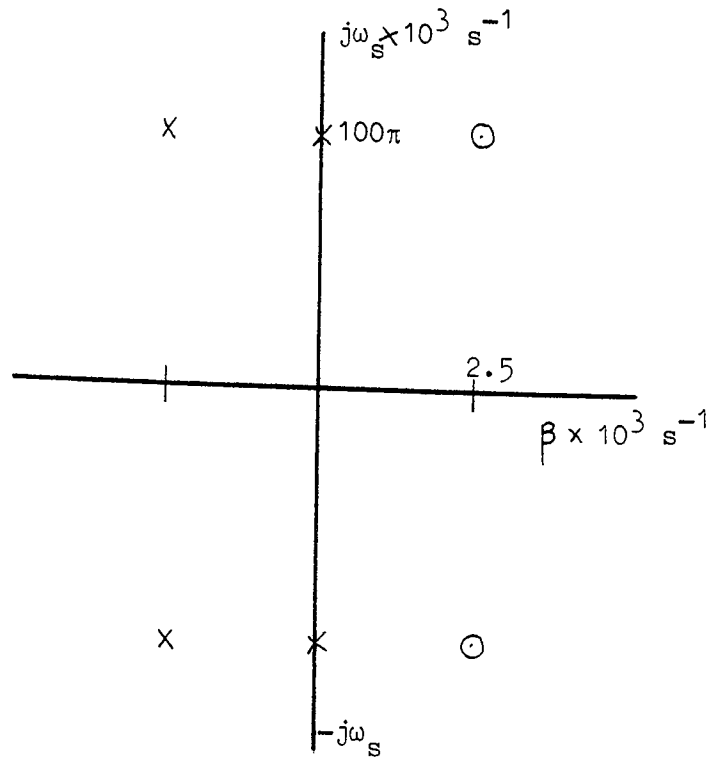this line and analysis of the echo is carried out in these
terms.

Figure 2.2 s-plane diagram of a simple lossless resonance.
As sharp resonances are required, the line coupling is made small
representing a low coupling loss (high Q_c). The data shown in the
diagram were evaluated by assuming fundamental frequency = 50 kHz
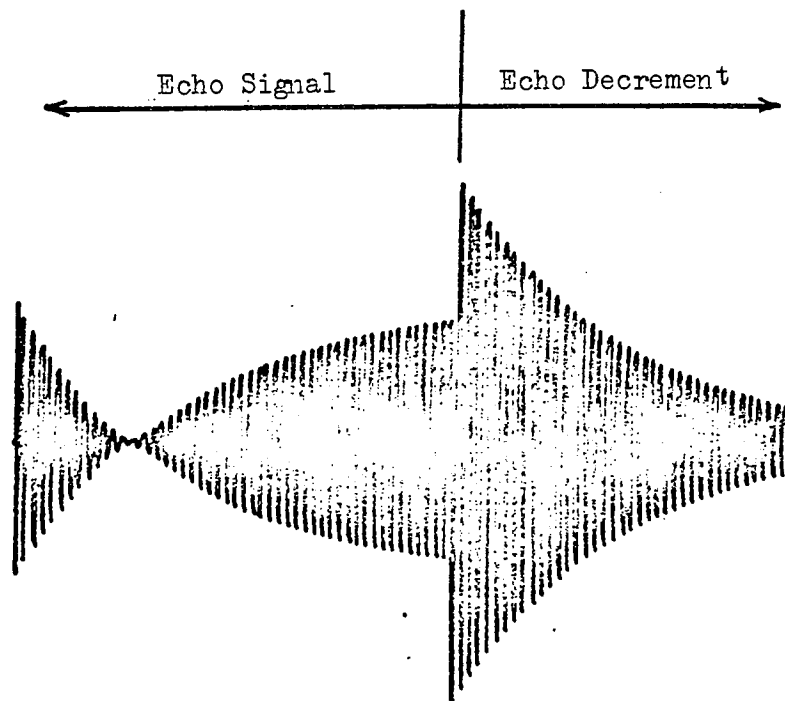and the reflection coefficient = 0.95. This gives Q_c = 60.
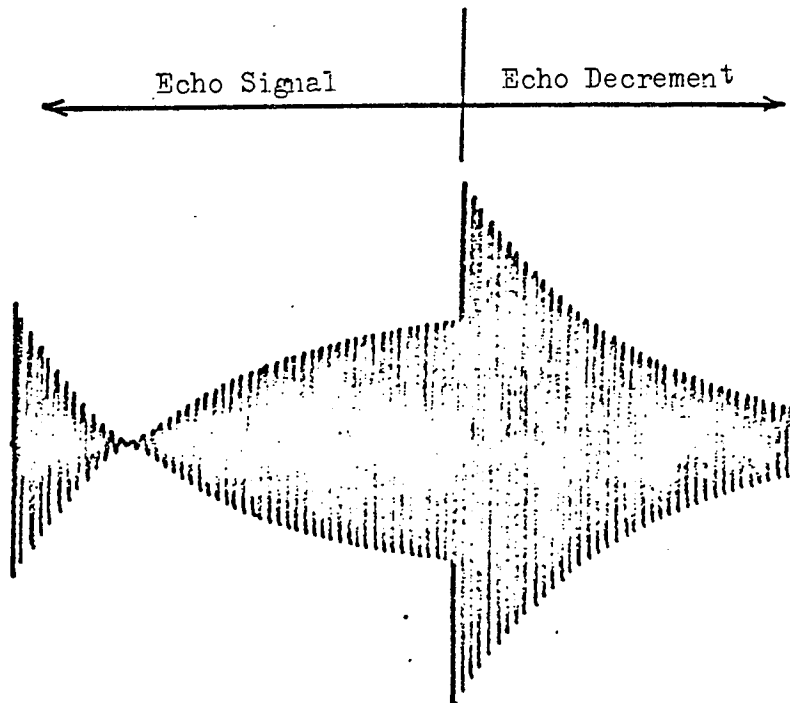
Figure 2.3 The resultant computer plot for the rod resonator using
the s-plane diagram of fig.2.2. The burst number is 50. A lossless
material gives the steady state echo signal equal to the initial signal.

Figure 2.2   s-plane diagram of a simple lossless resonance.
As sharp resonances are required, the line coupling is made small
representing a low coupling loss (high Q_c). The data shown in the
diagram were evaluated by assuming fundamental frequency = 50 kHz
and the reflection coefficient = 0.95. This gives Q_c = 60.

Figure 2.3   The resultant computer plot for the rod resonator using
the s-plane diagram of fig.2.2. The burst number is 50. A lossless
material gives the steady state echo signal equal to the initial signal.
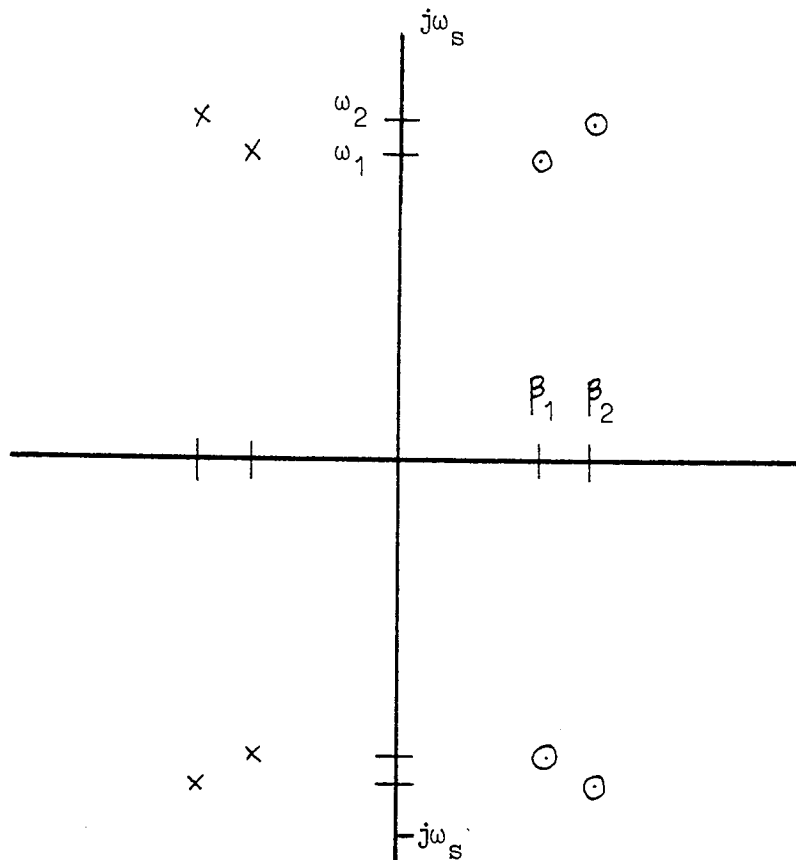
Figure 2.4 s-plane diagram for two adjacent modes.

As in fig. 2.2, the real axis is greatly expanded. In the

case shown, the second resonance has a slightly higher frequency

and a lower Q_c. The drive frequency will contribute a pair of
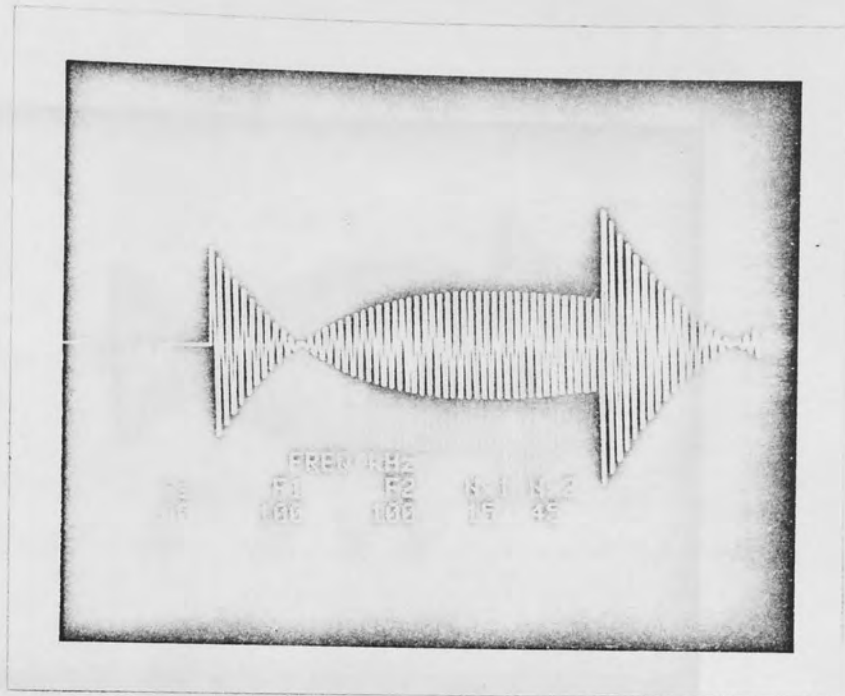
conjugate poles along the imaginary axis.

Figure 2.5 The echo pattern resulting from the interaction of two equal resonant modes. The signal pattern is no longer a simple exponential.
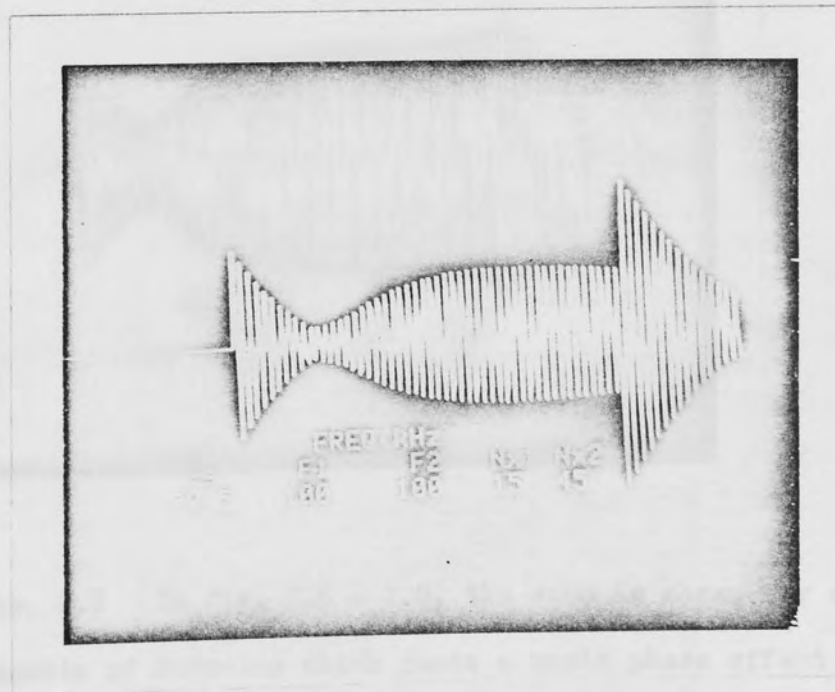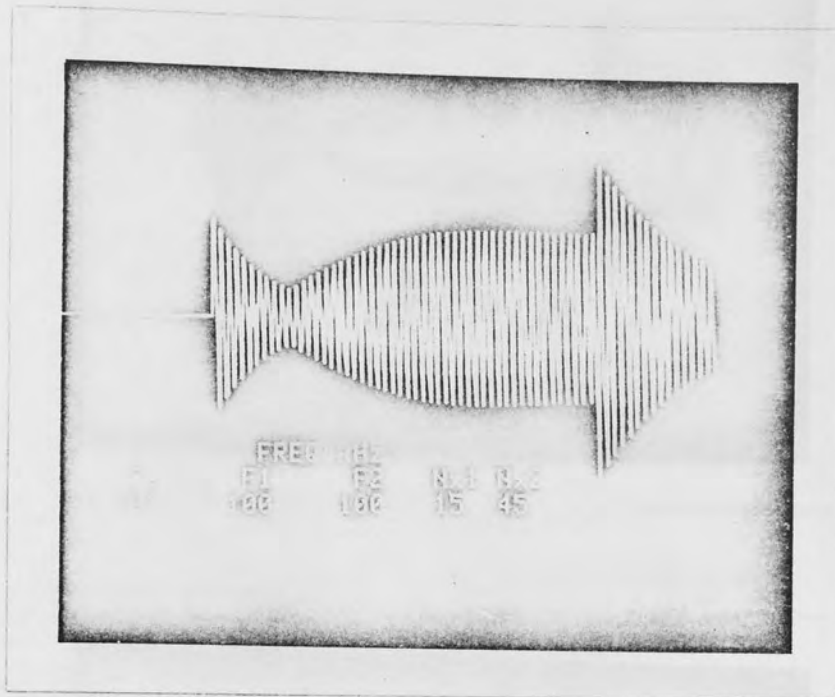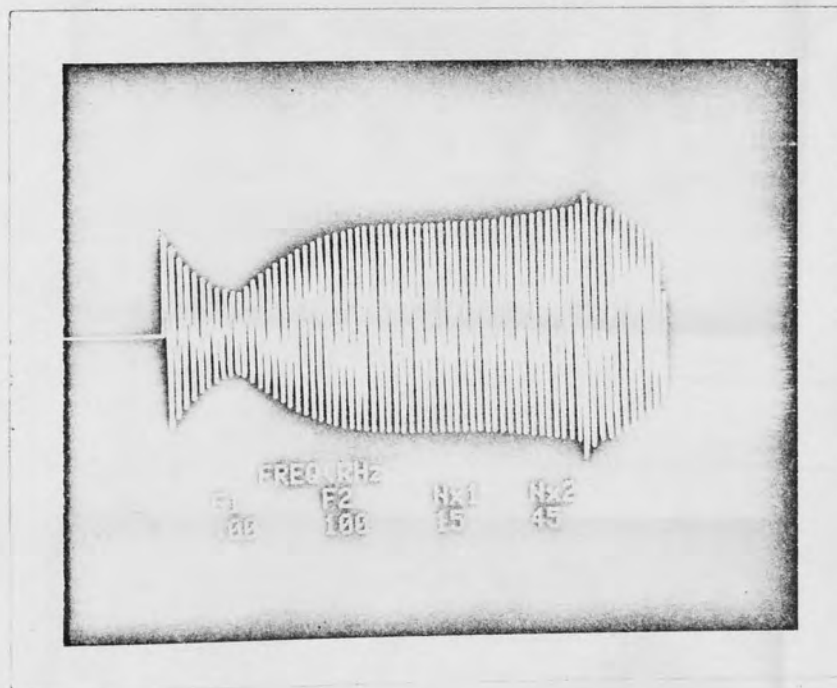

Figure 2.6

Fig. 2.7

Fig. 2.8   In fig. 2.6 – 2.8, the echo is shown for small
amounts of detuning which cause a rapid phase effect on the
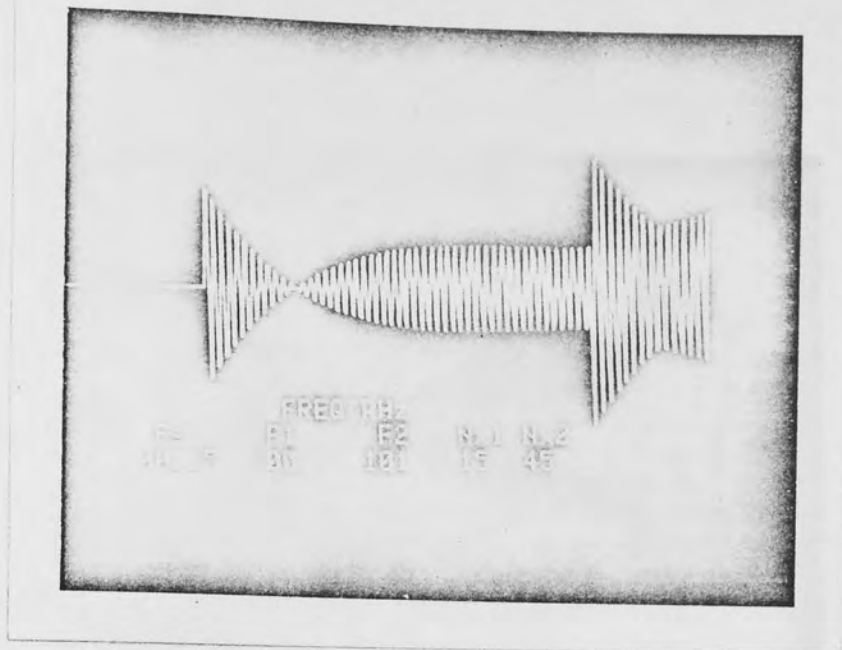signal. This shows the pattern is very sensitive to the
drive frequency.

Fig. 2.9
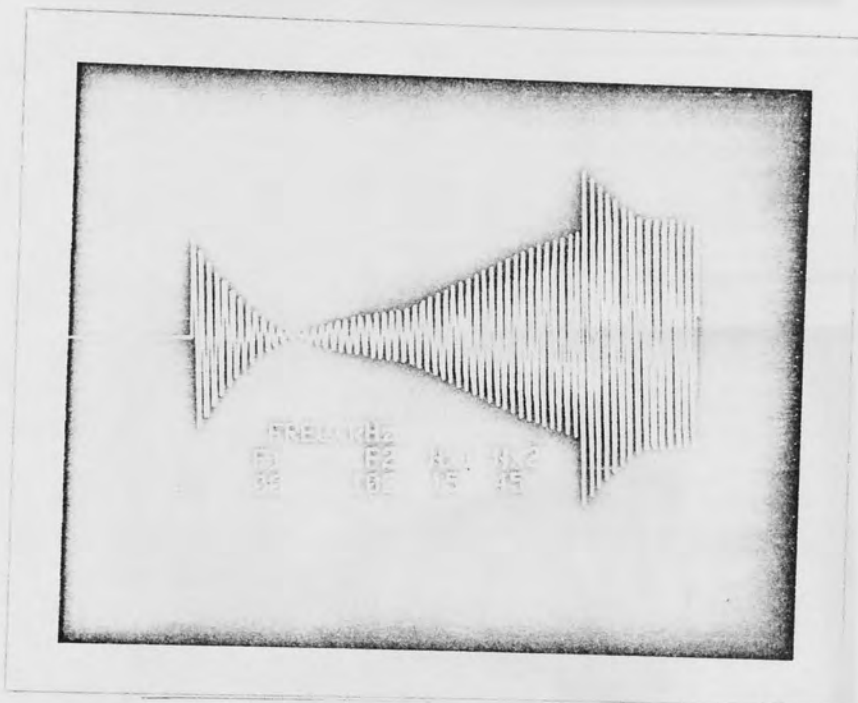
Fig. 2.10

Fig. 2.11
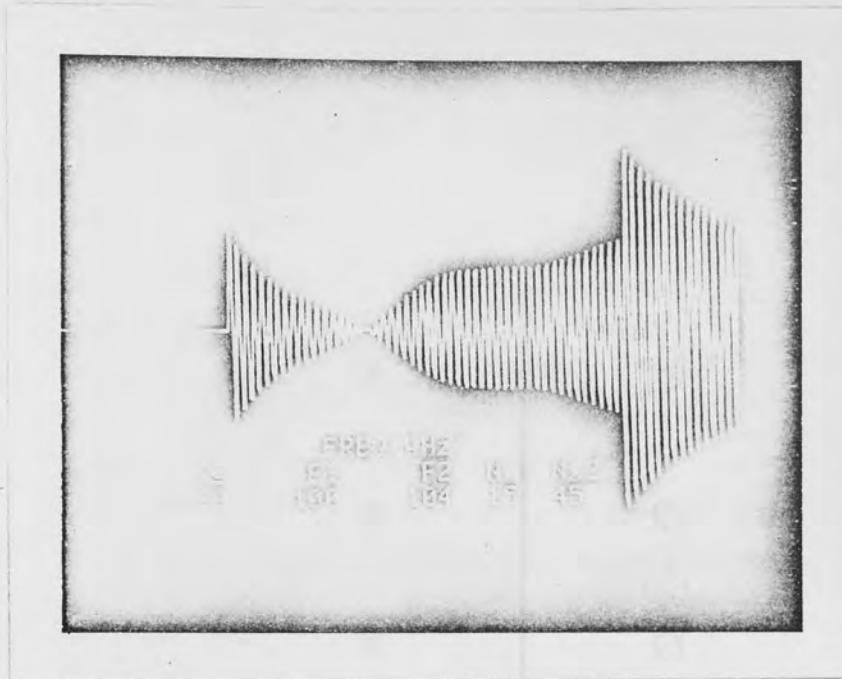
Figure 2.12
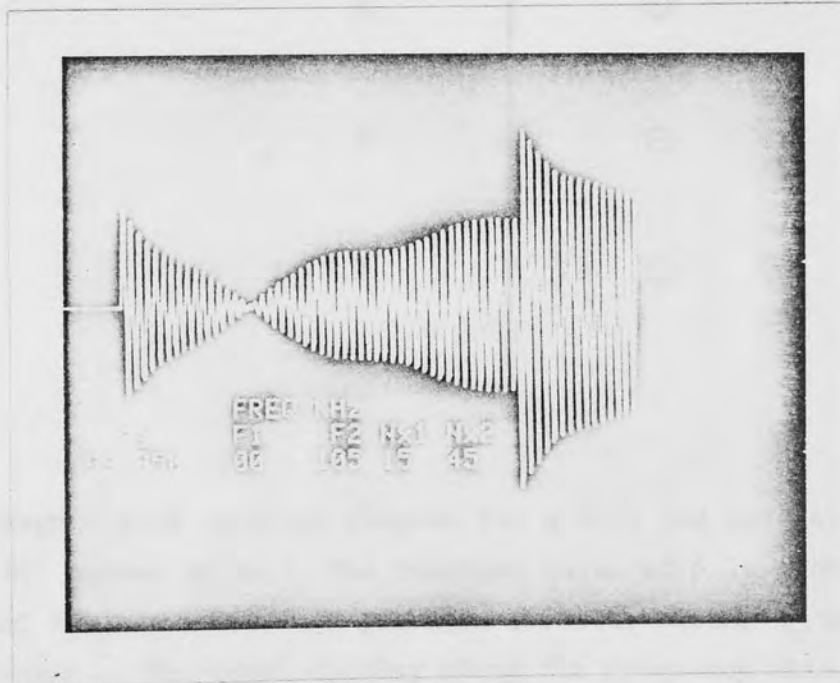
Figure 2.13 Fig. 2.11 - 2.13 show the echo pattern of
two resonant modes with a frequency separation of 1 - 5%.
The signal frequency is changed to maintain the frequency
sensitive null. Here the signal frequency is not equal to
any mode frequencies. Although it is not shown, a crossover
is also observed with a signal frequency close to that of
second mode if the burst length is long enough.
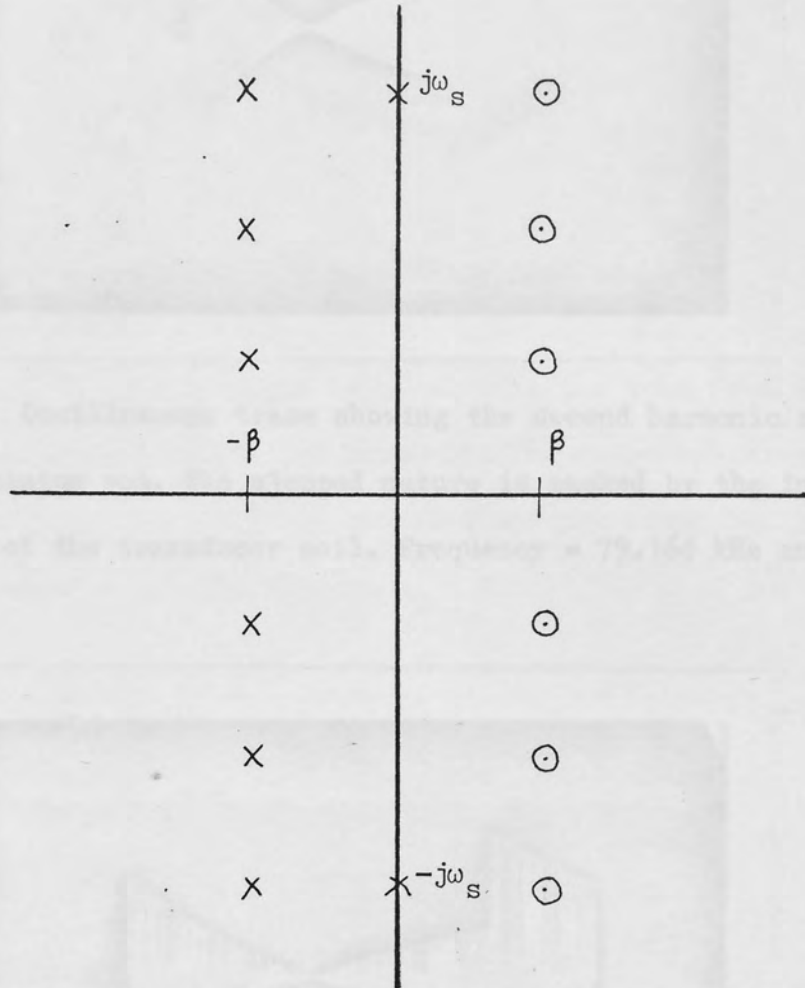
Figure 2.14   s-plane diagram for a thin rod resonator with
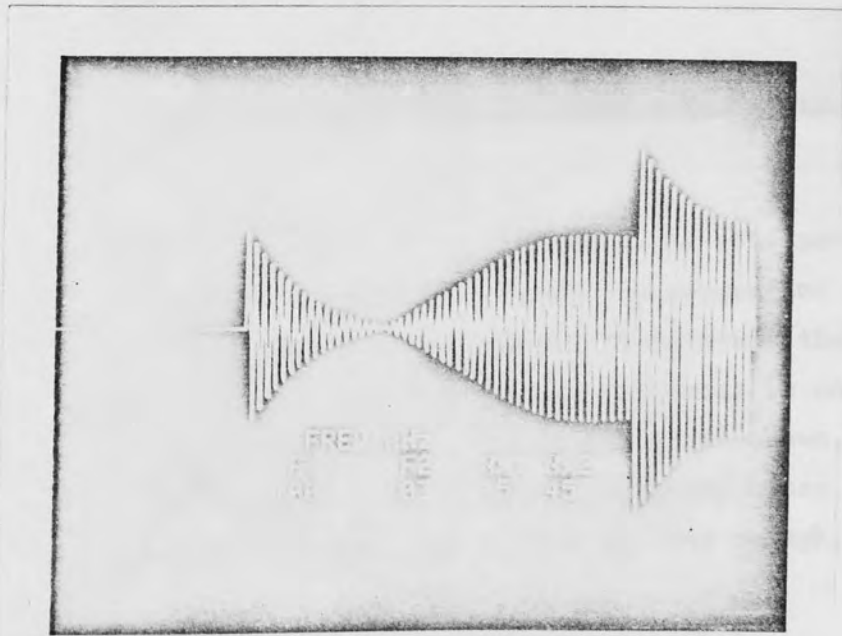'n' values up to 3. The constant value of β is a characteristic
of this resonator and produces a linear rising Q_c with mode
order n. The equal spacing along the frequency axis shows the
harmonic mode relationship.

Fig. 2.15 Oscilloscope trace showing the second harmonic resonance of an aluminium rod. The stepped nature is masked by the inherent bandwidth of the transducer coil. Frequency = 79.164 kHz and n_x= 30.
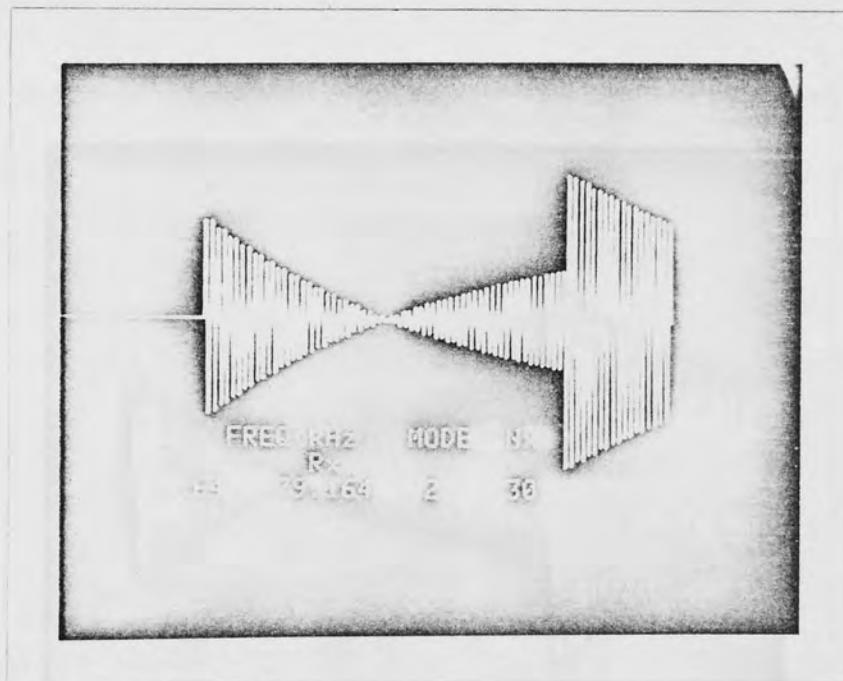
Fig. 2.16 The resulting computer plot corresponds to the resonator shown in fig. 2.15. The steps are well defined as the computer model assumes a large transducer bandwidth.

T_x : transmitting frequency

R_x : resonanting frequency
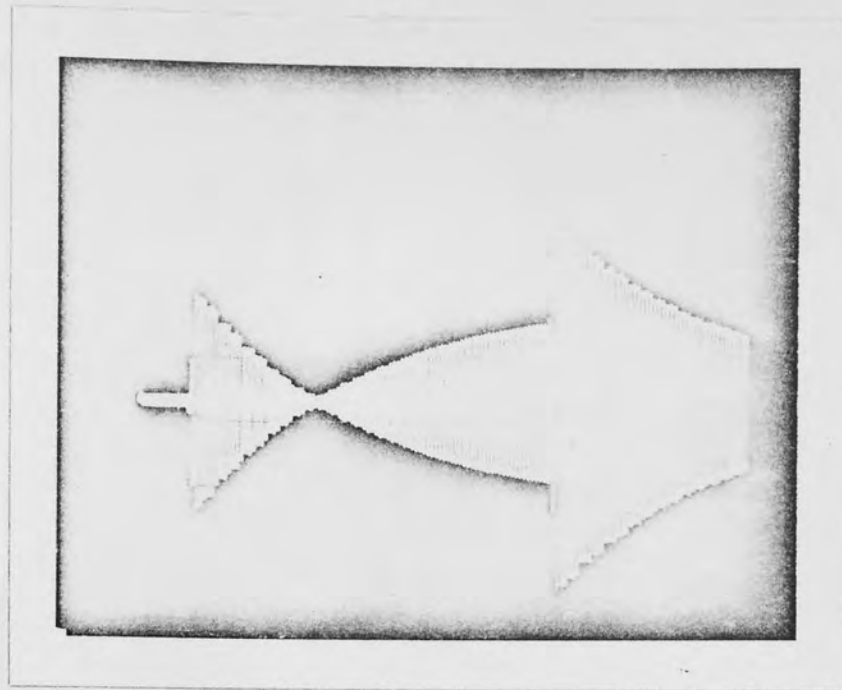
Fig. 2.17 Oscilloscope trace showing the echo from the
aluminium rod at its 3rd harmonic. The decrement step is
clearly shown with three oscillations per step.
Frequency = 118.490 kHz and n_x = 30 .
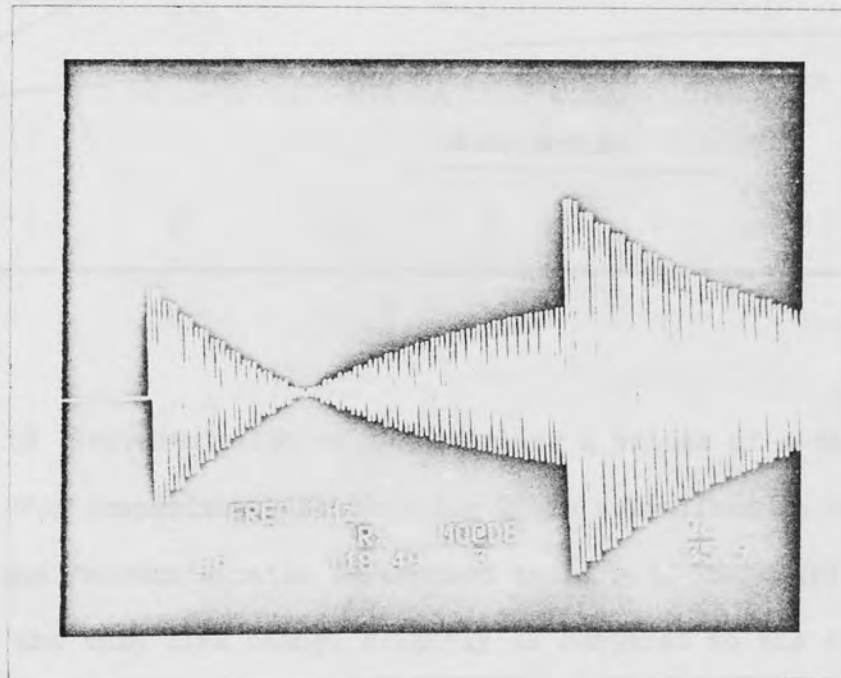
Fig. 2.18 The echo plot using the s-plane model with three
arbitrary modes. The data are obtained from the observation
shown in fig. 2.17 . The agreement is excellent and the
stepped nature is well maintained.
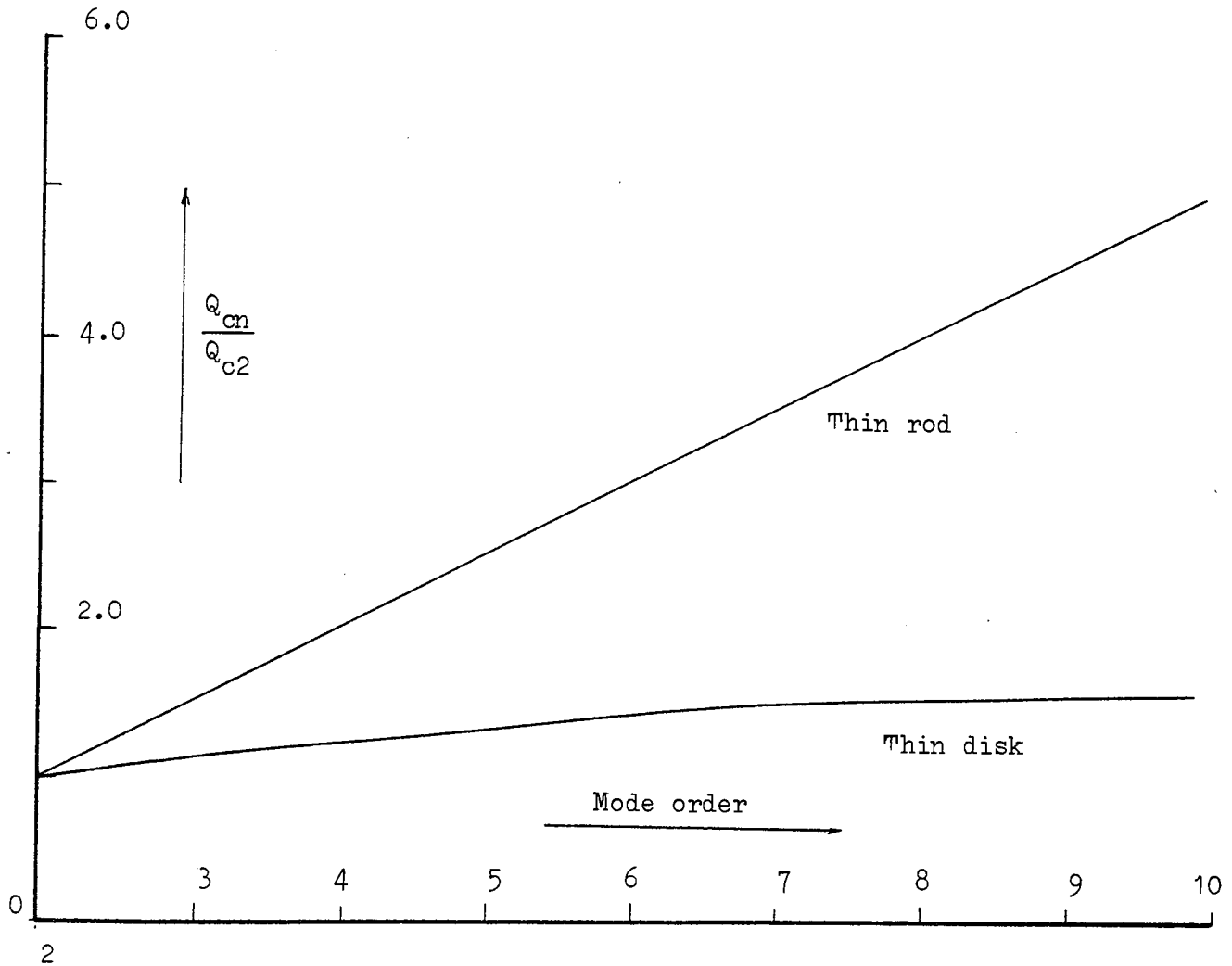
Figure 2.19 Representation of the coupling Q values of a thin rod and disk. For comparison, the coupling Q_c is normalised to the mode number 2 and Poisson's ratio is assumed to be 0.3. The coupling values of the thin disk change slightly as compared to the thin rod. This means that the n_x values of a thin disk vary insignificantly with mode order.
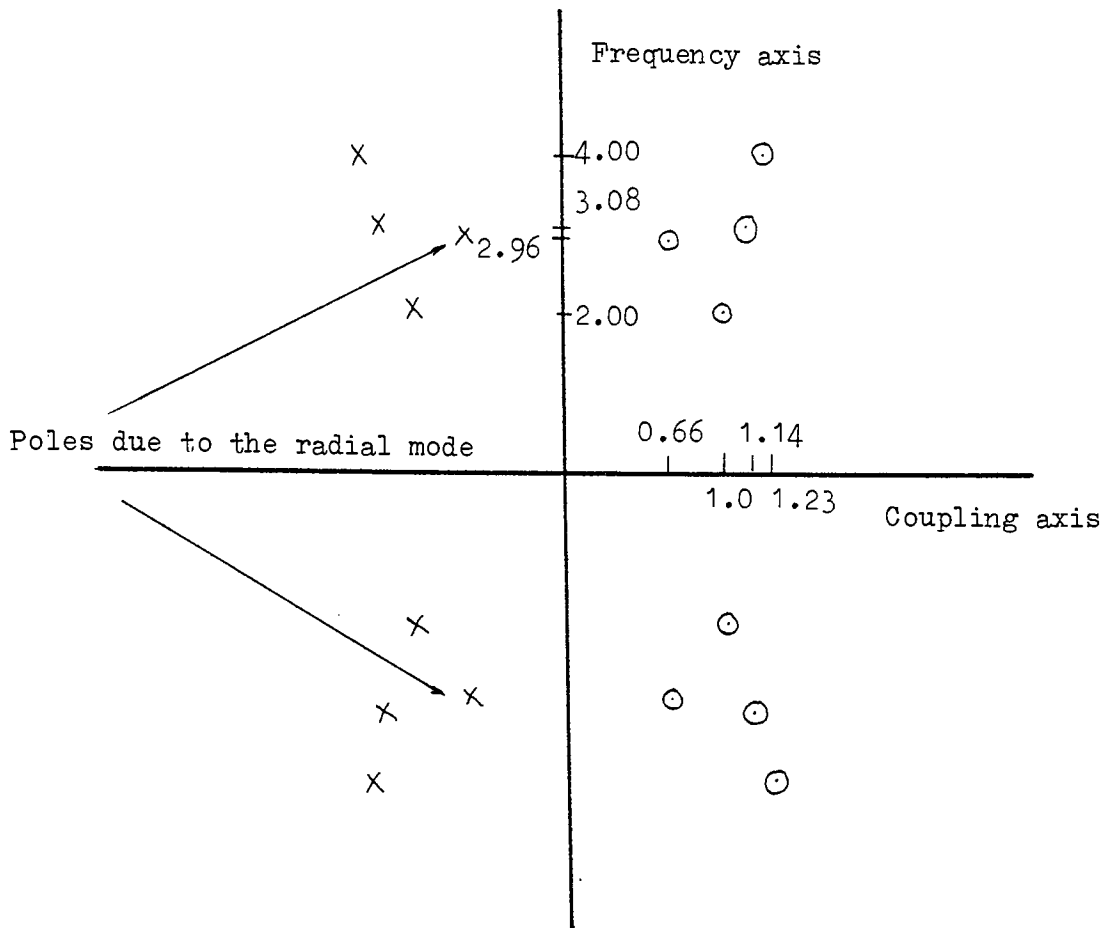
Figure 2.20 In this s-plane diagram, three contour modes (having

nodal diameters only) and the radial (breathing) modes are shown.

The Poisson's ratio is assumed to be 0.3. The vertical frequency

axis is normalised to $\frac{1}{2}\omega_{1,2}$ and horizontal coupling axis to $\beta_{1,2}$.

The frequencies here are not harmonic; unlike the thin rod resonator,

the coupling increases slowly with mode order 'n'.
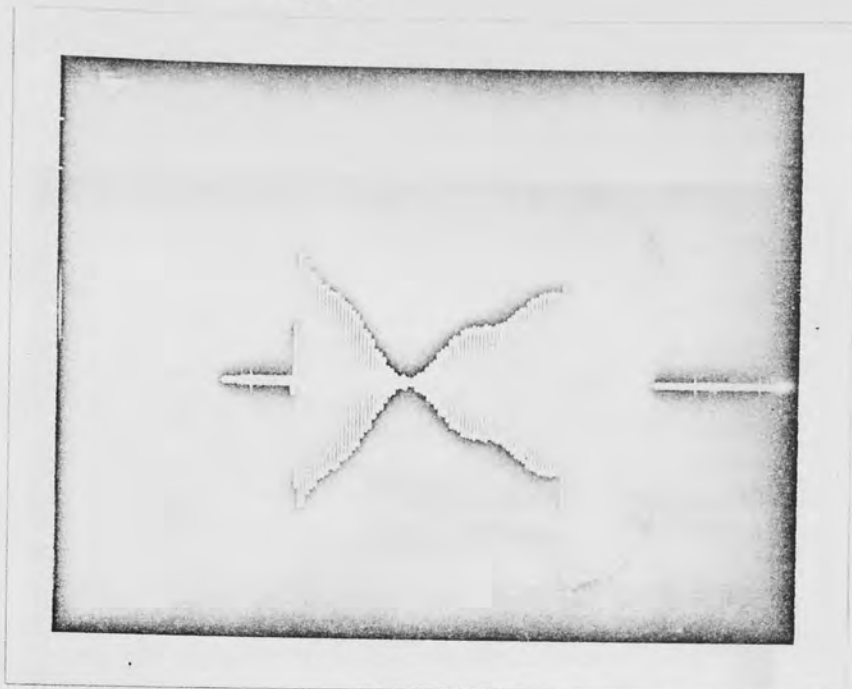
Figure 2.21 Oscilloscope display showing the echo pattern
of a steel disk (σ=0.287) at the mode with three nodal
diameters (1,3). The nature of stepped decrement and interaction
from the adjacent radial mode can be observed.
Signal frequency = 73.682 kHz.
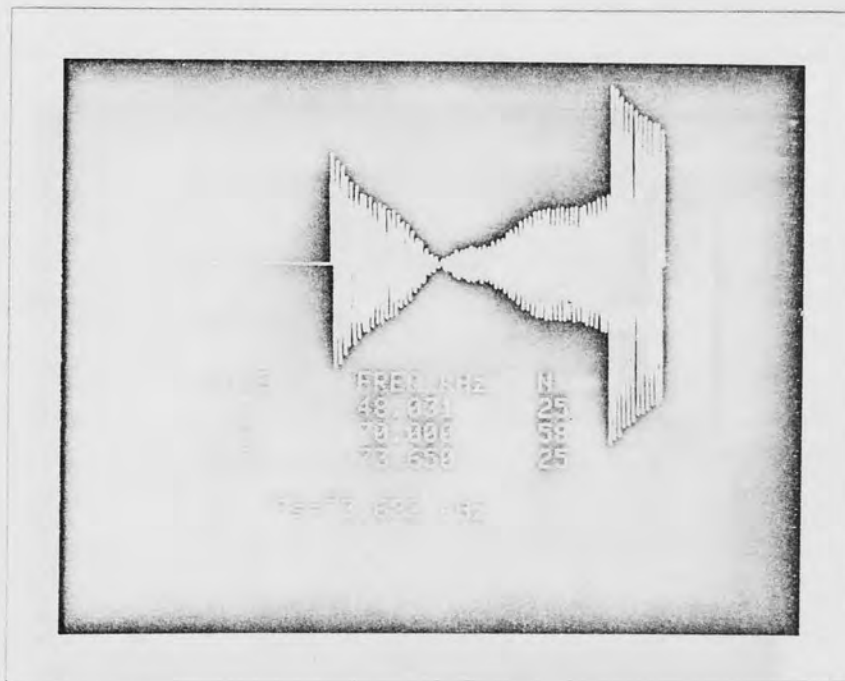
Figure 2.22 The computer plot for the particular case
shown above. This shows a combination of two mode frequencies
at 70.000 and 73.650 kHz. It is the only one to give a
crossover with a signal frequency of 73.682 kHz. The
steps disappear if 1,2 mode is omitted from the model.
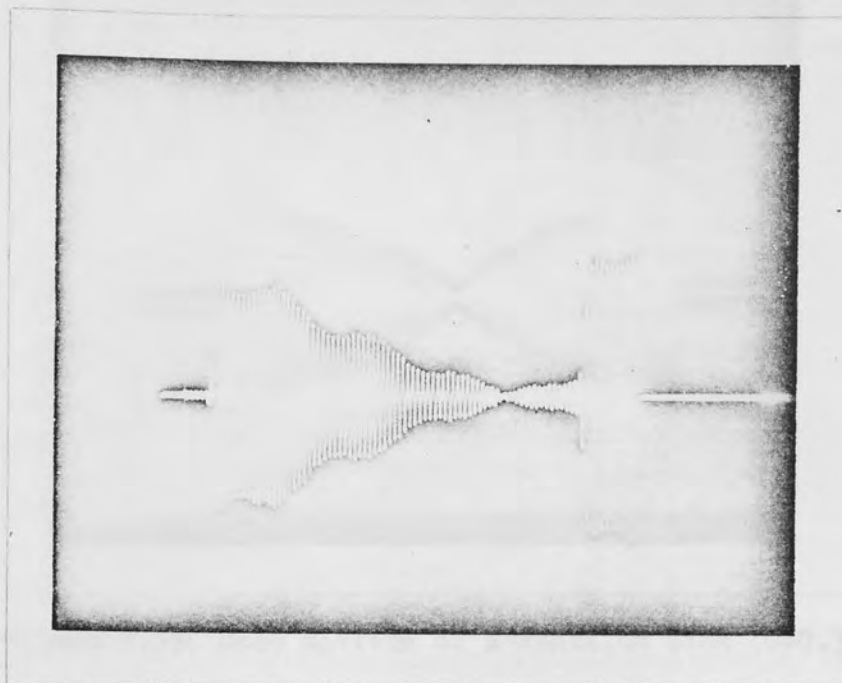
Figure 2.23 The pattern obtained from the steel disk
of fig.2.21 driven at its radial mode (1,R) frequency 69.991 kHz.
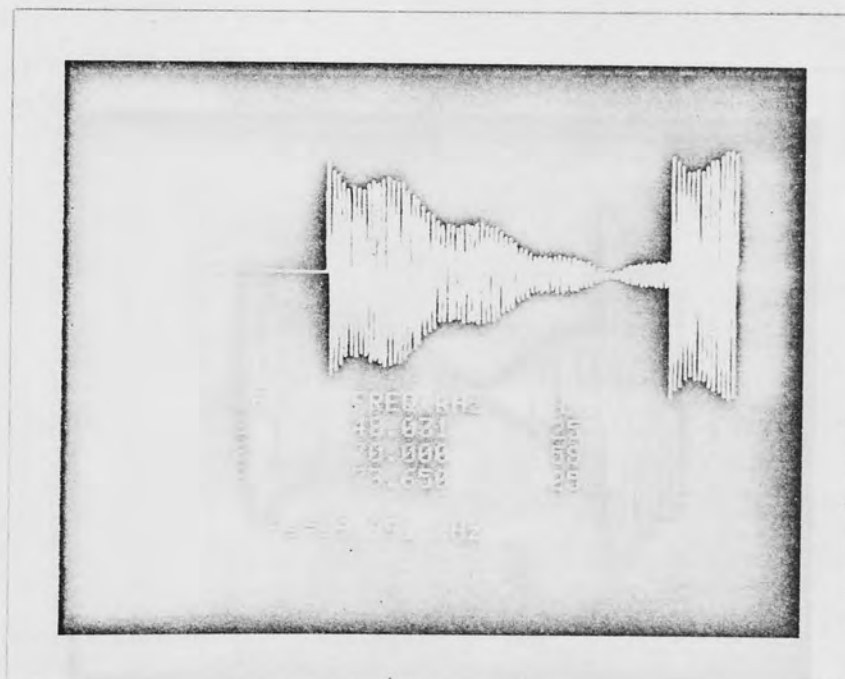
Figure 2.24 The resulting computer plot with the data
obtained from fig.2.22. The signal frequency in this case
corresponds to the experimental values. The agreement is
excellent demonstrating the validity of the model being
developed.
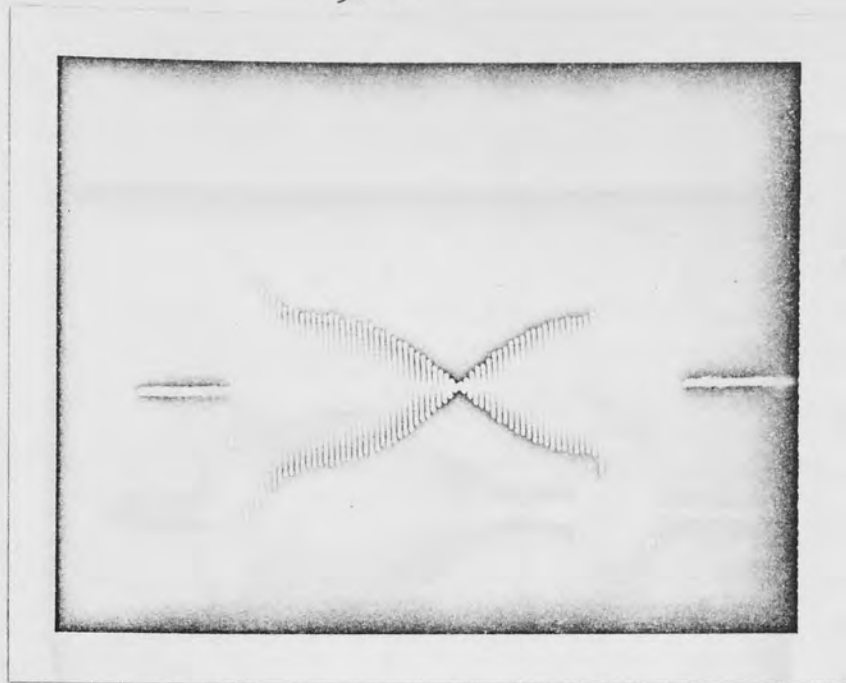
Figure 2.25 Echo pattern of a tantalum disk (σ=0.362)
resonanting at 1,3 mode with frequency 61.668 kHz. As
in the case of the steel disk, the stepped nature and
interaction from an adjacent mode are evident. But the
form of the echo is quite different because the coupling
term is smaller and the adjacent frequency is even closer.
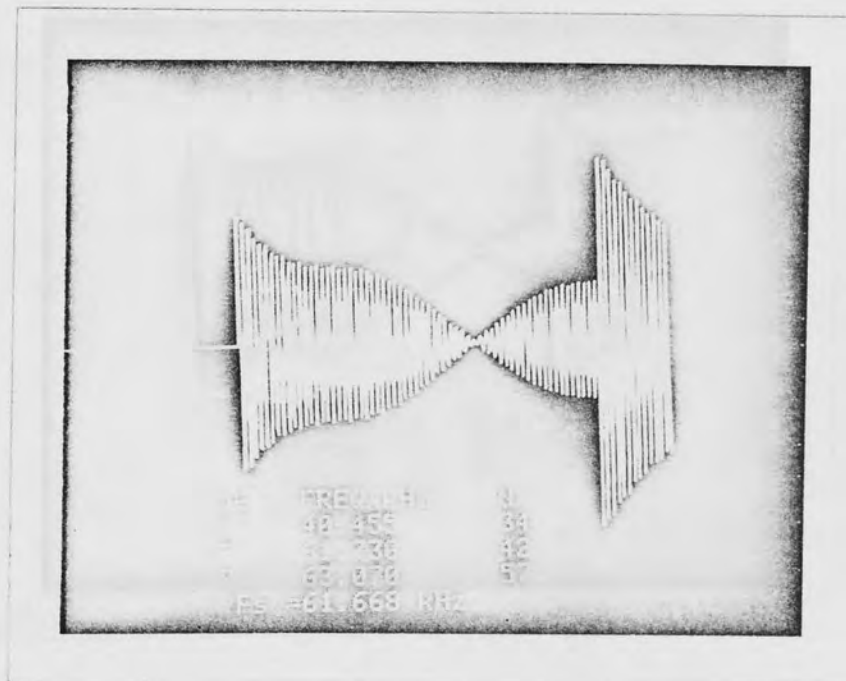
Figure 2.26 The computer echo pattern corresponding to
the case shown above. The pattern is still well matched
to the oscilloscope display.
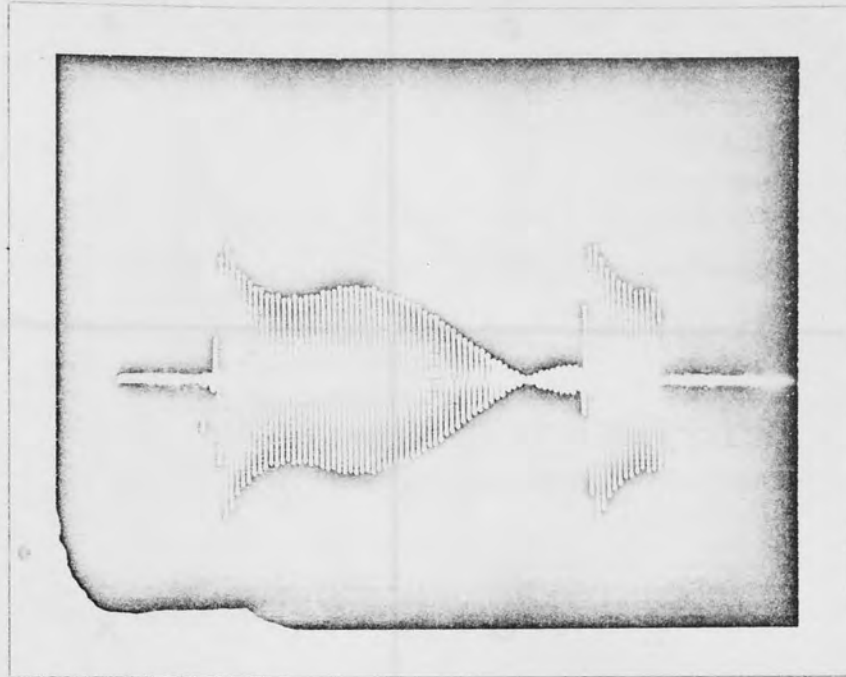
Figure 2.27 As in fig. 2.25, the tantalum disk resonanting
at 1,R mode with frequency 63.090 kHz.
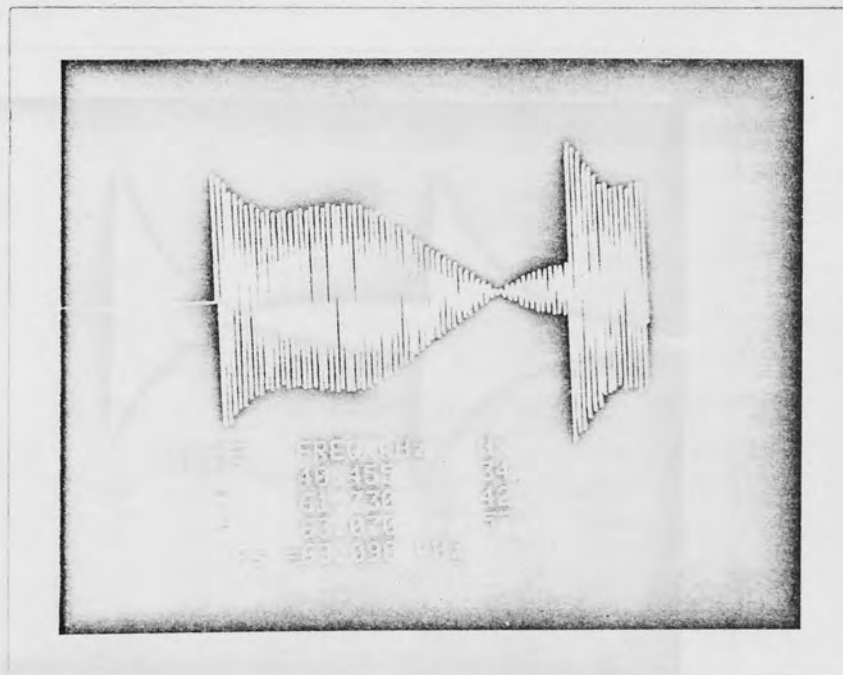
Figure 2.28 The resulting computer plot with the experimental
data. Here the actual frequency separation is 2.17% rather
than the experimental value of 2.31%. This enables an
improved value of Poisson's ratio to be obtained.
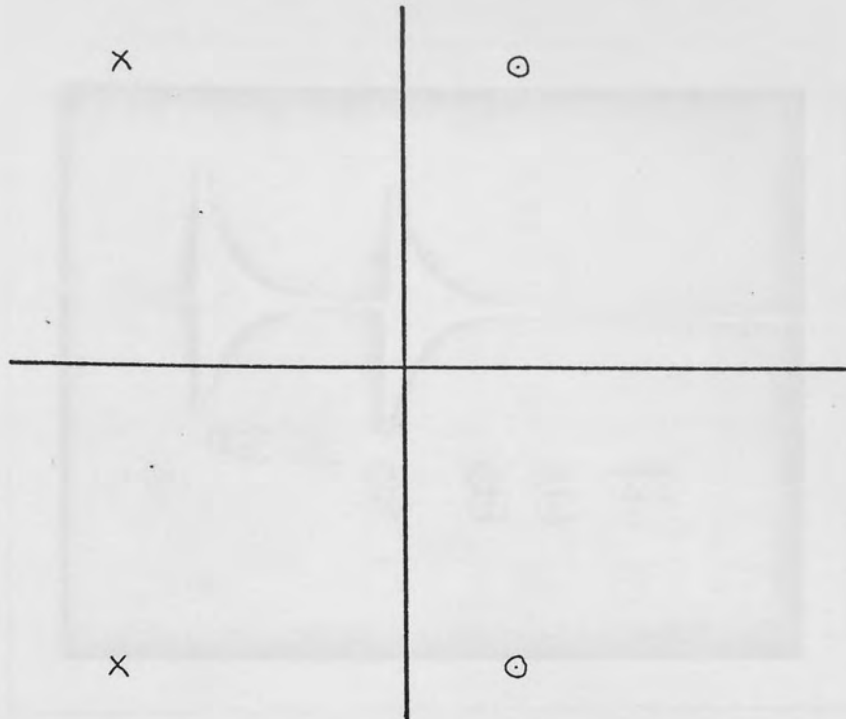
Figure 2.29 s-plane diagram of a single resonance including material losses. The data points are no longer symmetrical about the frequency axis.
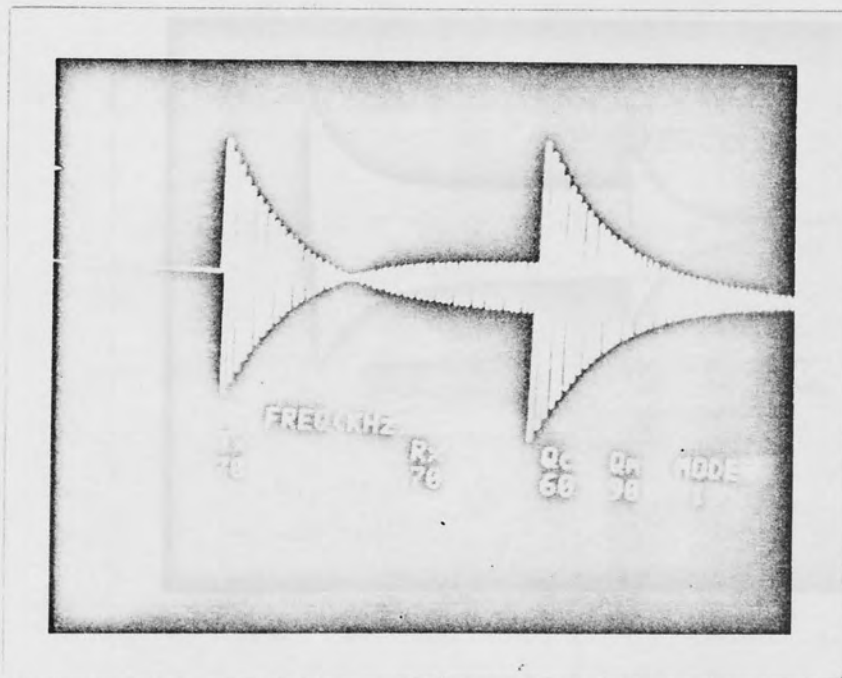
Figure 2.30 The echo pattern corresponding to the case shown above. The steady state amplitude is now considerable less than the initial value.
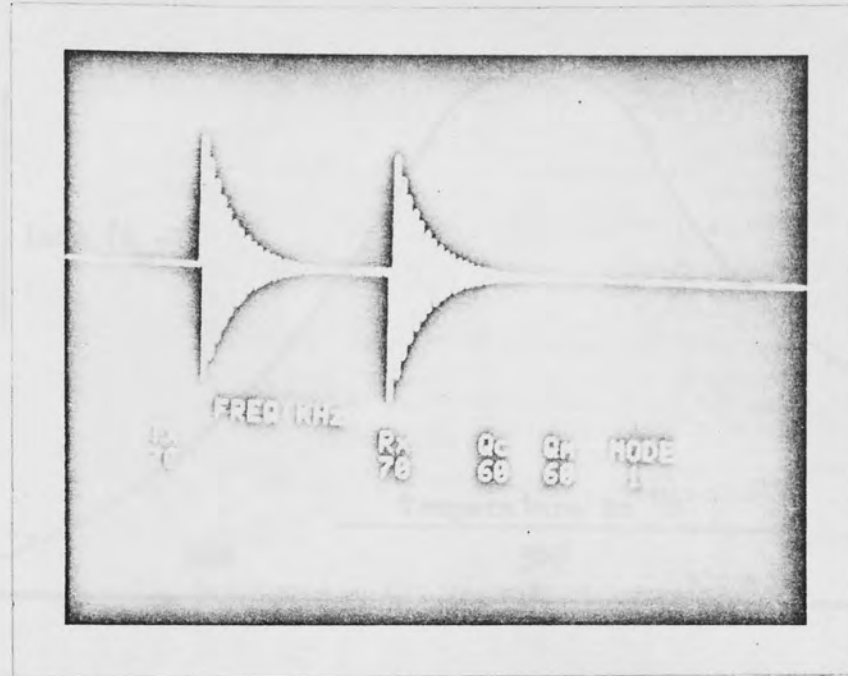
Figure 2.31   The echo pattern when $Q_c = Q_m$ showing the steady state amplitude is zero. In this case, the echo expression is simply

$$\exp(-2\beta t)\sin\omega_s t\left[H(t) - H(t-\tau)\right].$$
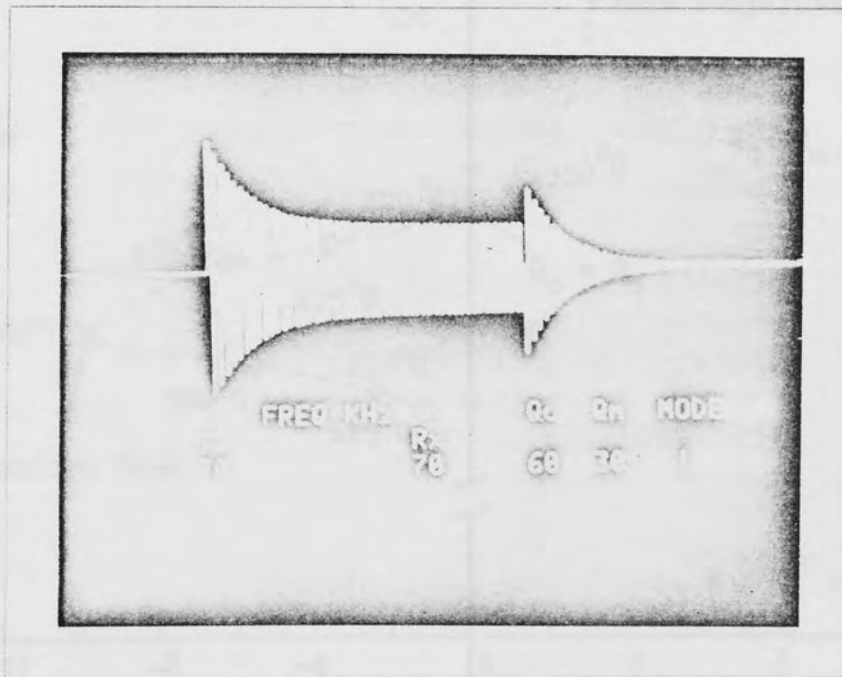
Figure 2.32   When $Q_c > Q_m$, the null of the echo pattern is lost due to most of the energy being dissipating inside the resonator.
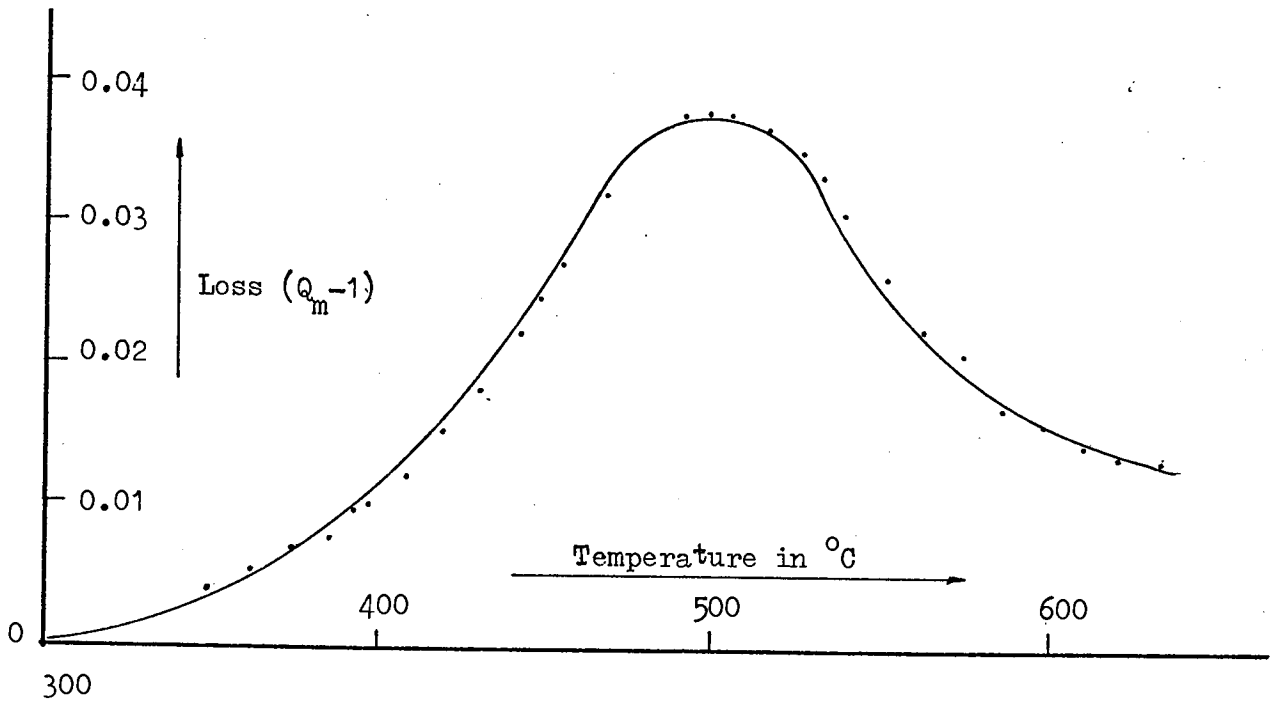
Fig. 2.33 The variation of material losses for an
aluminium disk with temperature. A peak is observed at 500°C.
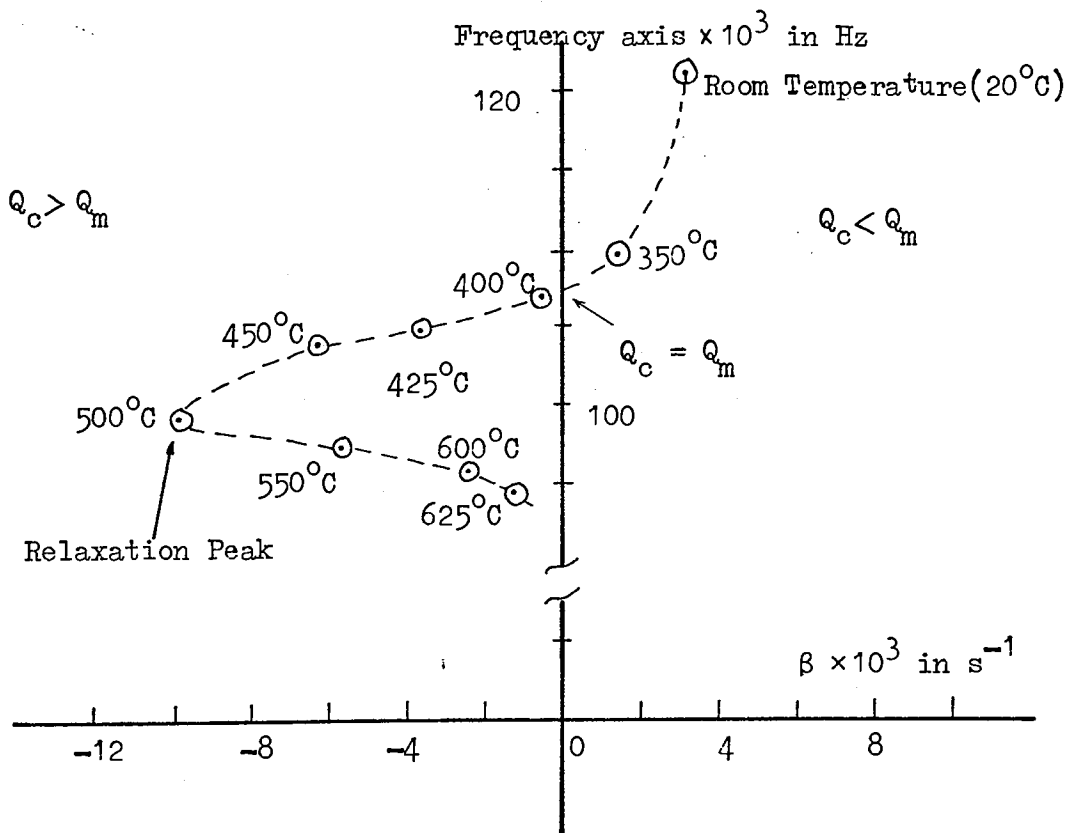
Fig. 2.34 s-plane zero locus diagram with temperature as
a parameter. The corresponding pole has a similar locus but
displaced by an amount dependent on the coupling term.

Poisson's Ratio MODE	$\dfrac{M_{eq}}{M}$					
	0	0.1	0.2	0.3	0.4	0.5
1,2	0.4778	0.4932	0.5056	0.5158	0.5242	0.5314
1,3	0.3347	0.3532	0.3689	0.3823	0.3936	0.4037
1,4	0.2764	0.2932	0.3082	0.3215	0.3331	0.3434
1,5	0.2410	0.2563	0.2705	0.2831	0.2945	0.3046
1,6	0.2154	0.2296	0.2429	0.2550	0.2659	0.2758
1,7	0.1953	0.2086	0.2211	0.2327	0.2432	0.2528
1,8	0.1788	0.1914	0.2033	0.2144	0.2246	0.2338
1,9	0.1651	0.1770	0.1884	0.1990	0.2088	0.2177
1,10	0.1534	0.1648	0.1756	0.1858	0.1952	0.2039
1,R	0.7050	0.7317	0.7562	0.7832	0.8111	0.8401

Table 2.1 Calculated $\dfrac{M_{eq}}{M}$ for the in-plane modes of circular disks as a function of Poisson's ratio.

($\dfrac{M_{eq}}{M}$ = ratio of edge equivalent mass to static mass)

MODE	1mm Nickel Line Drive				0.7mm Nickel Line Drive			
	Frequency(KHz)	n_x	Q_c	$Z_x = 2\pi f \dfrac{\frac{1}{2}M}{Q_c}$ (Ω)	Frequency(KHz)	n_x	Q_c	Z(Ω)
2	33.081	20	90.647	28.72	33.101	41	185.73	14.024
3	49.549	30	135.97	28.622	49.552	62	280.86	13.883
		mean Z_x	=	28.671		mean Z_x	=	13.954

Table 2.2 The experimental line impedance data from a brass rod of 100mm long
and static mass (M) of 25.047 gm.

8

Poisson's Ratio of the aluminium disk = 0.340

Diameter of the aluminium disk = 35.50 mm

Thickness = 1.56 mm

Static mass (M) = 3.88 gm

Driven line impedance (Z) = 13.954Ω

MODE	Frequency(KHz)	n_x	$\dfrac{M_{eq}}{M}$ (Exp.)$=\dfrac{Z\ n_x}{f\ M\ 2\log_e 2}$	$\dfrac{M_{eq}}{M}$(Cal.)
1,2	66.704	13	0.5056	0.5193
1,3/1,R	102.711	11	-	0.3871
1,4	134.042	18	0.3484	0.3263
1,5	163.361	18	0.2859	0.2878
1,6	192.626	17	0.2290	0.2595

Table 2.3 Calculated and experimental $\dfrac{M_{eq}}{M}$ values on an aluminium disk. The equivalent mass (M_{eq}) is normalised to the static mass (M).

Poisson's Ratio of the brass disk = 0.355

Diameter of the brass disk = 53.848 mm

Thickness = 1.5 mm

Static mass (M) = 35.15 gm

Driven line impedance (Z) = 28.671 Ω

MODE	Frequency(KHz)	n_x	$\dfrac{M_{eq}}{M}$ (Exp.)	$\dfrac{M_{eq}}{M}$ (Cal.)
1,2	30.506	27	0.5208	0.5202
1,3	46.976	31	0.3883	0.3882
1,4	61.412	36	0.3449	0.3275
1,5	74.904	37	0.2906	0.2890
1,6	87.890	36	0.2410	0.2606
1,R	48.591	60	0.7265	0.7970

Table 2.4 The normalised edge equivalent mass of a brass
disk associated with the first five asymmetric and the
pure radial in-plane modes.

Poisson's Ratio of the steel disk = 0.287

Diameter of the steel disk = 50.80 mm

Thickness = 1.50 mm

Static mass (M) = 23.193 gm

Driven line impedance (Z) = 13.954 Ω

MODE	Frequency(KHz)	n_x	$\frac{M_{eq}(Exp.)}{M}$	$\frac{M_{eq}(Cal.)}{M}$
1,2	48.148	52	0.4687	0.5148
1,3	73.822	63	0.3704	0.3810
1,4	96.250	67	0.3021	0.3200
1,5	116.305	70	0.2612	0.2819
1,R	70.103	112	0.6934	0.7805

Table 2.5 As in table 2.3 and 2.4, this shows the normalised
edge equivalent mass of a steel disk.

CHAPTER 3

ONE DIMENSIONAL RAYLEIGH WAVE ON STRIPS

CHAPTER 3

ONE DIMENSIONAL RAYLEIGH SURFACE WAVE ON STRIPS

3.1 Introduction

In 1855, Lord Rayleigh[14] showed mathematically that
acoustic waves can propagate on the surface of isotropic
materials. He pointed out that the energy of such waves
spreading in two dimensions only, would fall off in inverse
proportion to the distance while in the three dimensional case,
the inverse square law applies. The application of his ideas
to the study of the earth's crust have led a better
understanding of energy propagation from earthquake zones and
these surface waves have since been known as "Rayleigh Waves".
With the recent application of surface wave to microelectronics,
many review articles of these waves appear in the literature.
White[15] has given a good description of the physics of
surface acoustic waves (SAW). The low velocity, the ease of
access to the signal and their non-dispersive characteristic
have led to significant applications in the field of signal
processing and non-destructive testing. The annual I.E.E.E.
Ultrasonic Symposium[16] and Surface Wave Abstracts[17] provide
an up to date account of references to SAW.

The work described here establishes theoretically and
experimentally that Rayleigh waves can also propagate on the
edges of various geometrical structures, they are then one
dimensional and suffer no spreading loss. In common with two
dimensional waves, the energy is confined to the boundary and
the waves are non-dispersive for a straight edge. Because of

these features, microsound waveguides consisting of a ridge
above a surface make the basis of the ridge waveguides of
Mason and Ash[18].

They first reported the existence of two propagation modes
in which the displacements are horizontal and vertical in
ridge guides for SAW. They make use of a transverse (flexural)
wave which has a very low phase velocity and is highly
dispersive. Rayleigh waves, which are the subject of this work
have no transverse component, their displacement being in depth
and parallel to the direction of propagation. The other ridge
mode is similar to the one dimensional Rayleigh wave of this
investigation. Hitherto, no extensive study[19] has been made
of these waves, probably due to the difficulty in their
generation. Using the wire drive technique, however strong
coupling is obtained and this has led to the experimental and
theoretical studies described here.

For theoretical analysis, the plate thickness is assumed
to be indefinitely small in comparison with the wavelength.
The frequency equation is obtained by considering the edge
itself and assuming the existence of a surface wave. It will
be shown that the Rayleigh-Lamb frequency equation converges
to the same form at small wavelength in an indefinitely thin
plate.

The particle displacement on the free edges of an infinite
strip follows the two dimensional case very closely. The
phase velocity is slightly lower than that of the two
dimensional case except at Poisson's ratio equal to zero where

the velocities are equal. In both cases, the waves are non-dispersive i.e. phase and group velocities are equal. The pulse-echo technique previously described in Chapter 2 has been used to test the theoretical results and gives an excellent verification.

3.2 The Derivation of Elastic Wave Equation of an Unbounded Plates

The most general expression for the behaviour of an extended elastic isotropic solid under dynamic conditions is obtained by the application of Newton's third law to an element of the bulk material. This, in carterian form gives the well known wave equation shown in equation (3.1).

$$
\begin{bmatrix} \sigma_{xx} & T_{xy} & T_{xz} \\ T_{yx} & \sigma_{yy} & T_{yz} \\ T_{zx} & T_{zy} & \sigma_{zz} \end{bmatrix} \begin{bmatrix} \frac{\partial}{\partial x} \\ \frac{\partial}{\partial y} \\ \frac{\partial}{\partial z} \end{bmatrix} = \rho \frac{\partial^2}{\partial t^2} \begin{bmatrix} u_x \\ u_y \\ u_z \end{bmatrix} \tag{3.1}
$$

Further abbreviation gives the concise vector form of equation (3.1a).

$$
C_B^2 \Delta \nabla - 2C_S^2 \nabla \times \bar{\omega} = \ddot{u}
$$

$$
\Delta = DIV\ u \qquad \bar{\omega} = \frac{1}{2}\ curl\ u
$$

C_B and C_S are the bulk and shear velocities respectively

σ_{ij} and T_{ij} the longitudinal and shear component defined by their subscripts

u : displacement vector

For the case of a strip, the shear strains are in one plane and appears as e_{xx}, e_{xz}, e_{zz} and e_{yz}, e_{xy}, e_{yy} being zero (see Fig. 3.1). This leads to the result that the shear

stresses T_{xy}, T_{yz} vanish. Furthermore, in the nature of the wave, there is no particle displacement in y direction other than that arising from the Poisson's ratio. This leaves the term σ_{yy}. In the case of plane stresses in the xz plane, the components σ_{yy}, T_{xy} and T_{yz} are zero, but the displacement u_y is possible, thus introducing the plate rather than the bulk modulus of the equation. Therefore, the elastic wave equation reduces to the two dimensional form as

$$
\begin{bmatrix} \sigma_{xx} & T_{xz} \\ T_{zx} & \sigma_{zz} \end{bmatrix} \begin{bmatrix} \frac{\partial}{\partial x} \\ \frac{\partial}{\partial y} \end{bmatrix} = \rho \, \frac{\partial^2}{\partial t^2} \begin{bmatrix} u_x \\ u_z \end{bmatrix} \tag{3.2}
$$

For isotropics materials in general[20]

$$
\begin{bmatrix} e_{xx} \\ e_{yy} \\ e_{zz} \end{bmatrix} = \frac{1}{E} \begin{bmatrix} 1 & -\sigma & -\sigma \\ -\sigma & 1 & -\sigma \\ -\sigma & -\sigma & 1 \end{bmatrix} \begin{bmatrix} \sigma_{xx} \\ \sigma_{yy} \\ \sigma_{zz} \end{bmatrix} \tag{3.3}
$$

$$
\begin{bmatrix} T_{xy} \\ T_{yz} \\ T_{xz} \end{bmatrix} = \mu \begin{bmatrix} \frac{\partial}{\partial y} & \frac{\partial}{\partial x} & 0 \\ 0 & \frac{\partial}{\partial z} & \frac{\partial}{\partial y} \\ \frac{\partial}{\partial z} & 0 & \frac{\partial}{\partial x} \end{bmatrix} \begin{bmatrix} u_x \\ u_y \\ u_z \end{bmatrix} \tag{3.3a}
$$

For the case of a strip, it simplifies to

$$
\begin{bmatrix} \sigma_{xx} \\ \sigma_{zz} \end{bmatrix} = \rho \begin{bmatrix} c_p^2 & c_p^2 - c_s^2 \\ c_p^2 - c_s^2 & c_p^2 \end{bmatrix} \begin{bmatrix} \frac{\partial u_x}{\partial x} \\ \frac{\partial u_z}{\partial z} \end{bmatrix} \tag{3.4}
$$

$$
T_{xz} = \rho \, c_s^2 \left[\frac{\partial u_x}{\partial z} + \frac{\partial u_z}{\partial x} \right] \tag{3.4a}
$$

Substitute (3.4), (3.4a) into equation (3.2) gives

$$C_p^2 \frac{\partial}{\partial x} \left[\frac{\partial u_x}{\partial x} + \frac{\partial u_z}{\partial z} \right] + C_s^2 \frac{\partial}{\partial z} \left[\frac{\partial u_x}{\partial z} - \frac{\partial u_z}{\partial x} \right] = \frac{\partial^2 u_x}{\partial t^2}$$

$$C_p^2 \frac{\partial}{\partial z} \left[\frac{\partial u_x}{\partial x} + \frac{\partial u_z}{\partial z} \right] + C_s^2 \frac{\partial}{\partial x} \left[\frac{\partial u_z}{\partial x} - \frac{\partial u_x}{\partial z} \right] = \frac{\partial^2 u_z}{\partial t^2}$$

(3.5)

Equation (3.5) can be written in the same vector form as equation (3.1a).

$$C_p^2 \nabla_2 \Delta - 2 C_s^2 \nabla_2 \times \bar{\omega} = \ddot{\bar{u}}$$

(3.5a)

The subscript (2) here denotes that the dimension of elastic wave equation is two. Compare equation (3.5a) to (3.1a), it shows they differ by replacing C_B by C_p.

3.3 Rayleigh Wave on the Edge of an Infinite Strip

Equation (3.5a) can be analysed to derive the properties of plane Rayleigh surface waves, (their velocity being designated C_{1R}) along the x axis on the straight edge of an infinite isotropic strip. The particle displacement u may be expressed in terms of scalar potential ϕ and a vector potential ψ. Because the motion is independent on co-ordinate y and only the component of vector potential ψ along the y axis has a non-zero magnitude, this is denoted as $\psi\hat{y}$; therefore

$$u = \nabla\phi + \nabla \times (\psi\hat{y}) \tag{3.6}$$

In using equation (3.5a) and Helmholtz's theorem[21], the potential ϕ and ψ satisfy the following equations of wave motion,

$$\nabla^2\phi = \frac{1}{C_p^2} \frac{\partial^2\phi}{\partial t^2}$$

$$\tag{3.7}$$

$$\nabla^2\psi = \frac{1}{C_s^2} \frac{\partial^2\psi}{\partial t^2}$$

∇^2 : the Laplace operator of continuity.

By working in parallel with the two dimensional case, equation 3.7 leads to the expression for ϕ and ψ as

$$\phi = A \exp(-gz) \exp(i(2\pi ft - \frac{2\pi}{\lambda}x))$$

$$\psi = B \exp(-pz) \exp(i(2\pi ft - \frac{2\pi}{\lambda}x)) \tag{3.8}$$

where

$$g^2 = (\frac{2\pi}{\lambda})^2 - (\frac{2\pi f}{C_p})^2$$

$$p^2 = (\frac{2\pi}{\lambda})^2 - (\frac{2\pi f}{C_s})^2$$

For a stress free surface at z=0, the boundary conditions in terms of ϕ and ψ are

$$\sigma_{zz} = \rho\, C_p^2 [\frac{\partial^2 \phi}{\partial z^2} + \frac{\partial^2 \psi}{\partial x \partial z} + \sigma(\frac{\partial^2 \phi}{\partial x^2} - \frac{\partial^2 \psi}{\partial x \partial z})] = 0$$

$$\tag{3.9}$$

$$T_{xz} = \rho\, C_s^2 [\frac{\partial^2 \phi}{\partial x \partial z} + \frac{1}{2}(\frac{\partial^2 \psi}{\partial x^2} - \frac{\partial^2 \phi}{\partial z^2})] = 0$$

To obtain a non-trivial solution for the unknowns A and B, the determinant of their coefficient matrix must vanish. When the determinant of the coefficient matrix is set equal to zero, it is known as frequency equation. This is obtained by substituting equation (3.8) into (3.9).

$$(R_0 - 2)^2 = 4(1 - \frac{R_0^2}{B^2})^{\frac{1}{2}} (1 - R_0^2)^{\frac{1}{2}} \tag{3.10}$$

where R_0 is the Rayleigh wave velocity normalized to the shear velocity, i.e. C_{1R}/C_s .

Inspection shows that the equation for the one dimensional case differs from that of two dimensions in that the two

dimensional modulus factor $B^2 = \frac{1-2\sigma}{2(1-\sigma)}$ is replaced by $\frac{1-\sigma}{2}$, σ here being Poisson's ratio. Again, the absence of a wavelength term shows the velocity to be non-dispersive. The root of R_o corresponds to the one dimensional Rayleigh wave which lies bewteen 0 and 1. Figure 3.2 shows the calculated value of the two velocities for a wide range of Poisson's ratio. It will be seen that the surface wave which propagates along an edge always has a lower velocity than that on a flat surface. The velocities and eigenfunctions are equal at $\sigma=0$ when both B^2 terms are 1/2. Both velocities are less than the shear velocity for all possible values of σ. Equation (3.11) gives the components u_x and u_z of the particle displacement along the x and z axes respectively by using equations (3.6), (3.8) and (3.9).

$$u_x = A \frac{2\pi}{\lambda}\left[\exp(-gz) - \frac{2pg \exp(-pz)}{p^2 + (\frac{2\pi}{\lambda})^2}\right] \sin(2\pi ft - \frac{2\pi}{\lambda} x)$$

$$(3.11)$$

$$u_z = A g \left[\exp(-gz) - \frac{2(\frac{2\pi}{\lambda})^2 \exp(-pz)}{p^2 + (\frac{2\pi}{\lambda})^2}\right] \cos(2\pi ft - \frac{2\pi}{\lambda}x)$$

Fig. 3.3 shows the variation with depth of displacement amplitude u_x and u_z for the two cases in a Rayleigh wave case. The displacement amplitude is normalized to the vertical displacement u_z at z=0. It is apparently that the two patterns of displacement follow very closely, with the exception that the displacements parallel to the propagated direction change sign at a depth 0.19λ and 0.17λ in the one and two dimensional cases respectively (assumed $\sigma=0.34$). Fig. 3.4a

and 3.4b show the two energy distributions with depth. The energy is normalized to the value associated with z=0. Carrying out the numerical calculation, for σ=0.34, it was found that 50% of energy is above 0.1825λ and 99% above 1.10λ for the one dimensional case. For two dimensions, the figures are 0.242λ and 1.15λ. It follows that the energy in one dimensional surface waves is slightly nearer the edge except for σ=0, they are equal. Since the particle motion at the free boundary is less constrained than the free surface, a lower phase velocity is expected. Because of this lower phase velocity, the energy does not propagate into the interior of the medium and has a smaller penetration effect. Table 3.1 shows the general comparison for two cases.

3.4 Experiment

Two velocity measurements are possible. By observing the time of travel of a burst of oscillation, the group velocity is obtained. Measurement of successive resonances associated with standing waves give the phase velocity. The latter, being in effect a resonance method is very much more accurate. The group velocity is readily obtained from the phase velocity by the relationship given in equation (3.12) and (3.13).

$$C_\phi = 2L \frac{f_n}{n} \qquad (3.12)$$

where f_n is the frequency for n standing waves

$$C_g = 2L \frac{df}{dn} \qquad (3.13)$$

where $\frac{df}{dn}$ is the frequency difference between successive resonances.

A simple and commonly used method of obtaining standing waves is by reflecting a forward travelling wave at a free boundary and examine the resonance arising from the result standing waves. This method is not possible for waves on a straight strip as reflection at a free boundary is accompanied by the considerable loss of energy due to mode conversion.

The line drive method previously described in Chapter 2 avoids this by exciting the edge with a double wire drive as

shown in Fig. (3.5). The two ends of the wire are fitted normally into the edge at a reasonable distance apart. The transducer coil is symmetrically placed for equal delays on each drive. The first echo return is the sum of the echo from each drive point and the second is that of the waves travelling clockwise and counter-clockwise round the circuit. The additional delay arises from Rayleigh waves on the strip. Both ends of the strip are covered with plasticine to remove any small reflection which might create additional signals. A burst of oscillation of sufficient duration is selected to combine both echoes. As the frequency is changed, the overlapping of the first and second echoes gives rise to maxima and minima and hence determines phase velocity. The electronic technique described in Appendix 1 provides a simple and quick method to determine the number of nodes 'n' along the edge.

Table 3.2 shows observations on the edge of a 1 mm thick aluminium strip with a drive separation of 342.9 mm. Figs. 3.6 and 3.7 show the oscilloscope displays for short and long oscillation bursts. A disk was cut from the same aluminium sheet and the precise values of Poisson's ratio plate and shear velocity were measured using the method described in Chapter 6 and included in Table 3.2.

From Table 3.2, the independence of Rayleigh wave velocity on wavelength is very apparent, confirming the non-dispersive characteristic and giving $C_\phi = C_g$. The ratio of C_{1R}/C_s is 0.9194 when compared to the value of 0.9207 derived from equation (3.10) shows a difference of only 0.14%.

3.5 Rayleigh-Lamb Frequency Equation for One Dimension

The theory for the propagation of waves in an infinite plate was published independently by Rayleigh[22] and Lamb[23]. These waves occur between the two free boundary defining the plate and are known as Lamb waves. Lamb identified two types of wave each having two perpendicular displacements. In both types of waves, the displacements occur both in the direction of propagation but in type designated as symmetrical, the displacement is symmetrical about a centre plane and in the antisymmetrical type, the displacement is the same throughout the plate and is flexural in nature. Fig. 3.8 shows the relative types of motion in plate. The eigenvalues of the plate waves for the symmetrical case is shown in equation (3.14).

$$\frac{\tanh\left(\frac{\pi h}{\lambda}\sqrt{(1-\frac{c_\phi^2}{c_s^2})}\right)}{\tanh\left(\frac{\pi h}{\lambda}\sqrt{(1-\frac{c_\phi^2}{c_B^2})}\right)} = 4\frac{\sqrt{(1-\frac{c_\phi^2}{c_B^2})(1-\frac{c_\phi^2}{c_s^2})}}{(2-\frac{c_\phi^2}{c_s^2})^2} \qquad (3.14)$$

where h is the plate thickness

$$c_B > c_s > c_\phi$$

This is sometimes known as Rayleigh-Lamb frequency equation.

For the type of wave considered in this work, the displacement is predominantly in the direction of wave propagation and in the plane of the plate (see Fig. 3.8a). There is a slight symmetrical motion with respect to the thickness direction. This is due to Poisson's ratio and is

covered by the use of the plate velocity. Equation (3.14) can be adapted for the case here. In the limit, the one dimensional Rayleigh frequency equation should be recovered from equation (3.14).

The wave equations, given in equation (3.7) are applicable as they stand for the theory of the plates. The solutions to equation (3.7) for a symmetrical wave propagated in x direction with the displacements dominant in the x, z direction are given as:

$$\phi = C \cosh \frac{2\pi z}{\lambda} \sqrt{1- \frac{c_\phi^2}{c_p^2}} \exp(j\omega t - \frac{2\pi x}{\lambda})$$

$$\psi = D \sinh \frac{2\pi z}{\lambda} \sqrt{1- \frac{c_\phi^2}{c_s^2}} \exp(j\omega t - \frac{2\pi x}{\lambda})$$

(3.15)

For a strip, the boundary conditions to be satisfied are that both plane and shear stresses at $z = \pm b$ must be zero. Substitution of equation (3.15) into equation (3.9) gives the following frequency equation.

$$\frac{\tanh \left(\frac{\pi b}{\lambda} \sqrt{(1- \frac{c_\phi^2}{c_s^2})}\right)}{\tanh \left(\frac{\pi b}{\lambda} \sqrt{(1- \frac{c_\phi^2}{c_p^2})}\right)} = 4 \frac{\sqrt{(1- \frac{c_\phi^2}{c_p^2})(1- \frac{c_\phi^2}{c_s^2})}}{(2- \frac{c_\phi^2}{c_s^2})^2}$$

(3.16)

where $C_p > C_s > C_\phi$

This is the Lamb wave equation applicable to the case considered. It will be noted that here the plate velocity C_p occurs where in the plate wave case, the bulk velocity C_B

must be used. The thickness h term in equation (3.14) is replaced by the width term b. Equation (3.16) have an infinite number of waves, each propagating at a velocity dictated by its frequency, width, density and elasticity.

For long wavelength ($\lambda \gg b$), the argument may be substituted for their hyperbolic tangent. Equation (3.16) reduces to

$$\left(\frac{C_\phi}{C_s}\right)^2 = 2(1+\sigma) \tag{3.17}$$

and $C_\phi = C_o$ (bar velocity)

For the limit for short wave ($b \gg \lambda$), their hyperbolic tangent term becomes unity. Equation (3.16) becomes

$$\left(2 - \frac{C_\phi^2}{C_s^2}\right)^2 = 4\left(1 - \frac{C_\phi^2}{C_p^2}\right)^{\frac{1}{2}} \left(1 - \frac{C_\phi^2}{C_s^2}\right)^{\frac{1}{2}}$$

This is the equation for one dimensional Rayleigh surface wave propagating on the edge of an infinite strip as given in equation (3.10).
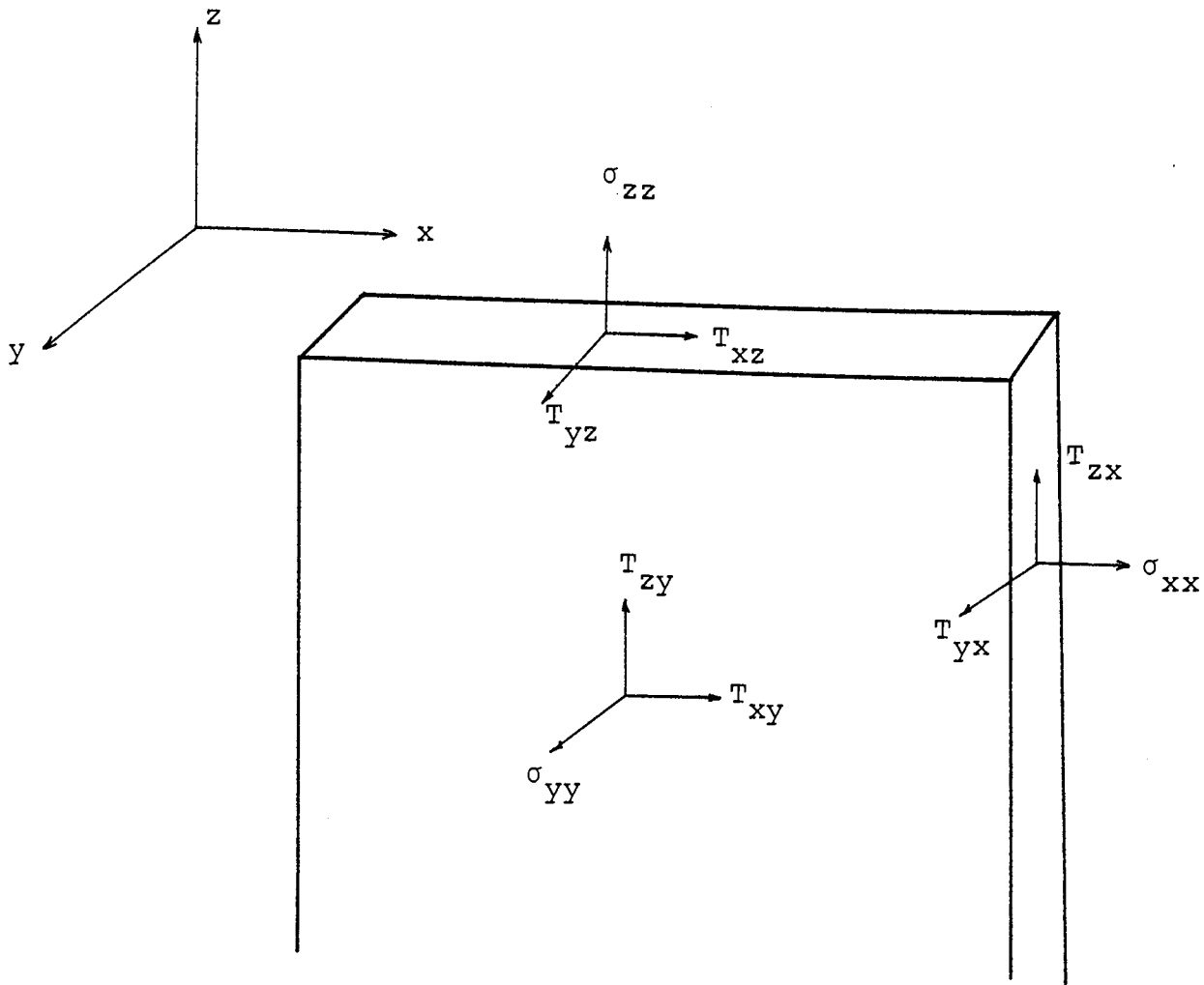
Figure 3.1   Stress components acting on a strip.

The displacement (u) may be resolved parallel to the x, y, z axes into components u_x, u_y, u_z. This gives six strain components as

$$e_{xx} = \frac{\partial u_x}{\partial x} \qquad e_{yy} = \frac{\partial u_y}{\partial y} \qquad e_{zz} = \frac{\partial u_z}{\partial z}$$

$$e_{yz} = \frac{\partial u_z}{\partial y} + \frac{\partial u_y}{\partial z} \qquad e_{zx} = \frac{\partial u_x}{\partial z} + \frac{\partial u_z}{\partial x} \qquad e_{xy} = \frac{\partial u_y}{\partial x} + \frac{\partial u_x}{\partial y}$$

For the case considered these simplify to the terms shown in equation (3.4).
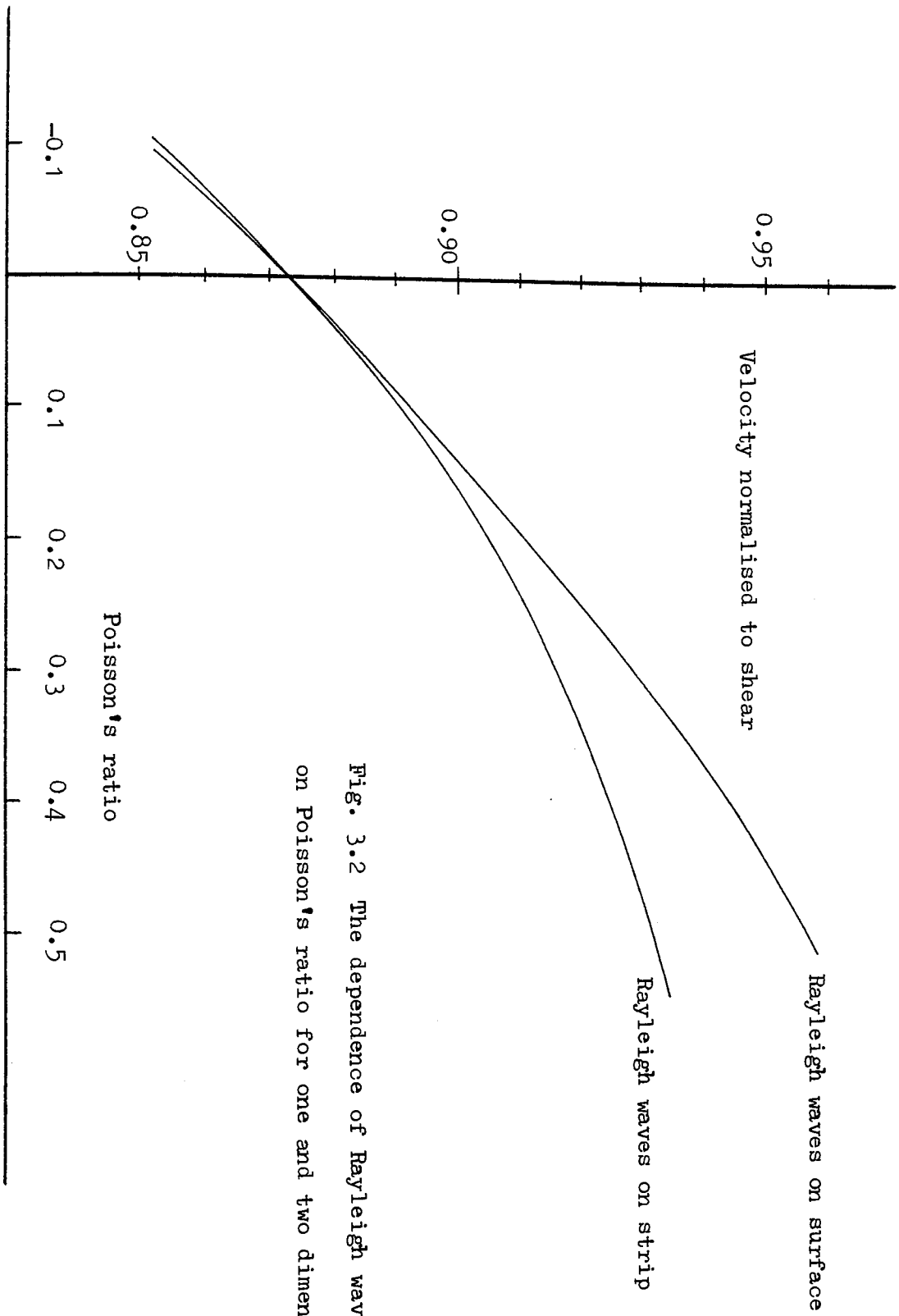
Fig. 3.2 The dependence of Rayleigh waves velocity
on Poisson's ratio for one and two dimensions.
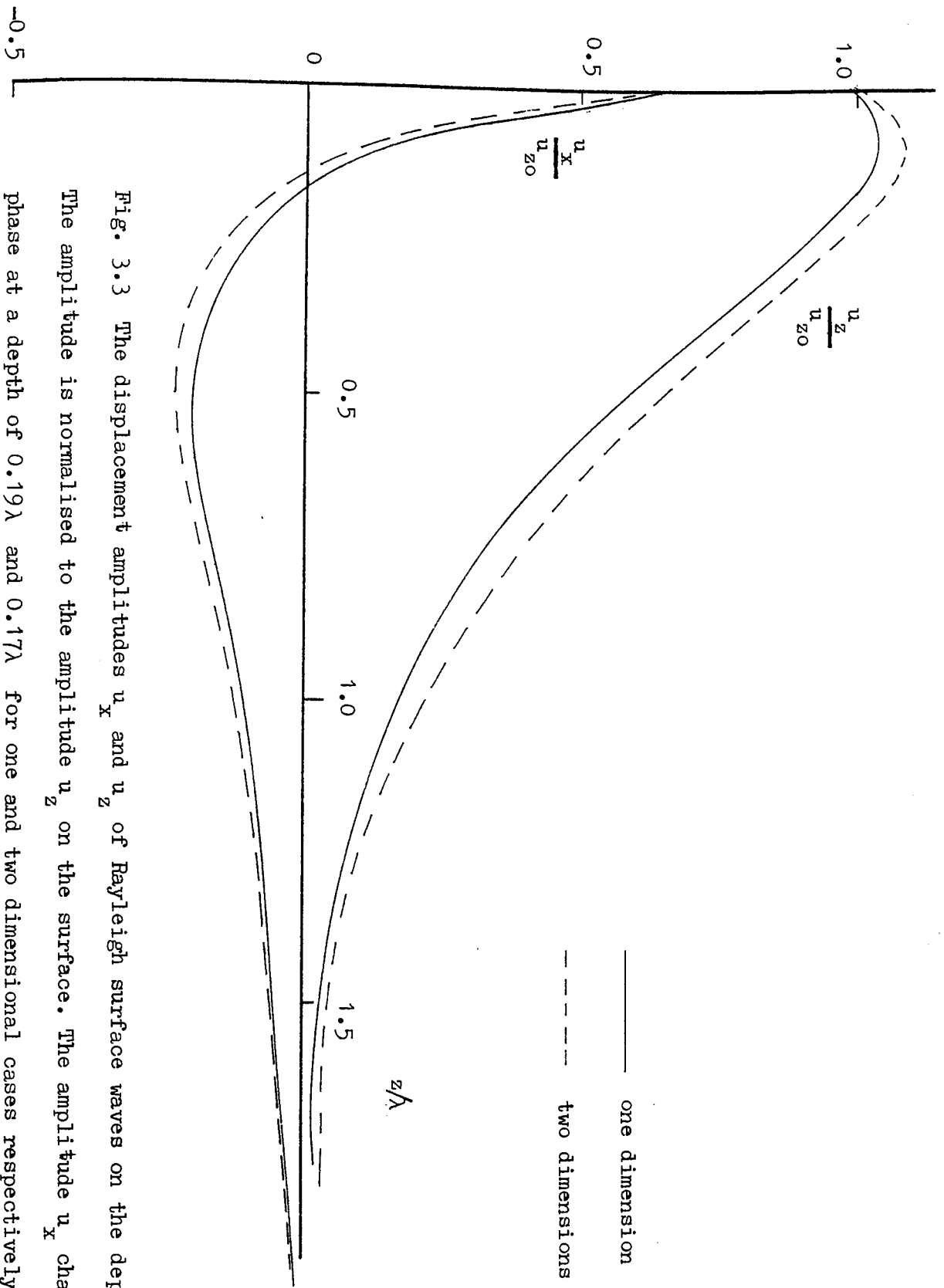
Fig. 3.3 The displacement amplitudes u_x and u_z of Rayleigh surface waves on the depth z. The amplitude is normalised to the amplitude u_z on the surface. The amplitude u_x changes phase at a depth of 0.19λ and 0.17λ for one and two dimensional cases respectively.
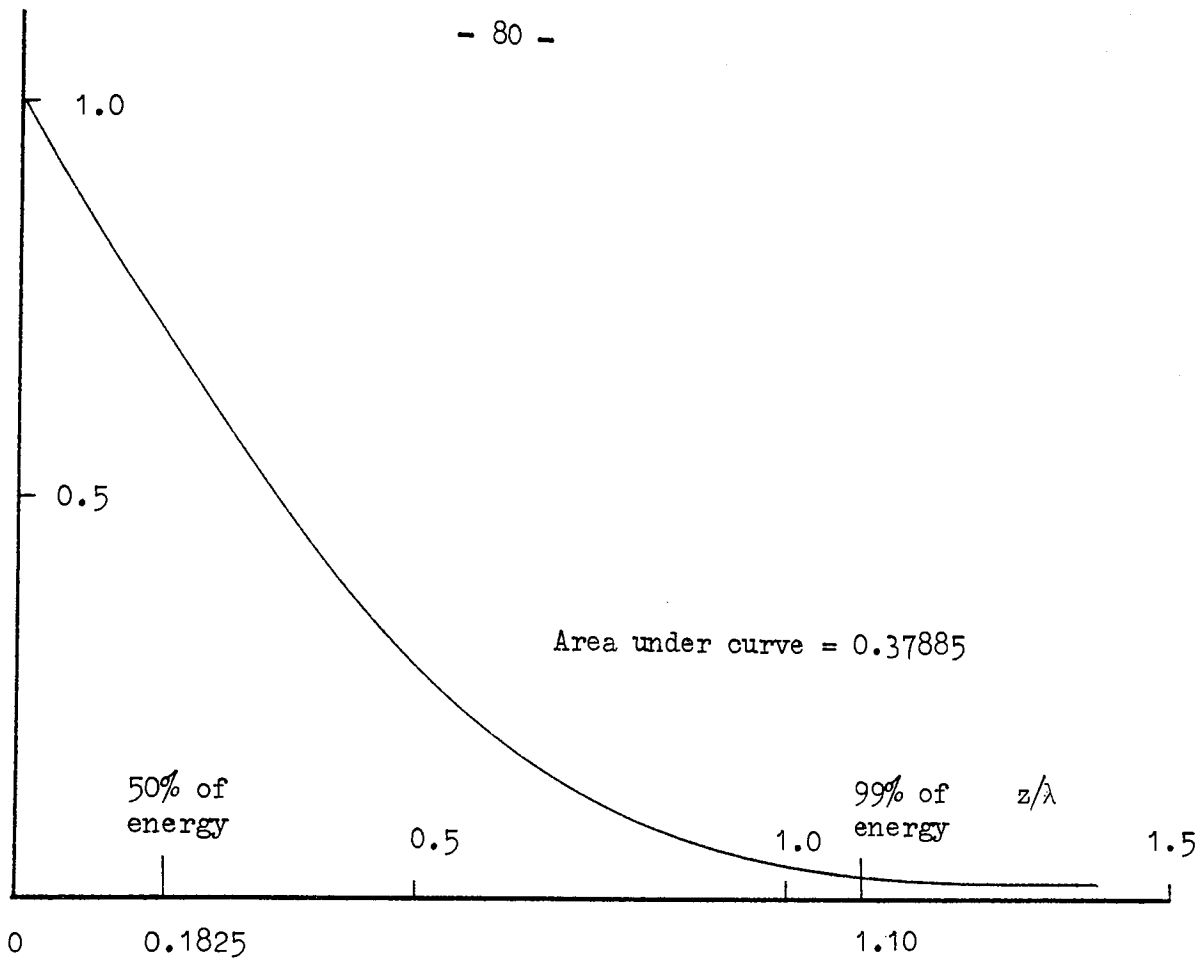
Fig. 3.4a The energy distribution of one dimensional surface waves ($\sigma = 0.34$) along the penetration depth. The energy is normalised to that on surface ($z = 0$).
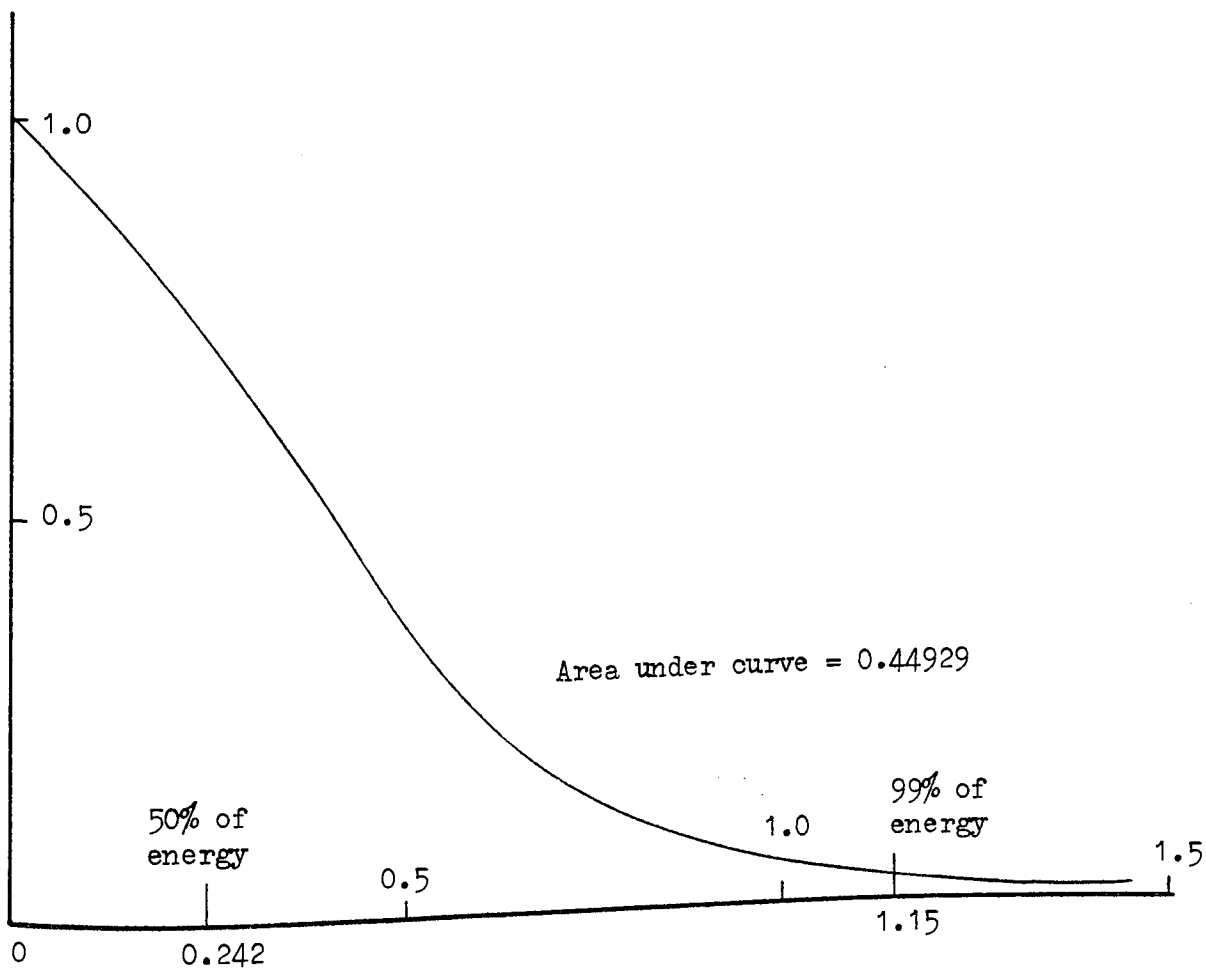
Fig. 3.4b As in fig. 3.4a, here shows the case of two dimensional
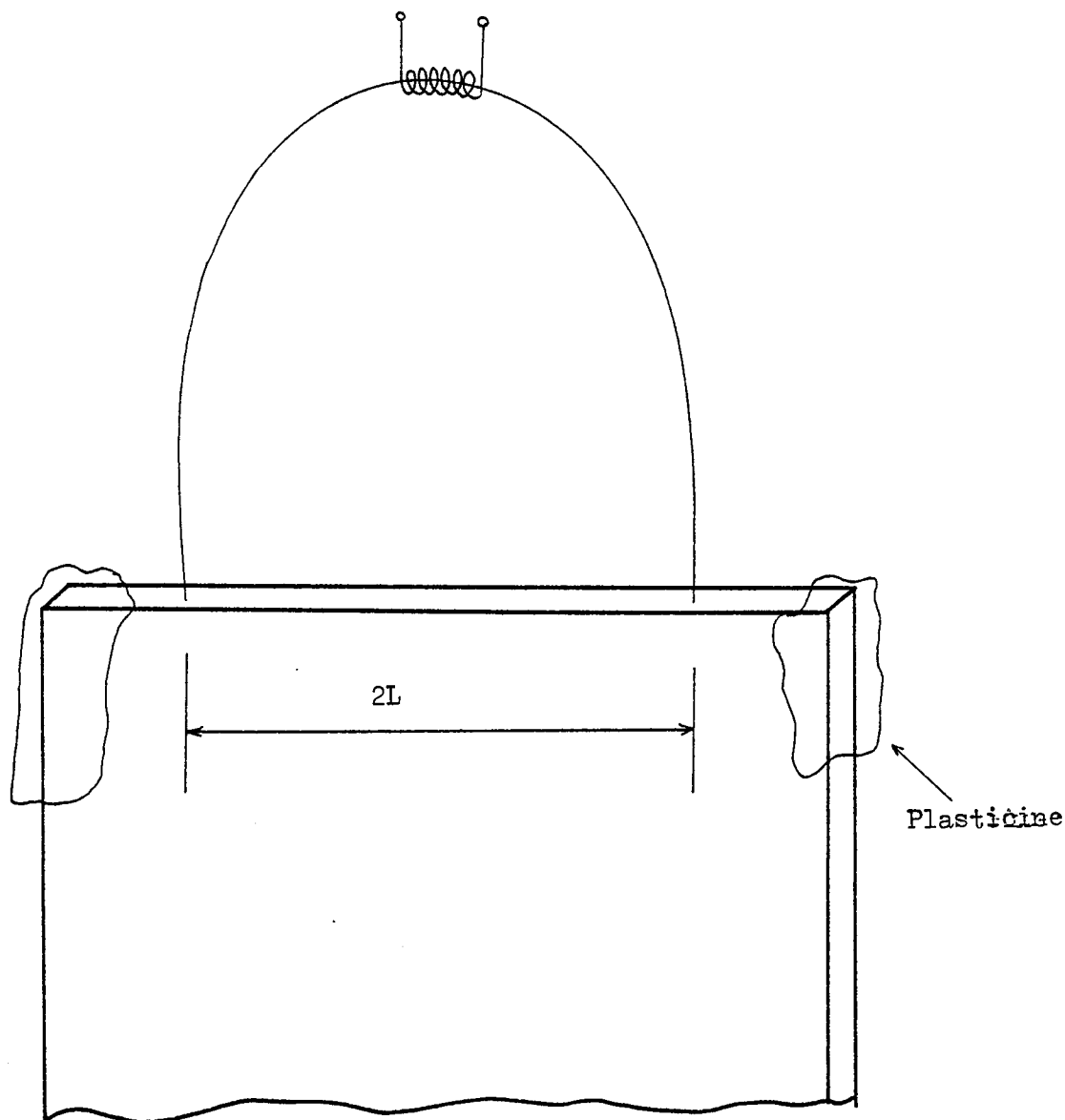
Fig. 3.5 The arrangement of double wire drive.

The transducer sends equal signals in both directions and the

two signals always have the same travel time. This technique enables

the Rayleigh waves velocity on straight edge to be obtained.

The plasticine is used to damp any small reflection arising

from the edges.
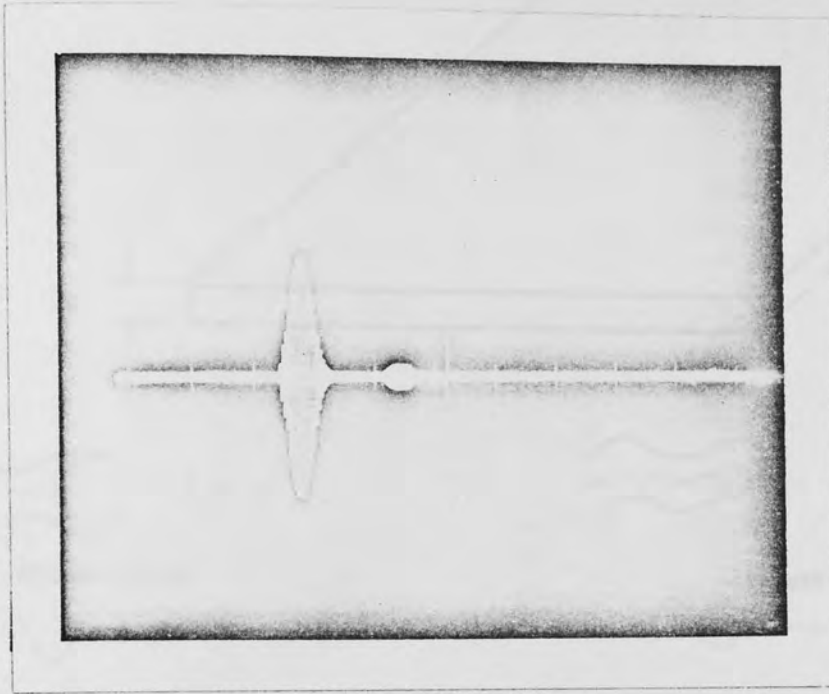
Fig. 3.6 A 10 oscillations burst at a frequency 348.678 kHz is traversed the edge of an aluminium strip 342.90 mm long. The first echo is the mismatched reflection arising from the drive points. The delay between two echoes is the time taken to travel between the drive points.
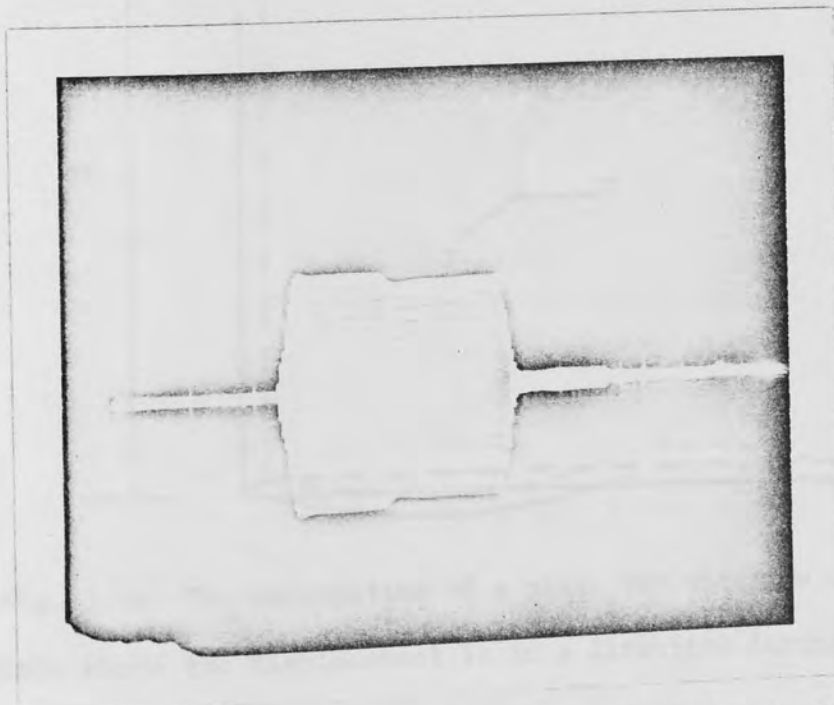
Fig. 3.7 As in fig. 3.6, in using a long burst, the overlapping of first and second echo gives minima and maxima and enables the phase velocity to be determined accurately.

2h

h = 0

Symmetrical

Asymmetrical

z

x

y
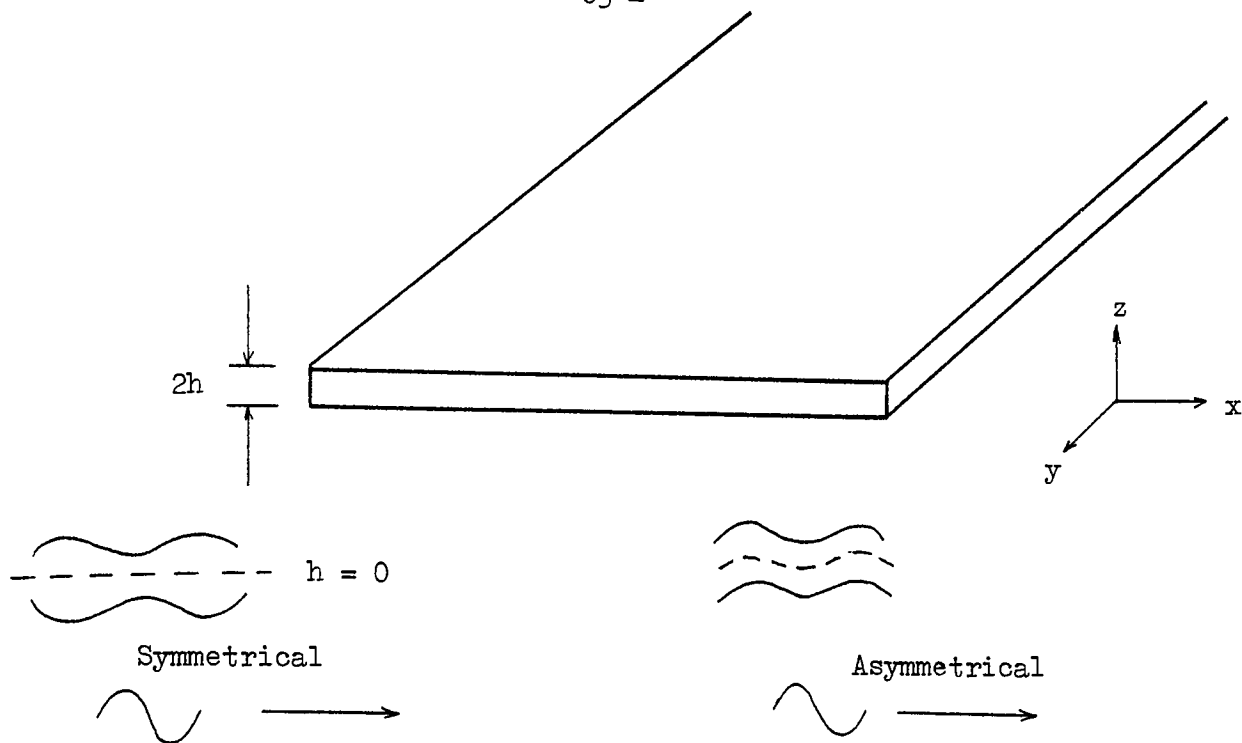
Fig. 3.8 The wave motion of Lamb waves on a plate.

2b

z

x

y
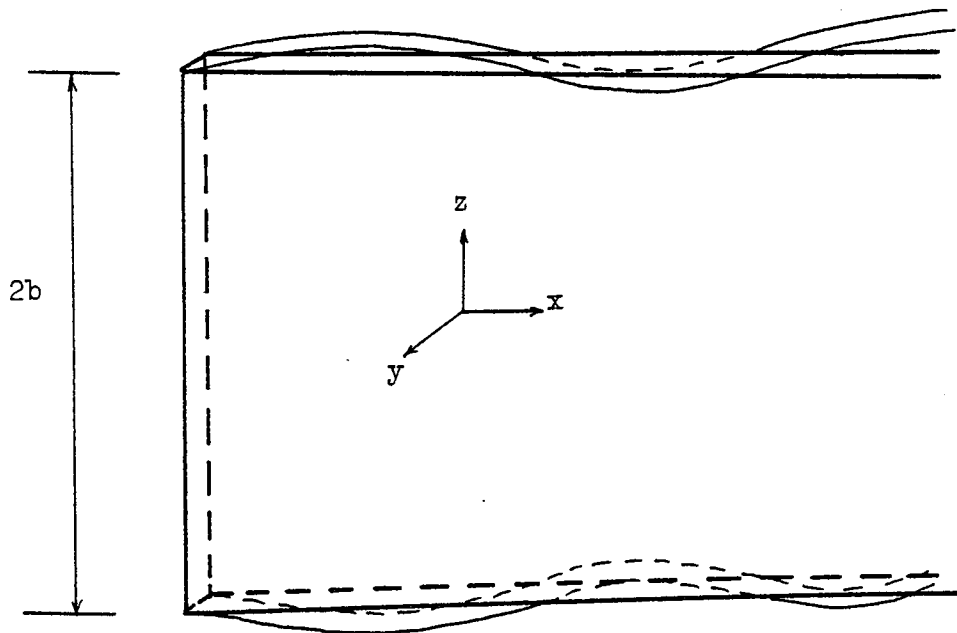
Fig. 3.8a The deformation of a plate for the case considered

here where the displacement is in z direction during propagation.

TWO DIMENSION		ONE DIMENSION

Wave Equations

$$\nabla^2 \phi = \frac{1}{C_B^2} \frac{\partial^2 \phi}{\partial t^2} \qquad\qquad \nabla^2 \phi = \frac{1}{C_P^2} \frac{\partial^2 \phi}{\partial t^2}$$

$$\nabla^2 \psi = \frac{1}{C_S^2} \frac{\partial^2 \psi}{\partial t^2} \qquad\qquad \nabla^2 \psi = \frac{1}{C_S^2} \frac{\partial^2 \psi}{\partial t^2}$$

Depth Function $\exp(-gz)$

$$g = \left(\frac{2\pi}{\lambda}\right)^2 - \left(\frac{2\pi f}{C_B}\right)^2 \qquad\qquad g = \left(\frac{2\pi}{\lambda}\right)^2 - \left(\frac{2\pi f}{C_P}\right)^2$$

Frequency Equation

$$R_0 = \text{Rayleigh Velocity/Shear Velocity}$$

$$\left(2 - R_0^2\right)^2 = 4\left(1 - R_0^2/H^2\right)^{\frac{1}{2}}\left(1 - R_0^2\right)^{\frac{1}{2}}$$

$$H = C_S/C_B \qquad\qquad\qquad\qquad H = C_S/C_P$$

Amplitude Ratio $(u_z/u_x)_{z=0}$

1.4679	$\sigma = 0.25$	1.4184
1.5741	$\sigma = 0.34$	1.4717

Table 3.1 General comparison of surface waves.

The major difference is the use of C_B and C_P in the case of two and one dimension respectively. Consequently, this gives a slower velocity and smaller amplitude ratio $(u_z/u_x)_{z=0}$. For $\sigma = 0$, however they are equal.

n	Frequency (kHz)	C_ϕ (m/sec.)	$C_g = 2L\dfrac{f_{n1} - f_{n2}}{n_1 - n_2}$ (m/sec.)
27	223.733	2842	
28	232.310	2845	
29	240.572	2845	
30	248.901	2845	
			2840
42	348.678	2847	
43	356.533	2843	
44	364.781	2843	
			2849
50	414.568	2843	
51	423.011	2844	
52	431.187	2843	
			2850
60	498.140	2847	
61	506.138	2845	
62	514.616	2846	

$$C_\phi \text{ (mean)} = 2844.5 \text{ m/sec.} \pm 0.057\%$$

$$C_g \text{ (mean)} = 2846.3 \text{ m/sec.} \pm 0.19\%$$

Table 3.2 shows velocities obtained experimentally on an aluminium strip ($2L = 342.90$ mm), $C_P = 5418$ m/sec. , $C_S = 3094$ m/sec. , $\sigma = 0.347$. The values of C_g are sufficiently close to C_ϕ to confirm the equality, bearing in mind the errors associated with the frequency differences of two large numbers.

CHAPTER 4

ONE DIMENSIONAL RAYLEIGH WAVES ON CURVED BOUNDARIES

CHAPTER 4

ONE DIMENSIONAL RAYLEIGH WAVES ON CURVED BOUNDARIES

4.1 Introduction

In a two dimensional surface wave, the wavefront must be
long in comparison with the wavelength. In one dimension, the
reverse is necessary and this condition is fulfilled by
propagation along the edge of a thin sheet. The two
dimensional wave on a curved surface can be analysed by
considering the surface of an infinite cylinder. Here the
wavefront is parallel to the axis and travels round the cylinder.
This approach was used by Viktorov[24], the analysis of the
Pochhammer-Chree wave equation established the dispensive
nature of such waves. The velocity approached the flat surface
non-dispersive Rayleigh wave velocity as the wavelength to
radius ratio approaches zero.

In this work, three edge types have been studied, the disk
with positive curvature, a circular hole with negative curvature
and for the curvature to be parallel to the wavefront, the
end of a cylindrical shell. Fig. 4.1 shows the photograph of
the specimens used in the experiments. In all cases, the
thickness of the sheet must be small compared to the wavelength.
No analysis appears to have been carried out hitherto, although
solutions are readily obtainable from the general solution
presented by Love[12]. The ability to generate these waves
has motivated this study.

The theoretical results can be obtained, in principle, either by taking the equation of the in-plane vibration of thin plates of relevant geometry or less rigorously by considering the edge itself and assuming the existence of a surface wave. Here the former more rigorous method was available for the disk and hole but only the latter method could be used for the cylindrical shell. The solution must give the straight edge velocity (R_o) as the wavelength approaches zero. For a wave travelling round the periphery of a disk, $\lambda = \pi d/n$ where n is the number of nodal diameters. Thus from a knowledge of n and the disk resonance f_n, the phase velocity can be obtained as $C_\phi = f_n \lambda_n$. Unlike the straight edge, in all these cases where there is curvature, the wave is dispersive. The group velocity can be obtained directly from the successive values of resonances. For a disk and a hole, the first root of the high order 'n' frequency equation represents the surface wave and explicit solutions can be obtained for all values of n. An algebraic expression is derived to show how the wave velocity approaches its asymptotic Rayleigh value.

Using the wire drive technique, extensive experiments were carried out on edges of positive and negative curvatures, the end of a cylindrical shell and combinations of curved and straight edges. This technique has also been used to generate waves round the surface of a sphere (the case for two dimensional curvature). Experimental results show a good agreement to the theory developed.

4.2 The Circular Disk

The in-plane frequency equation of a thin isotropic disk was derived by Love but the eigenvalues were not calculated until comparatively recently. Onoe[9] and Holland[10] gave the eigenvalues of the lower order modes up to 10 for selected values of Poisson's Ratio. The results were made the basis for the precise measurement of the elastic constants of isotropic and orthotropic materials by Bell, Sharp[2] and the author[7]. Equation (4.1) gives the frequency equation normalised to the shear velocity C_s where Ω_1 (the first root for a given n value) $= \pi f d/C_s$, the wavelength is equal to $\pi d/n$; thus Ω_1/n is the ratio of phase to shear velocity.

$$\begin{bmatrix} a_{11} & a_{12} \\ a_{21} & a_{22} \end{bmatrix} = 0 \tag{4.1}$$

where

$$a_{11} = -J_n\left(\frac{\Omega_1}{\theta}\right)\left[\frac{\Omega_1^2}{2} - n(n+1) + M_n\left(\frac{\Omega_1}{\theta}\right)\right]$$

$$a_{12} = nJ_n(\Omega_1)\left[M_n(\Omega_1) - (n+1)\right]$$

$$a_{21} = -nJ_n(\Omega_1)\left[M_n\left(\frac{\Omega_1}{\theta}\right) - (n+1)\right]$$

$$a_{22} = J_n(\Omega_1)\left[\frac{\Omega_1^2}{2} - n(n+1) + M_n(\Omega_1)\right]$$

(25)

$M_n(x)$ is sometimes known as Onoe's Modified Bessel quotient and is equal to $xJ_{n-1}(x)/J_n(x)$ and $\theta^2 = 2/(1-\sigma)$.

The equation has an infinite number of roots which correspond to the infinite modes of vibration. These are characterised by two integers m, the number of nodal circles, and n (the order of Bessel function in equation (4.1)), the number of nodal diameters. In the present case, the solution for nodal diameters only is considered so that m is always unity representing a central nodal point. This means obtaining the lowest argument solution for each successive order n of the Bessel functions in equation (4.1).

To study comprehensively the dispersive characteristic of the edged surface wave, Ω_1 values for high order n over a wide range of Poisson's ratio must be evaluated. The phase and group velocities are obtained from equation (4.2) and (4.2a).

$$C_\phi = \frac{\Omega_1}{n} C_s \qquad\qquad (4.2)$$

$$C_g = \frac{d\Omega_1}{dn} C_s \qquad\qquad (4.2a)$$

The computation is carried out, using Newton-Raphson method as

$$\Omega_{i+1} = \Omega_i - \frac{F(\Omega_i)}{F'(\Omega_i)} \qquad\qquad (4.3)$$

The only difficulty in using this method is in obtaining the derivative of the complicated frequency equation. However $F'(\Omega_i)$ can be represented by

$$F'(\Omega_i) = \frac{F(\Omega_i) - F(\Omega_{i-1})}{\Omega_i - \Omega_{i-1}} \qquad\qquad (4.4)$$

provided that $\Omega_i - \Omega_{i-1}$ is small and hence equation (4.3) becomes

$$\Omega_{i+1} = \frac{F(\Omega_i)\Omega_{i-1} - F(\Omega_{i-1})\Omega_i}{F(\Omega_i) - F(\Omega_{i-1})} \qquad (4.5)$$

The readily available values of $J_0(x)$ and $J_1(x)$ are obtained from library sources or the expression of polynominal approximation[26]. Then using the recursion relationship,

$$J_{n+2}(x) = \frac{2n}{x} J_{n+1}(x) - J_n(x) \qquad (4.6)$$

with equation (4.5) makes the computation of lower order modes easy. Examination of these low order modes showed that the phase velocity rapidly falls below the shear velocity ($\Omega_1 < n$), thus making the argument of the functions less than the order. Equation (4.7) then becomes available for evaluation and avoids without the problem of accumulated error. The precise value of $J_n(x)$ is represented by the series shown in equation (4.7). The series converges rapidly when $x \ll n$.

$$J_n(x) = \sum_{p=0}^{\infty} \frac{(-1)^P (x/2)^{n+2P}}{P! \, (n+P)!} \qquad (4.7)$$

Using equations (4.5), (4.6) and (4.7), the precise eigenvalues of equation (4.1) up to circumferential order n of 100 were evaluated. Beyond this value, the normal algorithm saturates the computer. The Debye's[27] expansion used below avoids this and values to $n = \infty$ are obtainable.

$$J_n(nx) = \frac{\exp[n(\mu_0 - \alpha_0)]}{(2\pi n \mu_0)^{\frac{1}{2}}} \left[1 + \frac{1}{n}(\frac{1}{8\mu_0} - \frac{5}{24\mu_0^3}) + \ldots \right] \qquad (4.8)$$

where

$$\alpha_o = \log_e \left(\frac{1+\mu_o}{x} \right)$$

$$\mu_o^2 = 1 - x^2$$

The eigenvalues for $n \geqslant 100$ are conveniently determined by re-writing equation (4.1) in the form:

$$\left[\frac{\Omega_1^2}{2n^2} - 1 - \frac{1}{n} + \frac{M_n(\Omega_1/\beta)}{n^2} \right] \times \left[\frac{\Omega_1^2}{2n^2} - 1 - \frac{1}{n} + \frac{M_n(\Omega_1)}{n^2} \right]$$

$$= \left[\frac{M_n(\Omega_1/\beta)}{n} - \frac{1}{n} - 1 \right] \times \left[\frac{M_n(\Omega_1)}{n} - 1 - \frac{1}{n} \right] \qquad (4.9)$$

For large order n, $M_n(\Omega_1)/n$ can be expressed as

$$\frac{M_n(\Omega_1)}{n} \simeq (1+\mu_o) \exp(-\mu_o) \exp\left[-n(\mu_o - \mu_1 - \alpha_o + \alpha_1) \right] \qquad (4.10)$$

where

$$\mu_o = (1-R_1^2)^{\frac{1}{2}}$$

$$\mu_1 = \frac{(n^2\mu_o^2 - 2n + 1)^{\frac{1}{2}}}{n-1}$$

$$\alpha_o = \log_e \left(\frac{1+\mu_o}{R_1} \right)$$

$$\alpha_o = \log_e \left[\frac{n-1}{nR_1} + \frac{(n^2\mu_o^2 - 2n + 1)^{\frac{1}{2}}}{nR_1} \right]$$

$R_1 = \Omega_1/n$ = ratio of Rayleigh phase velocity to the shear for the case considered. (R_o is used for the straight edge asymptote).

By using the established theorem concerning limit,

$$\lim_{x \to \infty} f(x) \times g(x) = \lim_{x \to \infty} f(x) \times \lim_{x \to \infty} g(x) \qquad (4.11)$$

$$\lim_{x \to \infty} f(x) = \lim_{t \to 0} f(t) \quad \text{where } t = \frac{1}{x} \qquad (4.11a)$$

Equation (4.10) can be expressed as

$$\frac{M_n(\Omega_1)}{n} = (1+\mu_o)\left[1 + \frac{\delta_1}{n} + \frac{\delta_2}{n} + \ldots\ldots\right] \qquad (4.12)$$

where

$$\delta_1 = \mu_o - \frac{1}{2\mu_o}$$

$$\delta_2 = \mu_o - \frac{1}{2\mu_o} - \frac{1}{6\mu_o^3}$$

and again $n > \Omega_1$.

A derivation of equation (4.12) is given in Appendix (2). This gives equation (4.13) which has been put in the form of equation (4.9) with the addition of dispersive terms which are polynominals in $1/n$ and $1/n^2$.

$$\left[\frac{R_1^2}{2} - 1 + \frac{\mu_o}{n} + \frac{(1+\mu_o)\delta_1}{n^2}\right] \times \left[\frac{R_1^2}{2} - 1 + \frac{\gamma_o}{n} + \frac{(1+\gamma_o)\delta_3}{n^2}\right]$$

$$= \left[\mu_o + \frac{(\delta_1 + \mu_o \delta_1 - 1)}{n} + \frac{(\delta_2 + \mu_o \delta_2)}{n^2}\right] \times \left[\gamma_o + \frac{(\delta_3 + \gamma_o \delta_3 - 1)}{n} + \frac{(\delta_4 + \gamma_o \delta_4)}{n^2}\right]$$

$$(4.13)$$

where

$$\gamma_o = (1 - \frac{R_1^2}{a^2})^{\frac{1}{2}}$$

$$\delta_3 = \gamma_o - \frac{1}{2\gamma_o}$$

$$\delta_4 = \gamma_o - \frac{1}{2\gamma_o} - \frac{1}{6\gamma_o^3}$$

Using equations (4.5), (4.6), (4.7) and (4.13), the eigenvalues for selected orders of n were evaluated with a range of Poisson's ratio 0.0 to 0.5 in intervals of 0.1 as shown in Table 4.1. Inspection shows equation (4.13) to have the same form as equation (3.10) as the wavelength approaches zero. To investigate their dispersive characteristic, the phase and group velocities of the waves travelling round the edge of the disk were also calculated and included in Table 4.1. It is apparent that the phase velocity is higher than the corresponding group velocity and that for low order n, both velocities are greater than the shear velocity. This condition does not really represent the surface wave as the energy will no longer be confined to the edge. As the frequency is increased, both velocities become lower than that of shear wave. It has been shown that in Chapter 2, the equivalent mass of the in-plane disks will fall considerably as n increases. The theoretical and experimental result of a mild steel annular disk given in ref (4) confirms this, the in-plane resonant frequencies of modes $n \geqslant 8$ were unchanged and identical to the disk, the frequency does fall when inner radius is $\geqslant a/2$. This means that the energy becoming more

and more confined to the edge and approaching surface wave situation. For small curvature, equation (4.14) gives a second form showing how the normalised phase velocity approaches the straight edge Rayleigh wave velocity (R_0).

$$R_1 = R_0 (1 + \frac{b_1}{n} - \frac{b_2}{n^2} + \ldots.) \tag{4.14}$$

where

$$b_1 = 1.986$$
$$b_2 = 3.609$$

The variation of coefficients b with Poisson's ratio is very small as the velocity has already been normalised to the straight edge velocity (R_0). Differentiating equation (4.14) and substituting into equation (4.2a) gives the group velocity for small curvature.

$$\frac{C_g}{C_s} = R_0 (1 + \frac{b_2}{n^2} + \ldots.) \tag{4.15}$$

The positive term in $1/n^2$ of equation (4.15) means that while the group is less than the phase velocity, it is greater than the asymptotic value R_0. The group velocity converges more rapidly to the asymptotic straight edge value than that of phase velocity because its first polynominal term has the multiplier of $1/n^2$. This feature was used to determine its asymptotic value during the experiments.

4.3 The Circular Hole

This structure, which is the inverse of a circular disk, can be considered as a hole inside a sheet which is an isotropic homogeneous medium extending to infinity. The analysis is similar to that for a disk and the characteristic equation is similar to equation (4.1) with the Bessel function of first kind replaced by Hankel function having the same argument. The Hankel function $H_n(x)$ [28] represents the wave radiating energy away from the guiding concave edge. Equation (4.16) gives the characteristic equation for the wave propagating along the edge of a circular hole.

$$\left[\frac{\Omega^2}{2n^2} - 1 - \frac{1}{n} + \frac{N_n(\Omega)}{n^2}\right] \times \left[\frac{\Omega^2}{2n^2} - 1 - \frac{1}{n} + \frac{N_n(\Omega/\theta)}{n^2}\right]$$

$$= \left[\frac{N_n(\Omega)}{n} - 1 - \frac{1}{n}\right] \times \left[\frac{N_n(\Omega/\theta)}{n} - \frac{1}{n} - 1\right] \qquad (4.16)$$

where

$$N_n(x) = x \frac{H_{n-1}(x)}{H_n(x)}$$

and

$$H_n(x) = J_n(x) + iY_n(x)$$

The properties of Hankel function result in characteristic equation (4.16) will have no solution for any real values of n. The wavenumber n that corresponds to Rayleigh wave here is complex.

For large value of n and $1<x<0$, $J_n(nx)$ and $Y_n(nx)$ can be

represented as

$$J_n(nx) \simeq \frac{\exp\left[n(\mu_o - \alpha_o)\right]}{(2\pi n \mu_o)^{\frac{1}{2}}} \qquad (4.17)$$

$$Y_n(nx) \simeq \frac{\exp\left[n(\alpha_o - \mu_o)\right]}{(\frac{\pi}{2} n \mu_o)^{\frac{1}{2}}} \qquad (4.18)$$

It is apparent that $Y_n(nx)$ and $J_n(nx)$ are exponentially decaying and growing respectively and eventually $N_n(\Omega) = M_n(\Omega)$ as $1/n$ approaches zero. This shows the $J_n(\Omega)$ term will dominant the $H_n(\Omega)$ when n is large and suggests that the wave will only propagate when λ/d is small. Consequently, the wave will propagate with attenuation as the wave energy radiates inside the medium. The velocity again approaches the asymptotic value R_o at very high frequency.

4.4 The Cylindrical Shell

Consider the surface wave propagating along the edge of a cylindrical shell of means radius a, thickness h where there is no radial component. The vertical (u_z) and tangential (u_θ) displacements can be expressed as

$$u_z = \frac{\partial \phi}{\partial z} - \frac{1}{a} \frac{\partial \psi}{\partial \theta} \qquad (4.19)$$

$$u_\theta = \frac{1}{a} \frac{\partial \phi}{\partial \theta} + \frac{\partial \psi}{\partial z} \qquad (4.20)$$

The potential functions ϕ and ψ are postulated to be of the form for surface wave on a straight edge. Therefore,

$$\phi = \exp\left[-gz\right] \exp\left[i\left(\frac{2\pi a}{\lambda}\theta - \omega t\right)\right] \qquad (4.21)$$

$$\psi = \exp\left[-pz\right] \exp\left[i\left(\frac{2\pi a}{\lambda}\theta - \omega t\right)\right] \qquad (4.22)$$

For a stress free edge, the boundary conditions are the stress resultant σ_{zz} and stress couple $T_{z\theta}$ must vanish at z=0. They are given as [29]

$$\sigma_{zz} = \rho C_p^2 \left[\frac{\partial U_z}{\partial z} + \frac{\sigma}{a}\left(1 - \frac{h^2 \sigma_1^2}{a^2}\right) \frac{\partial U_\theta}{\partial \theta}\right] \qquad (4.23)$$

$$T_{z\theta} = \rho C_s^2 \left[\frac{\partial U_\theta}{\partial z}\left(1 + \frac{h^2}{4a^2}\right) + \frac{1}{a} \frac{\partial U_z}{\partial \theta}\right] \qquad (4.24)$$

where

$$\sigma_1^2 = \frac{2+\sigma}{24(1-\sigma)}$$

Inserting equations (4.21) and (4.22) into equations (4.23) and (4.24) gives the frequency equation. It takes the form of the determinant of equation (4.1), the terms become

$$a_{11} = g^2 - \sigma \left(\frac{2\pi}{\lambda}\right)^2 \left(1 - \frac{h^2 \sigma_1^2}{a^2}\right)$$

$$a_{12} = i \frac{2\pi}{\lambda} p \left[\sigma \left(1 - \frac{h^2 \sigma_1^2}{a^2}\right) - 1\right]$$

$$a_{21} = i \frac{2\pi}{\lambda} g \left[2 + \frac{h^2}{4a^2}\right]$$

$$a_{22} = \left(\frac{2\pi}{\lambda}\right)^2 + p^2 \left(1 + \frac{h^2}{4a^2}\right)$$

As in the case of a circular disk, this has been put in the form of equation (4.25) again with the addition of dispersive term (h/a).

$$\left[2 - R_s^2 + \frac{2\sigma}{1-\sigma}\left(\frac{h\sigma_1}{a}\right)^2\right] \times \left[2 - R_s^2 + (1 - R_s^2)\left(\frac{h}{2a}\right)^2\right]$$

$$= 4 \times (1 - R_s^2)^{\frac{1}{2}} \times \left(1 - \frac{R_s^2}{\beta^2}\right)^{\frac{1}{2}} \times \left[1 + \frac{1}{2}\left(\frac{h}{2a}\right)^2\right] \times \left[1 + \frac{\sigma}{1-\sigma}\left(\frac{h\sigma_1}{a}\right)^2\right]$$

$$(4.25)$$

where
R_s = velocity normalised to the shear velocity.

The dependent variable R_s of equation (4.25) is completely described by Table 4.2 over a reasonable wide range of the independent variable h/a and σ. In this case, it is noted that R_s has a slightly higher value than that of straight edge (R_0), while the deviation of the velocity ratio due to the h/a term is very small indeed and the charactersitic of this wave is essentially the same as the straight edge.

4.5 Experiments

Experiments were carried out on the three edges considered theoretically in earlier sections i.e. disks, holes and the ends of cylindrical shells. The technique was extended to the two dimensional dispersive case, the waves on the surface of a sphere.

The closed circuit is essential to the production of standing surface waves as the reflection method is ineffective. This is because of mode conversion, only a small fraction of the energy of a surface waves is reflected as a surface wave, the rest is converted to other wave propagating modes. In the analysis of surface wave production and detection, the loss of energy to other modes must always be considered. Edge curvature and frequency were found to have a conspicuous effect on the efficiency of the wire drive as a source of surface waves. Standing wave resonances can be determined by the normal technique of the pulse-echo system of observing a null or minimum of the echo. Successive resonances represent a unity increase of one wavelength in the circuit. A mathematical treatment on the stepped echo has been illustrated in Chapter 2; the plots from the mini-computer graphic unit show the characteristic of the stepped echo and null represents the resonance. This technique can give the group velocity directly by observing burst transit or phase velocity with high precision by resonances. Successive resonances can also be used to obtain the group velocity and this has been found to be the more accurate method.

The drive line diameter and the length of the line is chosen to minimize the line loss and give reasonable coupling when operating in high frequency region. Normally a 0.25~0.5mm diameter nickel wire is most suitable for all thin specimens. The line is stretched in ambient temperature in order to minimize the kinks and attentuation; the end of the line is annealled to give the maximum magnetostrictive effect. [30] Since the attentuation and scattering of surface waves depends considerably on the degree of surface finish, therefore the edges of various circular structures used in the experiments are polished and machined with strict uniformity in order to avoid the influence of those factors.

In using the wire drive technique which is applicable to any materials, the measurements were first made on an aluminium disk of 200 mm diameter, 1 mm thick and a glass disk of 117.50 mm diameter, 3.3 mm thick. A 0.5 mm line was used to excite the specimens and a good coupling was observed throughout the experiments. Some lossy material, for example plasticine, was covered round the centre region of the disk as the energy from the line radiates into the body of the plate as well as the surface wave. The plasticine removes the unwanted vibrations and interferences to the echo pattern. It has been shown in Chapter 2 that the equivalent mass of the disk will fall considerably as n increases, this means that the energy becomes more and more confined to the edge and approaches the surface wave situation. Tables 4.3 and 4.4 show the variation of measured phase velocity and velocity ratio from the aluminium and glass disks for n=2 to 100 and 2 to 50 respectively. This

also gives its corresponding Poisson's ratio. As the wave is dispersive, its group velocity is calculated by successive resonances from the expression $\pi d \frac{df}{dn}$. This dispersive effect can also demonstrate in the stepped echo pattern. In experiments, it is not possible to observe the progress of any individual wave in a group and hence the velocity directly measured from the oscilloscope trace will give only group velocity. Therefore, the number of oscillations per step resulting from the overlapping of echoes arises from the propagation at the group velocity. Because of this dispersion of velocity, the number of oscillations per step is not necessarily equal to the mode number n. Fig. (4.3) shows the stepped echo pattern of an aluminium disk from oscilloscope trace in which the number of oscillations per steps have a value of 6, and higher than the mode number (n=5). This illustrates the phase velocity of a disk travelling faster than its group velocity at a ratio about 6/5, this result is well within the limit of the experimental error. From the experimental results, the extrapolation of the group velocity to zero 1/n gives a valuable figure for the straight edge velocity R_O. Figs. (4.4) and (4.5) show the graphs for the phase velocity ratio of the disks against the mode number n. Figs. (4.4a) and (4.5a) shows the extrapolated curves of velocity ratios against the reciprocal of mode number i.e. 1/n. From the results, it concludes that the wave is dispersive with the condition $1 > R_1 > R_O$ for $n \geqslant 20$ and differences in phase and group velocity diminishes as 1/n approaching zero and are equal to the asymptotic velocity R_O which is governed by the equation (3.10). The asymptotic

velocities derived from the graphs correspond to the values calculated from the elasticity data.

Measurements were also carried out on a rectangular plate with two semi-circular ends. The dimension and measured result were shown in Figs. 4.6 and 4.6a respectively. A better coupling effect is obtained by driving at the curved edge and gives a better match. It is evident that the dispersion in this case is originating from the cruved boundary with $C_\phi > C_g$ and the extrapolated velocity ratio has the same consistency with the calculated value as the disk. To demonstrate the originality of the dispersion further, Fig. 4.7 shows the graph of velocity ratio against $\lambda/2\pi r$ where r is the radius of the semi-circular end and compares to the calculated velocity of the disk. A fair agreement is achieved but it clearly favours the high order values although the frequency is not high enough to make it more decisive.

The next investigation of in-plane surface waves was carried on the edge of a cylindrical shell. Good coupling was obtained with a 0.5mm nickel line on a cylindrical shell mean diameter 149mm, thickness 3mm, this enables an accurate velocity measurement for n=15 to 45. The result of phase velocity plotted against 1/n is shown in Figure 4.8. The features given in the theory that the asymptotic velocity is slightly higher than the straight edge value is apparent. The result shows a small dispersion which is not predicted within the theory, a more rigorous anlaysis would require

another postulated potential function and to satisfy the
wave equation of a thin shell rather than the two dimensional
elastic wave equation.

On a concave edge, Rayleigh waves are also dispersive,
the investigation would not have been complete without
demonstrating this experimentally. A circular hole of 308mm
diameter was cut inside a large aluminium sheet 1.6mm thick.
A 0.5mm line was used to launch the wave round the hole which
had been machined and polished to give maximum uniformity. No
echo was observed at low frequency region (f≤200 kHz). As
the frequency was increased, a weak echo appeared and
combined with the initial reflection from the drive point to
give maxima and minima from which the phase velocity could
be obtained in the normal way. The coupling is poor as
considerable energy radiates into the body of the plate. This
prevented the appearance of a phase null in the echo. Careful
measurements were made for n values of 80 to 200. The
average group velocity was evaluated from the expression
$C_g = \pi d \frac{df}{dn}$ with groups of six adjacent phase velocity values.
The result is shown in Table 4.5. The experimental results
show $C_g > C_\phi$ and $1 > R_0 > R_c$ where R_c is the normalised ratio of
phase velocity of a hole to the shear velocity. This is an
inverse result to the circular disk.

To confirm the result further, a curve fitting program
is used to obtain the algebraic expression of phase velocity
from its experimental values. This gives equation (4.26).

$$R_c = R_0 \left(1 - \frac{C_1}{n} - \frac{C_2}{n^2} + \ldots\ldots\right) \qquad (4.26)$$

where $C_1 = 1.962$

$C_2 = 4.326$

The positive value of the coefficient term C_2 confirms the group velocity is higher than the asymptotic value R_0. In comparing the equations (4.14) and (4.26) and for large order n, it is noted that the first coefficient term is approximately equal and only differing in sign. This strongly suggests that equation (4.14), derived from the theory, is valid with n and -n for circular disk and hole respectively. In using equation (4.14) and (4.26), figure 4.9 shows the phase and group velocities against the value of ±1/n. The velocities were normalised to R_0 in which +1/n represents the region of a circular disk, -1/n, the circular hole and zero 1/n, the straight edge. Fig. 4.11 shows the curve is continuous and smooth between the transition region of convex and concave edges.

It was considered that to complete the experimental studies, an attempt to launch surface waves on a sphere using the wire drive technique should be made. In this case, the surface wave is two dimensional. A billiard ball was selected as being of light material and readily machinable. The drive can be considered as occurring at the north pole with the wave fronts travelling round the sphere as lines of latitude returning to that region once per circuit. The

billiard ball diameter 48.5mm was driven by a 1mm line.
The velocity was measured for n=2 to 22 in interval of 1.
After the measurement, a thin circular disk was cut from the
billiard ball to enable values of shear velocity and
Poisson's ratio to be obtained. The result was plotted in
fig. 4.10. With no exception, the wave was dispersive with
$C_\phi > C_g$ and approaching to its asymptotic velocity as $1/n$
diminishes. A good agreement of the two dimensional asymptotic
velocity ratio between the values derived from the
extrapolated curve and the elasticity data is obtained. The
percentage difference is 0.54%. High precision will have
been obtained if higher order resonances had been measured
but this was limited by the internal friction of the material.
In Figs. 4.11(a) and 4.11(b), the oscillograms show the
single pulse and the corresponding echo pattern produced by
the overlapping of standing waves on the billiard ball. An
unexpected result was the very low velocity (1123m/sec) in the
material. This probably accounts for the fact that the click
of the billiard ball is audible. The extreme hardness of
the material adds to the paradox.

4.5 Conclusion

An exposition of the theory of the propagation of one dimensional surface waves on the edge of various circular structures as well as the experimental investigation, is given in this chapter.

Table 4.6 describes the essential features of one dimensional surface waves on circular disks, holes, cylindrical shells and the straight edge. Although the dispersive characteristic is a parallel to the two dimensional case and Rayleigh waves have received considerable attention in view of their usefulness but the applications are mainly two dimensional. The suggestions of neglecting these waves are

(1) The experimental problem involved with the efficient coupling to this mode on the edge of thin specimen. The wave velocity convergence is slow, a very accurate experimental technique is needed to determine its dispersion. However, the magnetostrictive line drive has been imporved by the author to operate up to 1 MHz. This enables the phase and group velocities to be determined with high precision.

(2) Because of the frequency limitation, the edged surface wave does not appear to be so relevant to the applications such as SAW filter, electro-mechanical delay line and surface flaw detection and have therefore been ignored. Probably the most important application that this investigation has shown

is that the edged surface wave provides a fast and simple
non-destructive testing method of any defects near the edge
of the disk. This application will be described in the
next chapter.
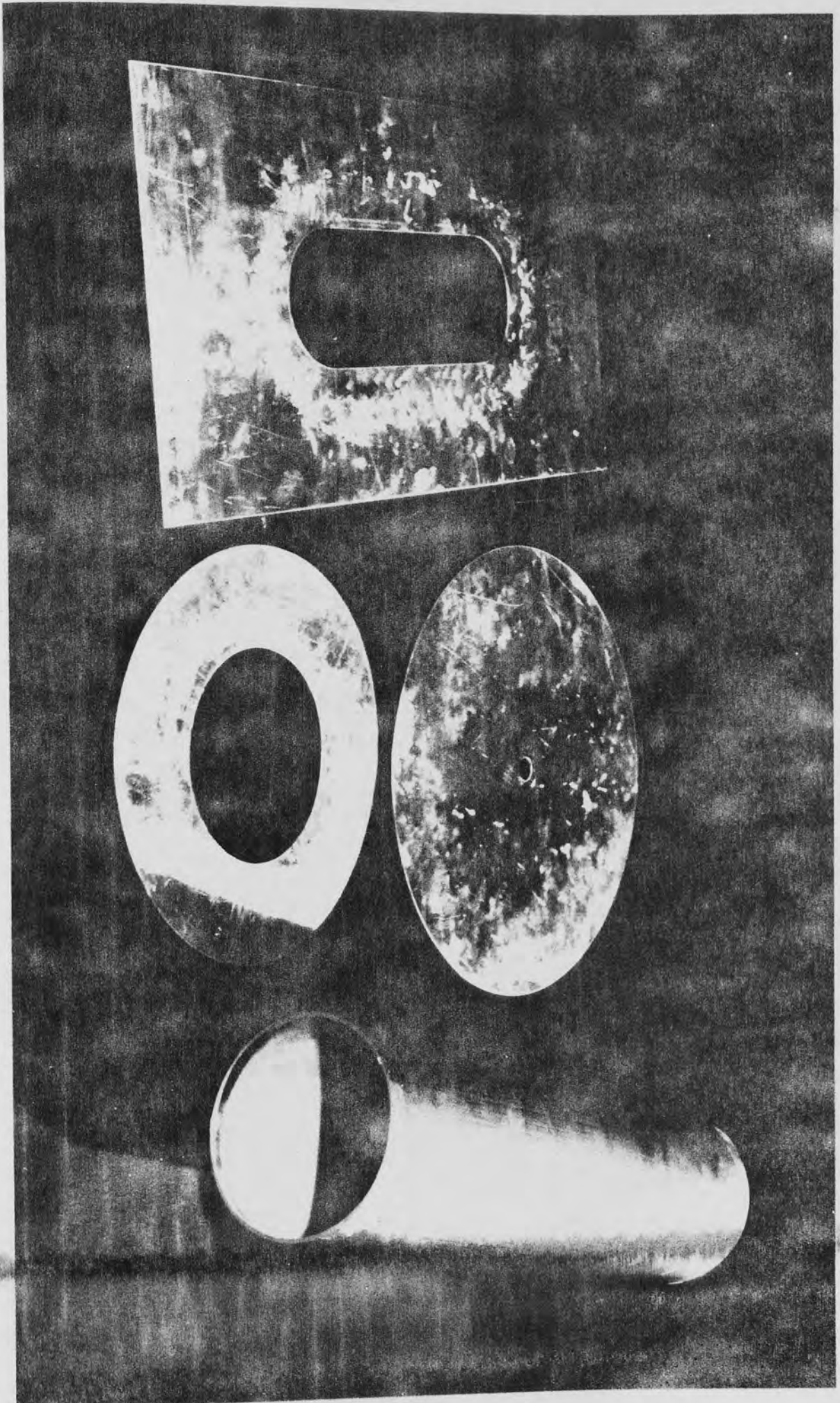
Figure 4.1 Photograph of the specimens used to investigate

the characteristics of Rayleigh wave velocity on curved

boundaries.
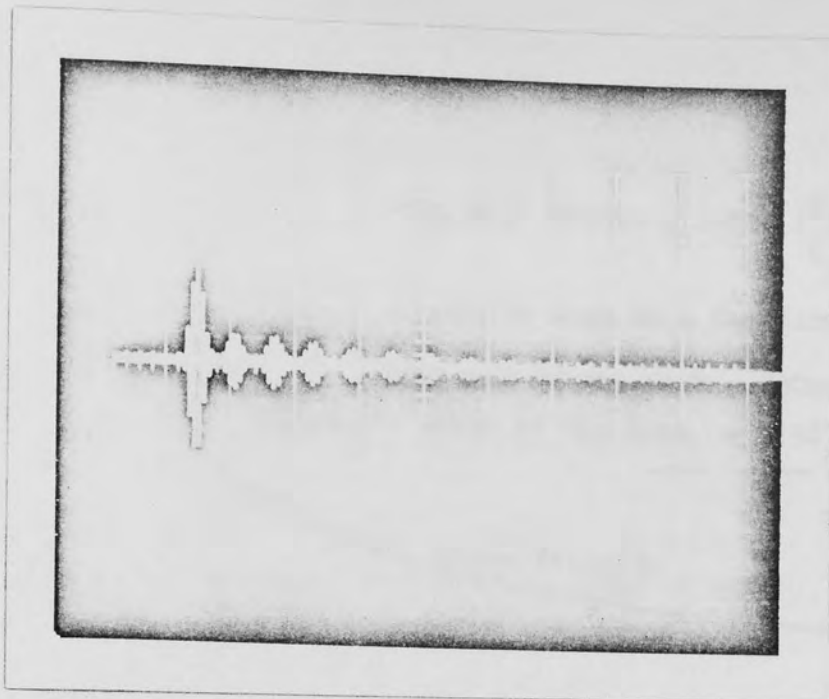
Figure 4.2 A short burst travelling round the aluminium disk.
This demonstrates the group velocity.
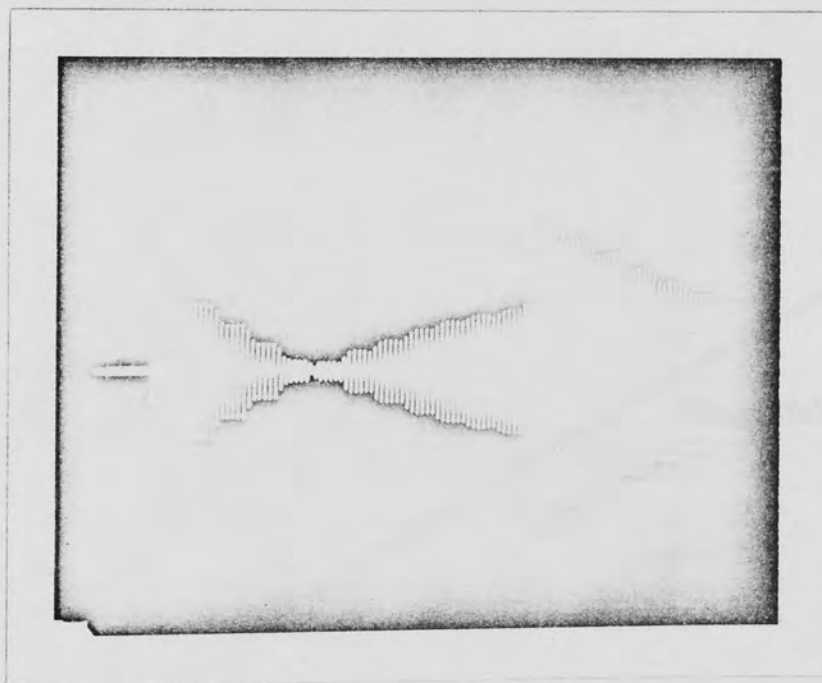
Figure 4.3 As in fig.4.2 , here shows the corresponding
stepped echo pattern (mode number = 5) produced by the
overlapping of long bursts with 6 oscillations per step.
This indicates $C_g < C_\phi$.

Fig. 4.4   Velocity ratio $(\frac{C_R}{C_S})$ for the aluminium dusk as a function of 'n'.

Diameter of the disk = 200mm , C_S = 3094 m/s
Poisson's ratio of the disk = 0.347
———— Theory
x   Experiment
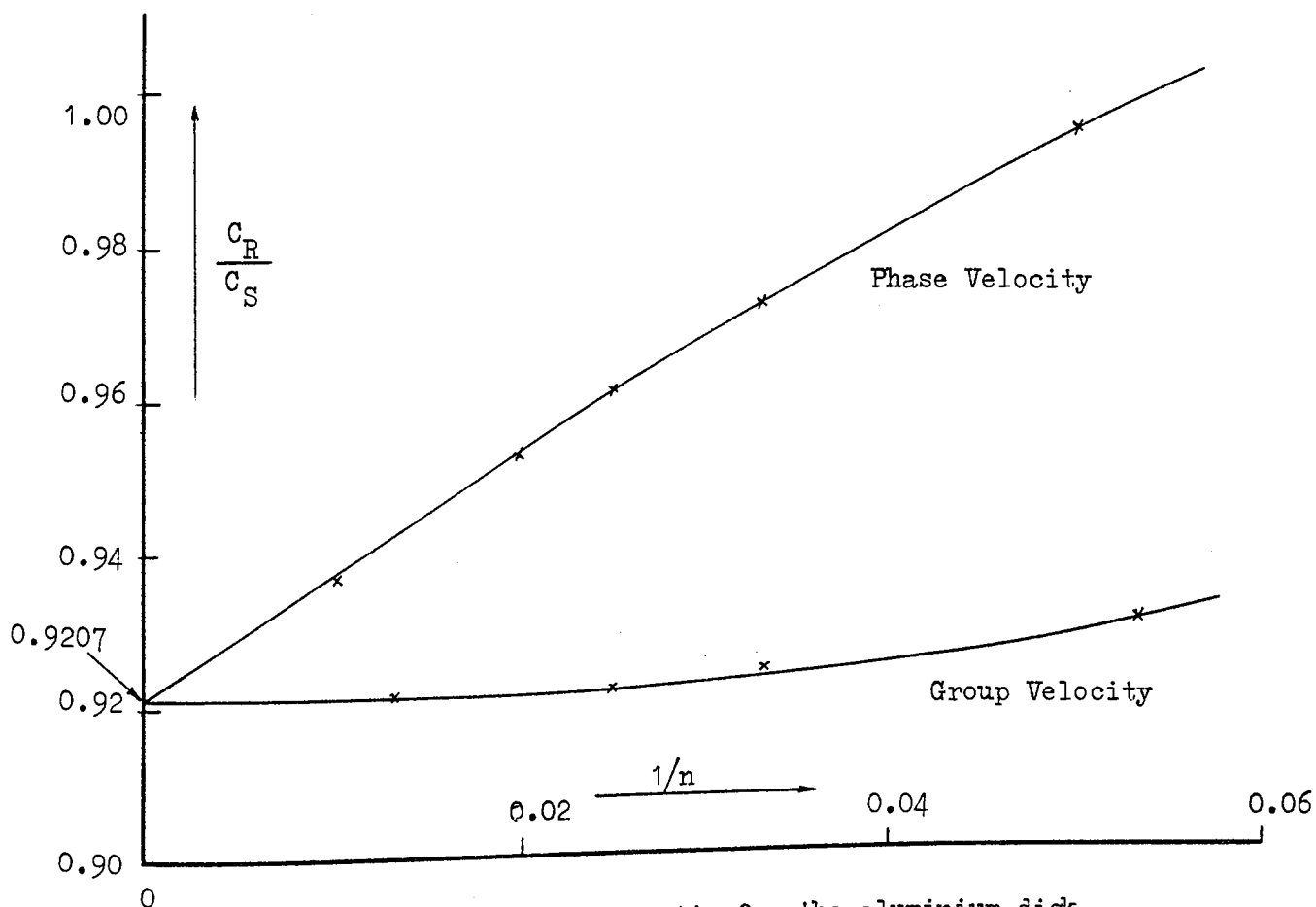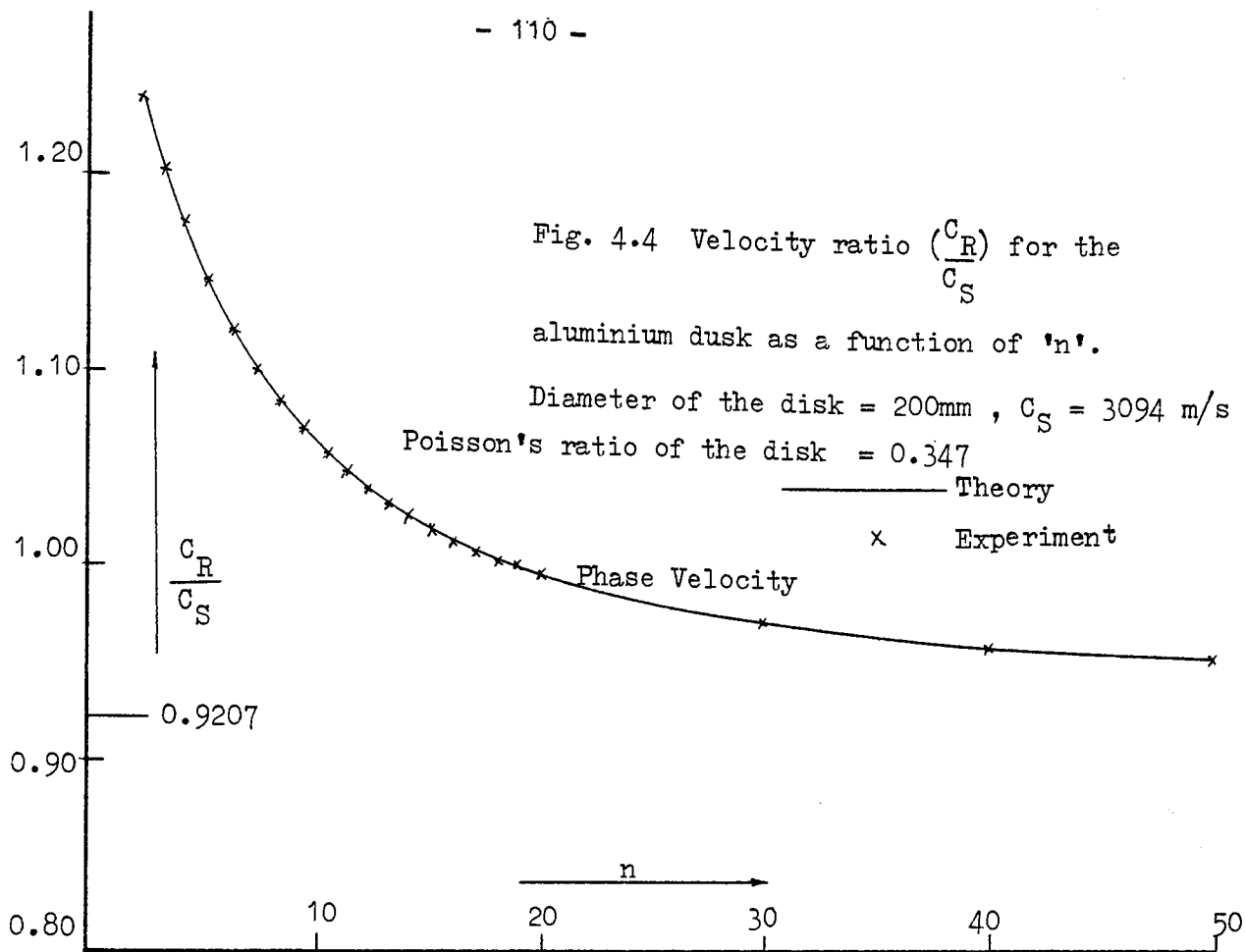
Fig. 4.4a   Velocity ratio for the aluminium disk as a function of (1/n)

Poisson's Ratio of the glass disk = 0.226

Diameter of the glass disk = 117.50 mm

c_S = 3356 m/s

——— Theory

X Experiment

Phase Velocity

$\frac{c_R}{c_S}$

n
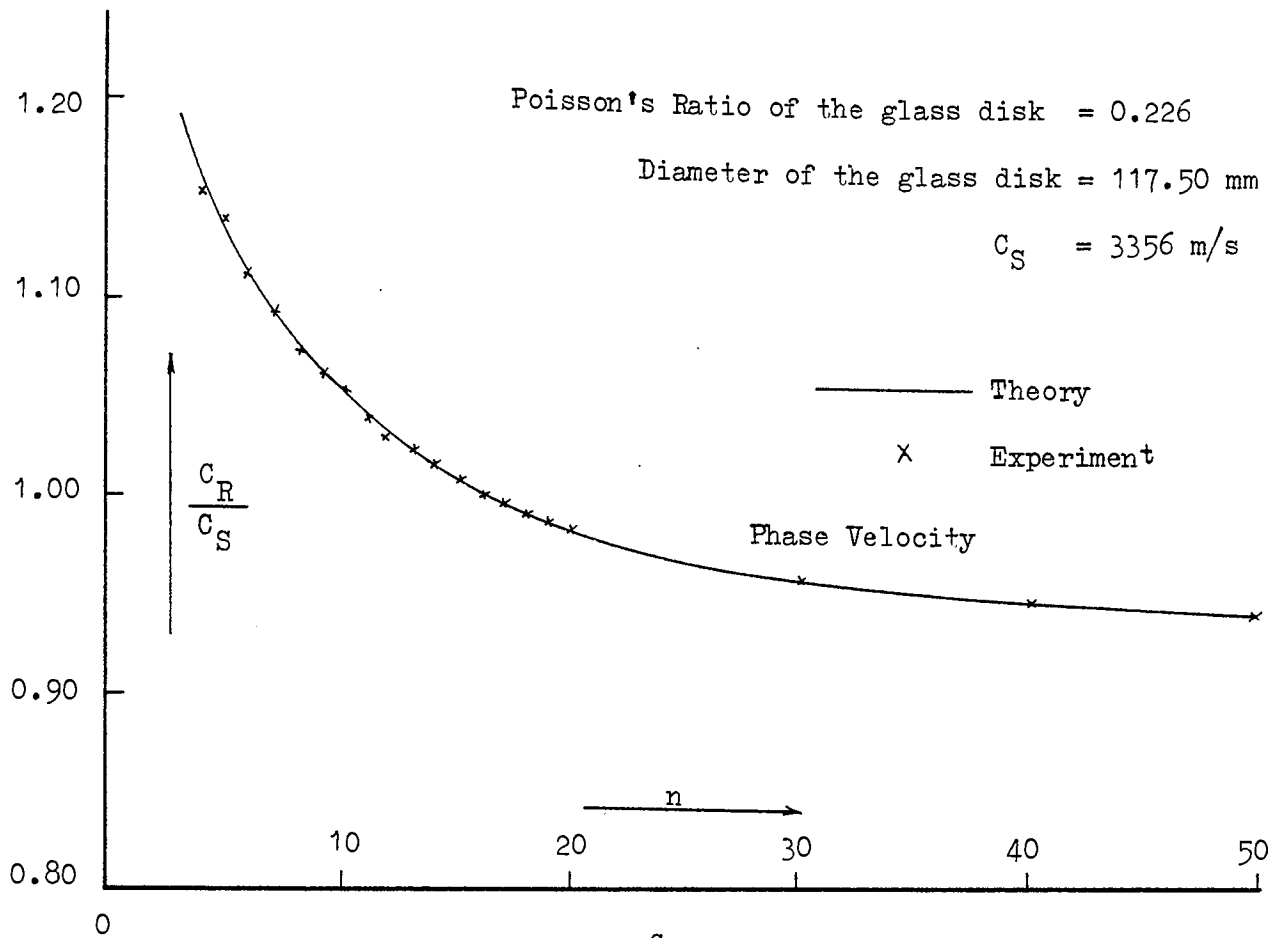
Fig. 4.5 Velocity ratio $\left(\frac{c_R}{c_S}\right)$ for the glass disk as a

function of 'n'.

$\frac{c_R}{c_S}$

Phase Velocity

Group Velocity

1/n
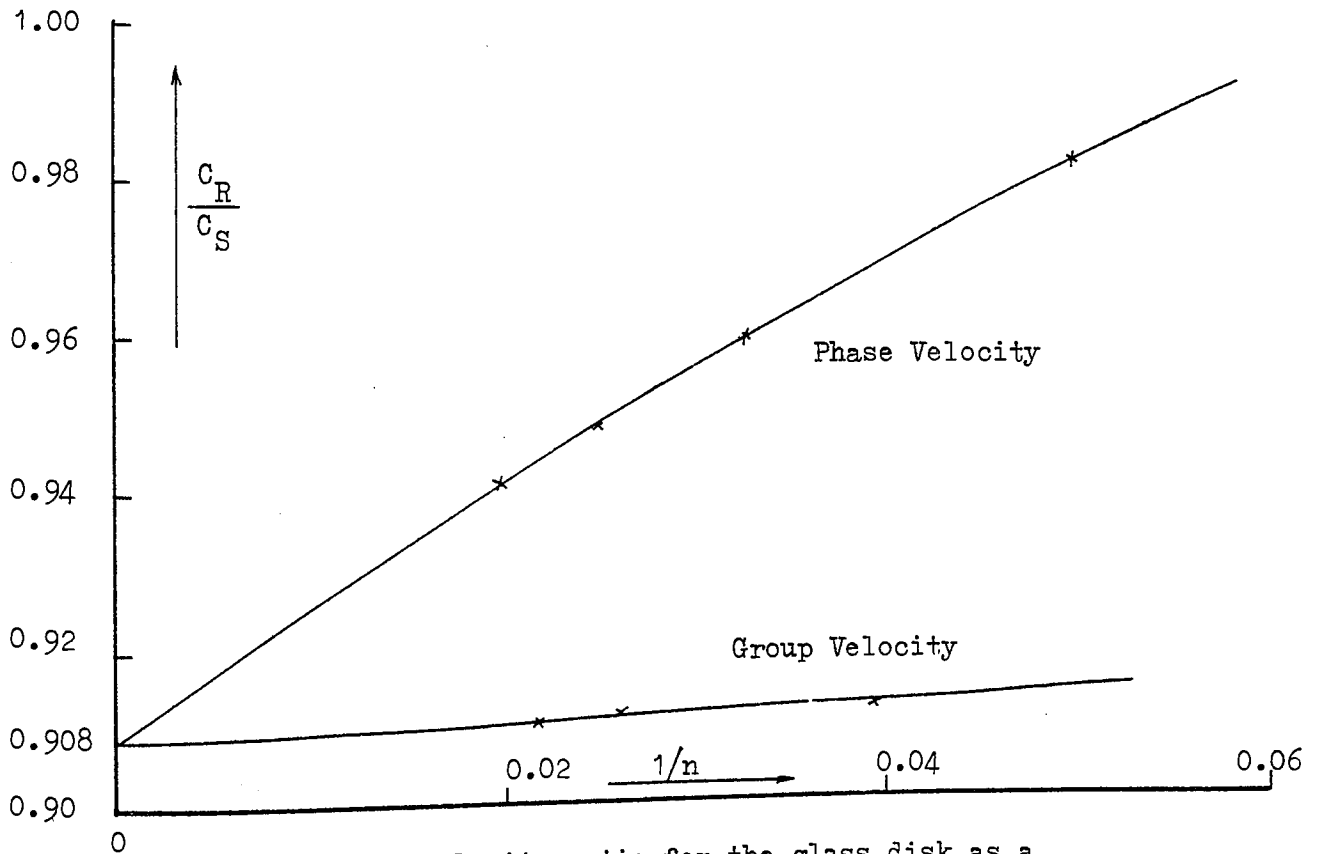
Fig. 4.5a Velocity ratio for the glass disk as a

function of (1/n).

76.2mm   38.1mm   76.2mm

Perimeter = 555mm

Aluminium thin sheet

C_S = 3094 m/sec.

Line
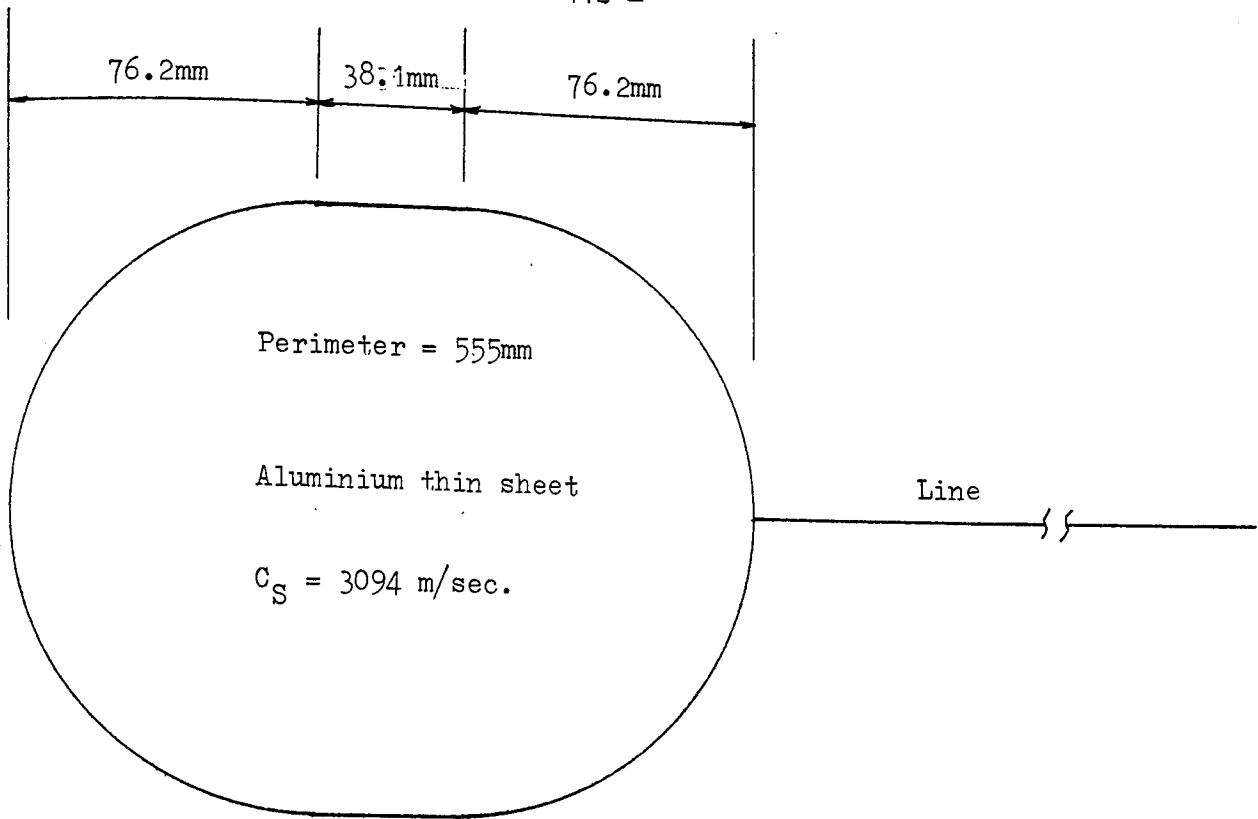
Figure 4.6 Dimension of a rectangular plate with two semi-circular ends.

$\dfrac{C_R}{C_S}$

Wavelength/Perimeter
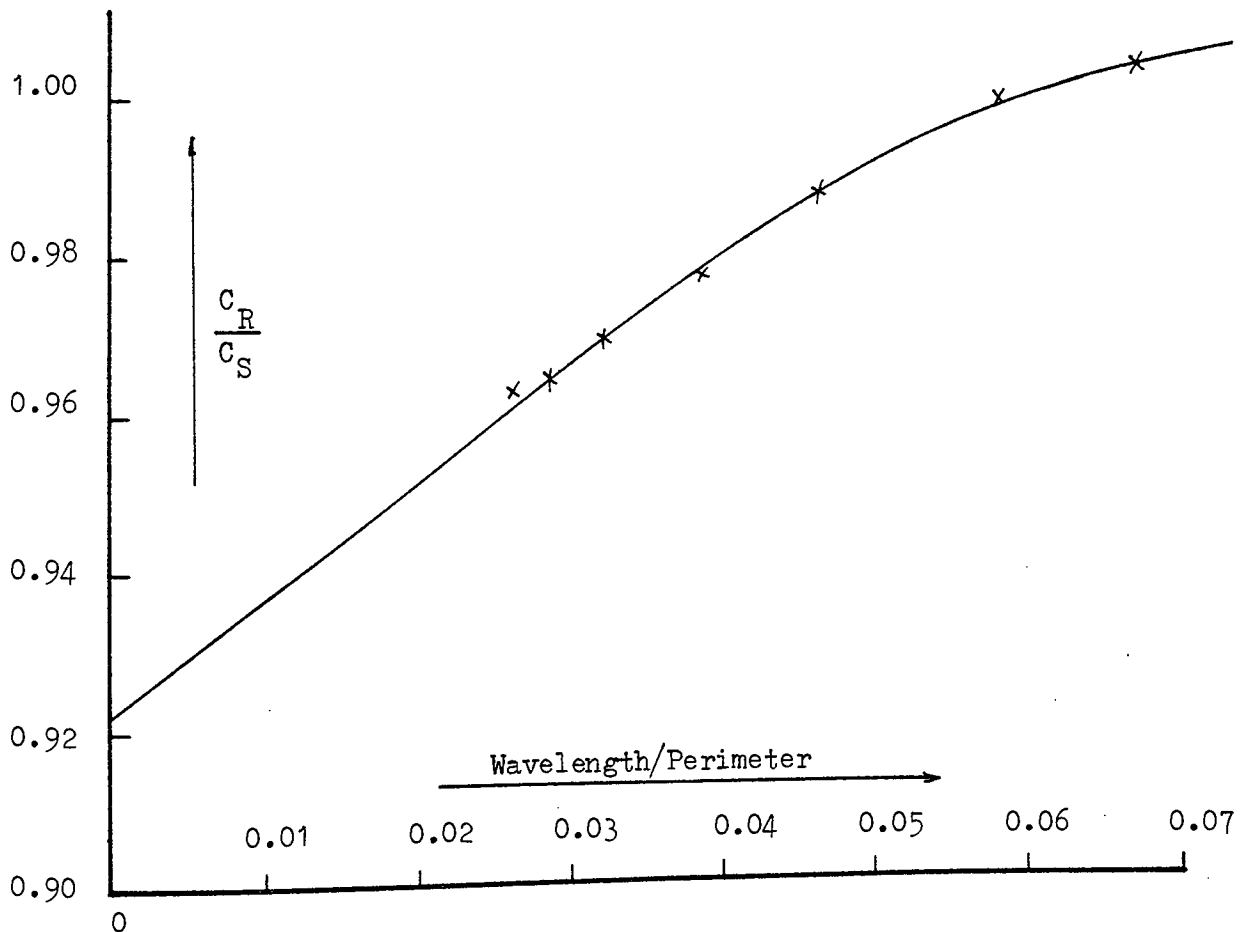
Figure 4.6a Experimental velocity ratio as a function of wavelength/perimeter for the circuit shown above.
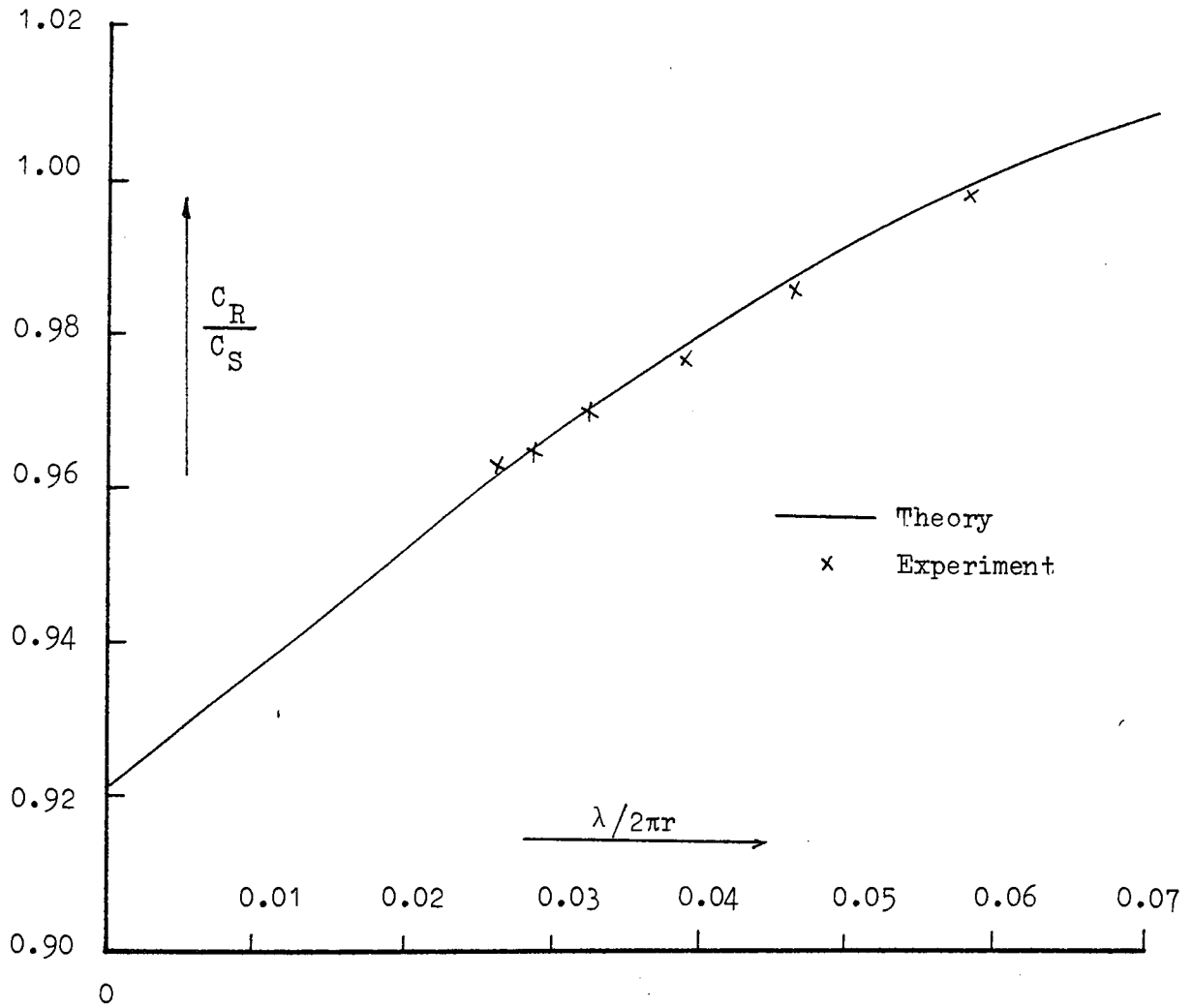
Figure 4.7 As in fig.4.6a, this shows the corresponding graph for a disk alone. (r = arc radius)
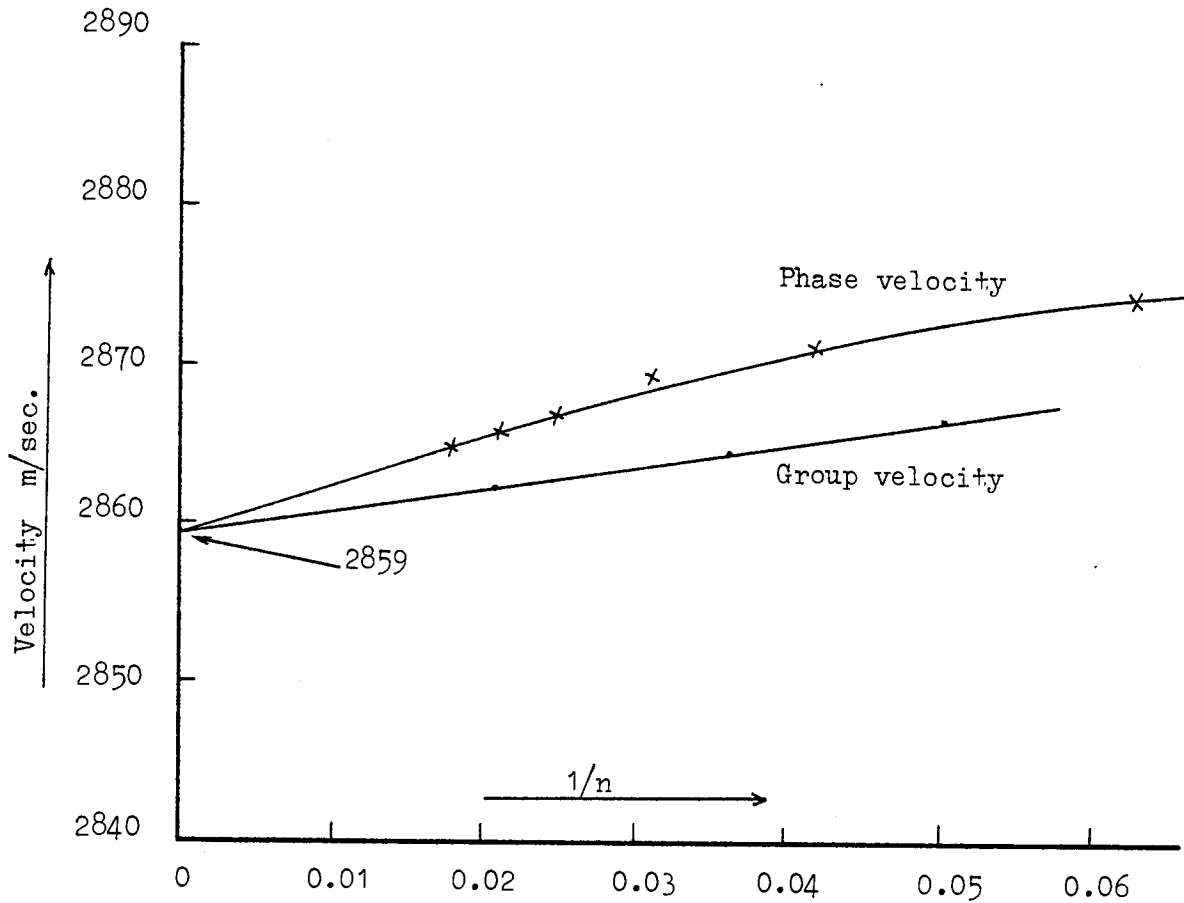
Figure 4.8 shows the edge surface waves velocities on an aluminium cylindrical shell. Mean diameter = 149mm, thickness = 3mm, Poisson's ratio = 0.34 and C_S = 3094 m/sec. The curves gives an asymptotic velocity of 0.924 which is slightly higher than the calculated value of 0.9201.
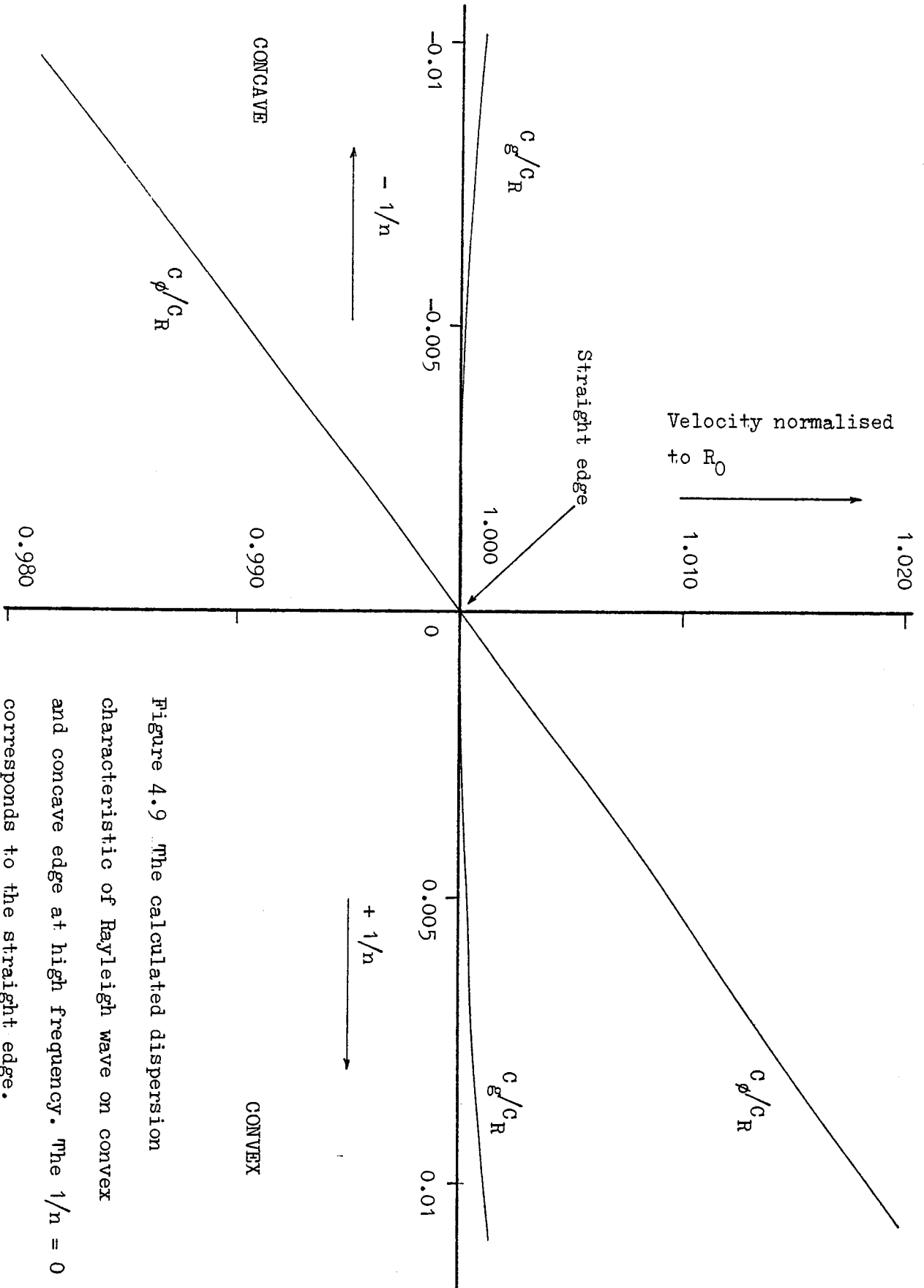
Figure 4.9 The calculated dispersion characteristic of Rayleigh wave on convex and concave edge at high frequency. The $1/n = 0$ corresponds to the straight edge.
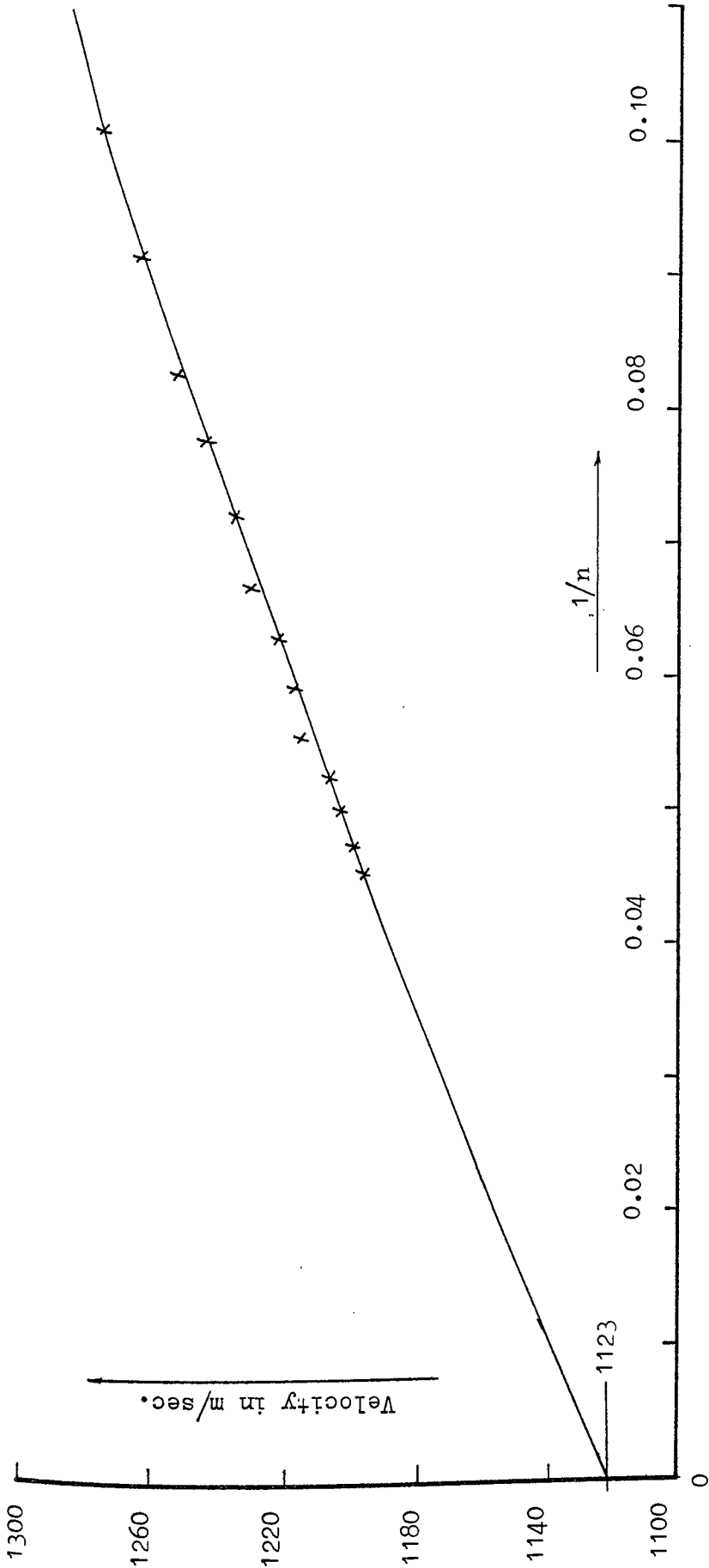
Figure 4.10 Two dimensional Rayleigh wave velocity on a billard ball, diameter = 48.5mm, Poisson's ratio = 0.35 and C_S = 1195 m/sec. The curve is drawn to fit the experimental points and predicted an asymptotic velocity of 1123 m/sec. When normalised to C_S, this gives a ratio of 0.94 which is close to the calculated value of 0.935 (for two dimensions).
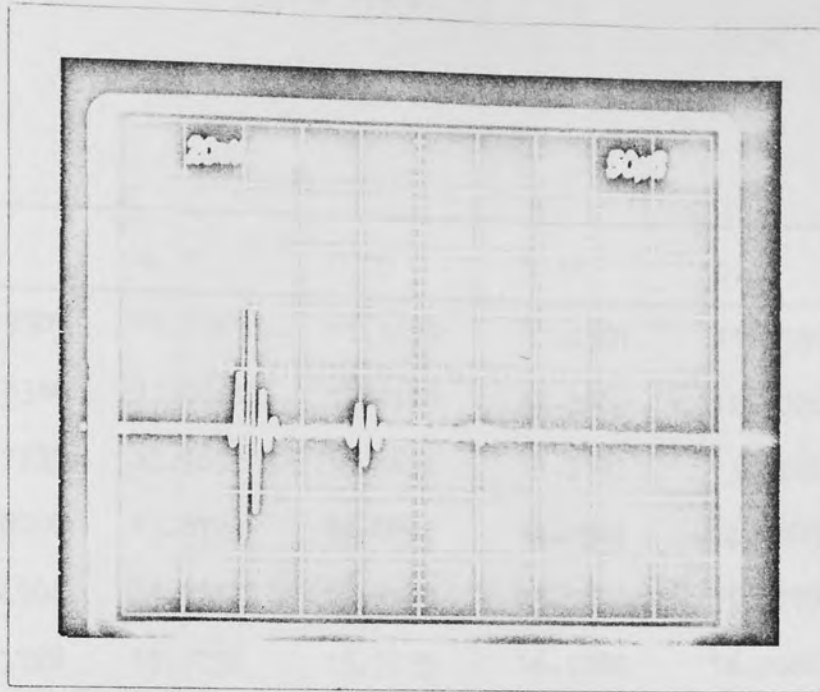
Figure 4.11a   Echoes travelling the billard ball.
The phase reversal of 1st and 2nd echoes indicate
a negative reflection coefficient.
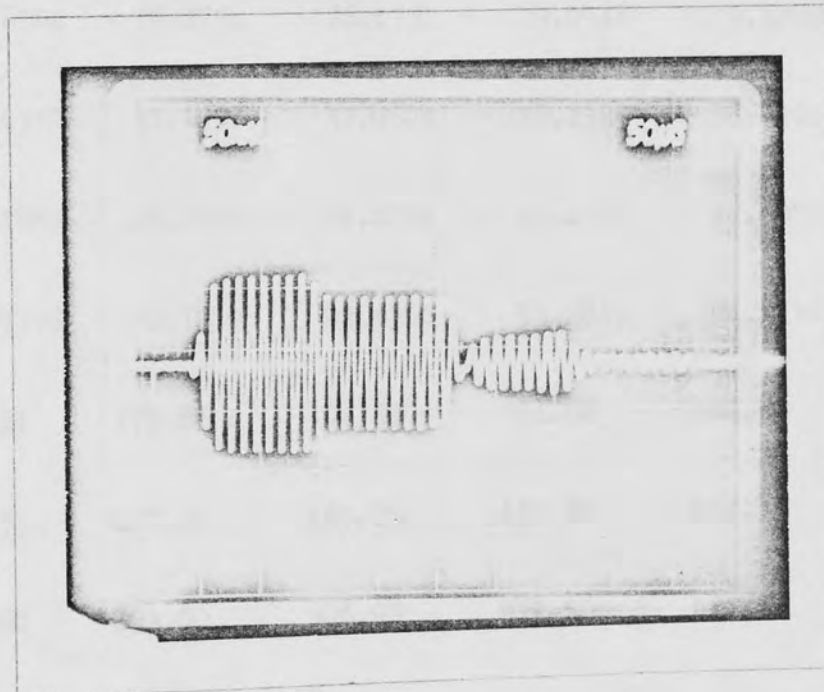
Figure 4.11b   Corresponding echo pattern on a billard
ball. Frequency = 91.85 kHz, mode number = 10 .
The wave is dispersive as the number of oscillations
in each step is 11 .

Poisson's Ratio	Ω_1					
n	0.0	0.10	0.20	0.30	0.40	0.50
11	10.9505	11.1569	11.3199	11.4501	11.5559	11.6428
12	11.8380	12.0641	12.2428	12.3860	12.5028	12.5984
13	12.7231	12.9692	13.1634	13.3193	13.4462	13.5510
14	13.6080	13.8723	14.0822	14.2507	14.3880	14.5014
15	14.4904	14.7743	14.9995	15.1804	15.3279	15.4514
16	15.3728	15.6752	15.9155	16.1089	16.2666	16.3970
17	16.3198	16.5752	16.8306	17.0362	17.2039	17.3428
18	17.1342	17.4742	17.7447	17.9625	18.1403	18.2874
19	18.0871	18.3726	18.6581	18.8880	19.0757	19.2311
20	18.8940	19.2708	19.5708	19.8127	20.0103	21.7398
30	27.6704	28.2294	28.6752	29.0348	29.3289	29.5727
40	36.4310	37.1691	37.7574	38.2320	38.6202	38.9420
50	45.1852	46.1000	46.8294	47.4178	47.8980	48.2974
100	88.9398	90.7080	92.1361	93.2839	94.2216	94.9971
200	176.34	179.86	182.64	184.88	186.68	188.14
500	438.55	447.30	454.25	459.80	464.30	468.05
1000	875.60	893.00	906.90	917.90	927.00	934.40

Table 4.1 Ω_1 values for the circular disks.

$$\left(\Omega_1 = \frac{\omega a}{c_S}\right)$$

h/a \ σ	R$_{1S}$					
	0.0	0.1	0.2	0.3	0.4	0.5
0	0.87400	0.89140	0.90520	0.91620	0.92515	0.93250
0.02	0.87405	0.89143	0.90521	0.91622	0.92517	0.93253
0.04	0.87411	0.89148	0.90523	0.91625	0.92519	0.93255
0.06	0.87421	0.89155	0.90529	0.91630	0.92523	0.93257
0.08	0.87434	0.89166	0.90537	0.91636	0.92528	0.93261
0.10	0.87452	0.89180	0.90548	0.91645	0.92534	0.93266
0.12	0.87473	0.89196	0.90561	0.91655	0.92542	0.93272
0.14	0.87498	0.89216	0.90577	0.91677	0.92551	0.93279
0.16	0.87527	0.89239	0.90594	0.91680	0.92562	0.93287
0.18	0.87560	0.89264	0.90614	0.91696	0.92574	0.93296
0.20	0.87596	0.89292	0.90636	0 91713	0.92587	0.93306

Table 4.2   Asymptotic velocity ratio for the wave travelling
on the edge of the cylindrical shell as a function of h/a and σ .

n	Freq.(kHz)	C_ϕ (m/sec.)	R_1(Expt.)	R_1(Cal.)
2	11.550	3614.40	1.1682	1.1732
3	17.745	3716.50	1.2012	1.2026
4	23.150	3636.39	1.1753	1.1750
5	28.200	3543.72	1.1454	1.1453
6	33.095	3465.70	1.1202	1.1198
7	37.880	3400.10	1.0990	1.0994
8	42.620	3347.37	1.0819	1.0818
9	47.320	3303.56	1.0678	1.0676
10	51.905	3261.29	1.0541	1.0556
11	56.595	3232.69	1.0449	1.0455
12	61.230	3206.00	1.0362	1.0368
13	65.855	3182.92	1.0288	1.0292
14	70.465	3162.46	1.0222	1.0226
15	75.075	3144.73	1.0164	1.0167
16	79.640	3127.46	1.0108	1.0115
17	84.260	3114.24	1.0066	1.0068
18	88.830	3100.75	1.0022	1.0026
19	93.395	3088.52	0.9983	0.9988
20	98.000	3078.76	0.9951	0.9953
30	143.535	3006.19	0.9716	0.9725
40	189.150	2971.16	0.9603	0.9604
50	234.420	2945.80	0.9521	0.9529
100	460.730	2894.85	0.9357	0.9373

Table 4.3 Experimental results on a 200mm diameter aluminium disk.

$$(R_1 = c_\phi/c_S)$$

n	Freq.(kHz)	C_ϕ (m/sec.)	R_1(Expt.)	R_1(Cal.)
2	21.336	3937.95	1.1734	1.1734
3	32.701	4023.84	1.1990	1.1985
4	42.508	3922.82	1.1689	1.1683
5	51.732	3819.24	1.1380	1.1370
6	60.567	3726.26	1.1103	1.1098
7	69.285	3653.67	1.0887	1.0882
8	77.914	3595.12	1.0713	1.0705
9	86.458	3546.10	1.0566	1.0560
10	94.956	3505.18	1.0445	1.0438
11	103.423	3470.66	1.0342	1.0343
12	111.893	3442.00	1.0256	1.0233
13	120.261	3414.83	1.0175	1.0157
14	128.672	3392.69	1.0109	1.0090
15	137.069	3373.15	1.0051	1.0032
16	145.386	3354.21	0.9995	0.9979
17	153.796	3339.52	0.9951	0.9932
18	162.143	3325.17	0.9908	0.9890
19	170.504	3312.60	0.9871	0.9852
20	178.808	3300.23	0.9834	0.9817
30	261.630	3219.25	0.9593	0.9590
40	344.730	3181.32	0.9480	0.9471
50	427.460	3155.83	0.9404	0.9400

Table 4.4   Measured velocity on a 117.5mm diameter glass disk.

$$(R_1 = C_\phi / C_S)$$

n	Freq.(kHz)	C_ϕ(m/sec.)	C_ϕ/C_{1R}	C_g(m/sec)	C_g/C_{1R}
80	229.90	2780.49	0.9761		
85	244.48	2782.82	0.9769		
90	259.20	2786.47	0.9782		
95	273.98	2790.36	0.9796	2853.0	1.0016
100	288.64	2792.67	0.9804		
105	303.44	2796.06	0.9816		
110	318.28	2799.50	0.9828		
115	332.96	2801.30	0.9834		
120	347.70	2803.43	0.9842		
125	362.46	2805.52	0.9849	2850.5	1.0007
130	377.16	2807.02	0.9854		
135	391.88	2808.56	0.9860		
140	406.66	2810.40	0.9866		
145	421.44	2812.11	0.9872		
150	436.22	2813.71	0.9878		
155	450.95	2814.88	0.9882	2849.5	1.0003
160	465.68	2816.00	0.9886		
165	480.38	2816.86	0.9889		
170	495.08	2817.68	0.9891		
175	509.82	2818.67	0.9895		
180	524.48	2819.17	0.9897		
185	539.22	2820.07	0.9900	2848.5	1.0000
190	553.94	2820.81	0.9903		
195	568.62	2821.32	0.9904		
200	583.30	2821.81	0.9906		

Table 4.5 Experimental results from a 308mm diameter hole.

Edge	Dispersion	Theory	Coupling
(1) Straight	None	Complete	Medium
(2) Convex	$c_\phi > c_g$	Complete	Strong
(3) Concave	$c_g > c_\phi$	Change sign of (2)	Weak
(4) Cylindrical Shell	$c_\phi > c_g$	Complete but not rigorous	Strong

Table 4.6 Characters of one dimensional surface waves on different edges.

CHAPTER 5

THE PROPAGATION OF MULTI-SURFACE WAVE
MODES ON CIRCULAR DISKS

CHAPTER 5

THE PROPAGATION OF MULTI-SURFACE WAVE MODES ON CIRCULAR DISKS

5.1 Non-Destructing Testing of Circular Disks

Ultrasonics is well established as one of the basic
techniques in the examination of defects in metals. A recent
application is the use of surface waves to measure and locate
defects near a surface. The journal, Material Evaluation,
published by American Society for Non-destructing (N.D.T.) and
British Journal of N.D.T. are a good source of information on
application in those fields. Reference (31) provides a brief
summary of those works. Normally, the reflected pulse and
amplitude is used as the reference in sizing the defects.
A mathematical treatment on those reflected echoes from a
shallow groove in the surface can be found in references (32)
and (33). Similarly, Lamb waves are widely used to inspect
thin geometrical structures using a scanning process$^{(34),(35)}$
$^{(24)}$. This is rather slow for manual operation and complicated
for automatic operation.

The wire-drive technique previously described in Chapter
2 is a very suitable instrument to inspect the defects along
the edges of thin continuous structures. A single surface
wave probe attached to the edge of the circular disk shown in
Fig. 5.1 launches the surface wave in both directions
around the circumference and receives the signal on
completion of the circuit. Any defect near the edge will
reflect signals within this transitional period and shown on

the oscilloscope display (Fig. 5.2). Various types of specimen such as ends of a cylindrical shell, elliptical plate and rectangular strip have been tested and proved to be effective. The time of flight measurement locates the defect and the reflected echo amplitude produces a good estimate of defect size. Fig. 5.3 shows the effect of the reflected echo of a strip on the crack depth. A crack, even a small fraction of wavelength deep, intercepts considerable wave energy and produces a large reflection. The reflected echo amplitude is almost linear with the small crack depth, this is consistent with the results reported in reference (32). The ease and simplicity should make this technique very attractive for unskilled or automated operation. The technique is also applicable to all other materials and could be extended to rapidly locate edged defects in propellers, turbines and compressor blades and other components.

5.2 Generation and Identification of a Second Surface Wave Mode

In carrying out the experiments, an unusual phenomenon
was observed. The reflected echo amplitude from the defects
which travelled the longer route had a larger amplitude than
that of the echo on the much shorter route. To investigate
this paradox, experiments with two wires were performed on the
edges of a circular disk and subsequently other structures.
Fig. 5.4 shows the experimental arrangement, a wire is used
to launch the surface wave round the circumference and a
second wire situated at a position θ from the drive point is
used as a receiver. Two echoes of amplitudes E_1 and E_2 for
the routes θ and $2\pi-\theta$ were observed and recorded. The
phenomenon was un-ambiguously confirmed, Fig. 5.4a being a
good example. This paradox of a stronger signal àt the greater
distance occurring in radio communications where a direct
wave and one reflected form the ionisphere combine in phase
to increase and decrease the signal depending on the relative
path lengths. In shallow water sonar, there is a similar
effect when the energy travels in two propagation modes. The
signal interferenœ effect occurs because, while the distances
are the same, the mode velocities are different. The latter
was ultimately established as the case described here. Figs.
(5.5) and (5.6) show the corresponding echo amplitudes E_1 and
E_2 on the end of a cylindrical shell and the circular hole in
a large sheet of metal. These observations strongly suggest
that the phenomenon appears on convex boundaries only. It
is noted that the amplitude ratio (E_2/E_1) is a function of

frequency and the received position θ. The amplitude ratio (E_2/E_1) has an oscillatory nature along the frequency axis for a fixed value of θ and a value greater than one in most frequencies.

5.3 Second Surface Wave Mode

The previous analyses have only considered the first root of equation (4.1) which represents the normal Rayleigh surface wave and other solutions are neglected. Nevertheless, it is possible that the high order modes are excited and a second signal combines with the normal surface wave mode.

The disk frequency equation (4.1) must contain this second mode solution which like the Rayleigh surface waves will have both lognitudinal and shear components. To analyse the character of such modes, the particle displacement S may be expressed in terms of wave potentials ϕ_m and ψ_m representing the longitudinal and shear components of mode m respectively. From the well established relations, the ϕ_m and ψ_m satisfy the equation of wave motion (equation (3.7)). In polar co-ordinates, they have the form:

$$\phi_m = A_m \ J_n (k_{m,\ell} r) \ \cos n\theta$$

$$\left. \right\} \qquad\qquad (5.1)$$

$$\psi_m = B_m \ J_n (k_{m,s} r) \ \sin n\theta$$

where

$$k_{m,\ell} = \frac{\omega_m}{C_p} = \frac{1}{a} \frac{\Omega_m}{a}$$

$$k_{m,s} = \frac{\omega_m}{C_s} = \frac{\Omega_m}{a}$$

This represents the angular waves propagating in the θ direction in the absence of attenuation. The expression of radial (U_r) and tangential (U_θ) displacement components is

obtained by using equation (5.2).

$$
\begin{bmatrix} U_r \\ \\ U_\theta \end{bmatrix} = \begin{bmatrix} \dfrac{\partial}{\partial r} & \dfrac{1}{r}\dfrac{\partial}{\partial \theta} \\ \\ \dfrac{1}{r}\dfrac{\partial}{\partial \theta} & -\dfrac{\partial}{\partial r} \end{bmatrix} \begin{bmatrix} \phi_m \\ \\ \psi_m \end{bmatrix} \qquad (5.2)
$$

They have the same form as shown in equations (2.31) and (2.32) when m is 1. The edge of the disk being free, the stress σ_{rr} and $T_{r\theta}$ vanish at r=a giving the characteristic frequency equation already shown in equation (4.1). The first root (Ω_1) of this equation has been analysed extensively in a preceding chapter in terms of the Rayleigh surface waves. The second mode can be obtained from equation (4.1) by following the second root for each 'n' value. It was found that the phase velocity, unlike the first root solution was always greater than the shear velocity and thus prevented the use of the Debye's expansion of equation (4.8). The velocity characteristics of the next two additional roots of equation (4.1) designated as Ω_2 and Ω_3 with n values up to 100 for $\sigma=0.34$ were evaluated. Fig. 5.7 shows the calculated phase and group velocities of the first two higher modes. The velocity is normalised to the shear. It is evident that both velocities are greater than the shear velocity i.e. $\dfrac{\Omega_3}{n} > \dfrac{\Omega_2}{n} > 1$. This is true even at very high frequency where λ/a is small and the straight edge condition is approached. A polynominal curve fitting program was used to determine the extrapolated velocity ratio at 1/n=0. This also provides a simple mathematical expression for the phase and group velocities which gives,

$$C_\phi\Big|_{m=2} = C_s\left[1 + \frac{12.58}{n} - \frac{155.30}{n^2} \ldots\ldots\right] \tag{5.3}$$

$$C_\phi\Big|_{m=3} = C_s\left[1 + \frac{21.06}{n} - \frac{325.17}{n^2} \ldots\ldots\right] \tag{5.4}$$

For the group velocity, the expressions are therefore

$$C_g\Big|_{m=2} = C_s\left[1 + \frac{155.30}{n^2} \ldots\ldots\right] \tag{5.5}$$

$$C_g\Big|_{m=3} = C_s\left[1 + \frac{325.17}{n^2} \ldots\ldots\right] \tag{5.6}$$

It is the combination of these waves with the Rayleigh waves which gives the anomalous echo amplitude observed experimentally. The velocity difference is considerable as the first wave travels at about the one dimensional Rayleigh waves velocity and others at the shear velocity. Thus for aluminium, the waves would be in phase every eleven wavelengths.

It is of interest that the velocity for these high order modes converges to the shear velocity. This has a parallel in the Lamb waves in plates. While the asymmetric and symmetric modes of zero order approach the two dimensional Rayleigh wave velocity as a limit, the high order modes approach the shear velocity[36].

Concentrating now on the wave potential functions and from equation (4.8), the Bessel term in equation (5.1) when λ/a is small can be approximately expressed as

$$J_n(Dr) \simeq \frac{\exp\left[-n(\tanh\alpha - \alpha)\right]}{(2\pi n \, \tanh\alpha)^{\frac{1}{2}}} \qquad (5.7)$$

where

$$Dr = \frac{n}{\cosh\alpha}$$

This expression is valid for $n > Dr$ which is the condition for the first surface wave mode developed in the previous analysis. Consider the wave propagating near the edge so that $\frac{2\pi}{\lambda} \simeq \frac{n}{r}$. Then for large values of 'n'

$$n(\tanh\alpha - \alpha) = (1 - \text{sech}^2\alpha)\frac{d\alpha}{d(1/n)} \qquad (5.8)$$

where

$$\text{sech}\alpha = \frac{D}{\varepsilon}$$

$$\frac{d\alpha}{d(1/n)} = \frac{\varepsilon r}{(1 - \frac{D^2}{\varepsilon^2})^{\frac{1}{2}}}$$

and

$$\varepsilon = \frac{2\pi}{\lambda}$$

From this, it follows that the potentials for the first normal surface wave mode have the form:

$$\phi_1 = \frac{A_1}{(2\pi g_1 a)^{\frac{1}{2}}} \exp g_1(a-z) = \text{constant} \times \exp(-g_1 z) \qquad (5.9)$$

$$\psi_1 = \frac{B_1}{(2\pi p_1 a)^{\frac{1}{2}}} \exp p_1(a-z) = \text{constant} \times \exp(-p_1 z) \qquad (5.10)$$

Where $z = a - r$ which is the penetration depth and $a \gg z$ is assumed.

$$g_1^2 = \epsilon^2 - k_{1,\ell}^2$$

$$p_1^2 = \epsilon^2 - k_{1,s}^2$$

$$\frac{B_1}{A_1} = \frac{J_n(\Omega_1/\theta)}{J_n(\Omega_1)} \times \left[\frac{\frac{\Omega_1^2}{2} - n^2 - n + M_n(\Omega_1/\theta)}{n\{M_n(\Omega_1) - n - 1\}} \right]$$

The above equations show that the potentials of shear and longitudinal components represent the propagation along the θ direction but have an exponential decay away from the edge. This is the classical Rayleigh wave functions and having similar form to that for straight edge of equation (3.8).

With various approximations, the U_r and U_θ displacement components can be obtained . In using equation (4.12) and retaining the first linear term,

$$\frac{B_1}{A_1} \simeq \left(\frac{p_1}{g_1}\right)^{\frac{1}{2}} \times \frac{\left[(\frac{R_1}{2} - 1) + \frac{1}{n}(1 - \frac{R_1^2}{\theta^2})^{\frac{1}{2}}\right] \times \exp\left[g_1 - p_1)a\right]}{(1 - R_1^2)^{\frac{1}{2}} + \frac{1}{n}\left[\frac{(1 - 2R_1^2) - (1 + 2R_1^2)(1 - R_1^2)^{\frac{1}{2}}}{2(1 - R_1^2)^{\frac{1}{2}}}\right]} \qquad (5.11)$$

where $R_1 =$ the velocity of first surface wave mode normalised to the shear velocity.

Combining equations (5.9), (5.10), (5.11) and (5.2) the displacements U_r and U_θ for $m=1$ are

$$U_r\bigg|_{m=1} = \frac{A_1 \exp(g_1 a)}{(2\pi g_1 a)^{\frac{1}{2}}} g_1 \times \left[\exp(-g_1 z) - \frac{\chi_1 \exp(-p_1 z)}{(1 - \frac{R_1^2}{\theta^2})^{\frac{1}{2}}} \right]$$

$$(5.12)$$

where $\chi_1 = \dfrac{(1-\frac{R_1^2}{2}) + \frac{1}{n}(1-\frac{R_1^2}{B^2})^{\frac{1}{2}}}{(1-R_1^2)^{\frac{1}{2}} + \frac{1}{n}\left[\dfrac{(1-2R_1^2)-(1+2R_1^2)(1-R_1^2)^{\frac{1}{2}}}{2(1-R_1^2)^{\frac{1}{2}}}\right]}$

$$U_\theta\bigg|_{m=1} = -\frac{A_1 \exp(g_1 a)}{(2\pi g_1 a)^{\frac{1}{2}}} \varepsilon \times \left[\exp(-g_1 z) - \chi_2 \exp(-p_1 z)\right]$$

(5.13)

where $\chi_2 = \dfrac{(1-\frac{R_1^2}{2}) + \frac{1}{n}(1-\frac{R_1^2}{B^2})^{\frac{1}{2}}}{1 + \frac{1}{n}\left[\dfrac{(1-2R_1^2)-(1+2R_1^2)(1-R_1^2)^{\frac{1}{2}}}{2(1-R_1^2)^{\frac{1}{2}}}\right]}$

The 1/n terms occur in equations (5.11) and (5.12) arising from the nature of curvature. For $n \geqslant 100$, the 1/n terms are small compared to their adjacent terms, hence the curvature does not have a significant effect on the amplitude functions when $\frac{\lambda}{a} \leqslant .063$. It follows that a surface wave propagating along the boundary is not feasible for high λ/a values when $C_\phi \geqslant C_s$ because equations (5.12) and (5.13) are no longer valid and displacements would not decay exponentially with depth.

As $n \rightarrow \infty$ which is the situation for zero curvature and for $\sigma = 0.34$, equations (5.12) and (5.13) reduce to

$$U_r = \text{constant} \times g_1\left[\exp(-g_1 z) - 1.7337\exp(-p_1 z)\right] \quad (5.14)$$

$$U_\theta = \text{constant} \times \varepsilon \left[\exp(-g_1 z) - 0.5768\exp(-p_1 z)\right] \quad (5.15)$$

Substituting the numerical values of $\frac{g_1}{\varepsilon}$ and $\frac{p_1}{\varepsilon}$ and normalised the above equations to U_{r_o}, the radial component at $r=a$, this becomes

$$\frac{U_r}{U_{r_o}} = 2.363\exp(-2.463z/\lambda) - 1.363\exp(-5.334z/\lambda) \qquad (5.16)$$

$$\frac{U_\theta}{U_{r_o}} = -0.926\exp(-2.463z/\lambda) + 1.606\exp(-5.334z/\lambda) \qquad (5.17)$$

This is the exact expression for the displacements in straight edge.

Because of the velocity difference, the waves of the higher order modes will behave differently from the normal Rayleigh wave. Consider the wave potential of the shear component (ψ_2) of the first higher mode, the Debye's asymptotic expansion is not applicable as the argument term has a value larger than the order, i.e. $\Omega_2 > n$. It is necessary to express the ψ_2 at very high frequencies (λ/a is small) by the approximation of equation (5.18).

$$\psi_2 \simeq A_2 \hat{\psi}_2 \exp(in\theta) \qquad (5.18)$$

where

$$\hat{\psi}_2 = J_n(k_{2,s}r) \simeq \frac{1}{(\pi)^{\frac{1}{2}}} \left(\frac{2}{k_{2,s}r}\right)^{\frac{1}{3}} A_i(Y)$$

and

$$k_{2,s} = \frac{\Omega_2}{a}$$

A_i is the Airy integral and it is expressible in integral form and $Y = \left(\frac{2}{k_{2,s}r}\right)^{\frac{1}{3}}(n - k_{2,s}r)$.

Consider the waves propagating near the edge and let $r \simeq a$ except for the term $(n - k_{2,s} r)$, then $(n - k_{2,s} r) = (\varepsilon - k_{2,s}) a + k_{2,s} z$ where z is the distance measured from the edge towards its centre and $z \ll a$. Because the values of ε and $k_{2,s}$ are close, then $\varepsilon - k_{2,s} \simeq \dfrac{\varepsilon^2 - k_{2,s}^2}{2 k_{2,s}}$. Therefore Y can be expressed as

$$Y = \left(\frac{1}{2\Omega_2^2}\right)^{2/3} p_2^2 a^2 + (2\Omega_2^2)^{1/3} z/a \qquad (5.19)$$

where

$$p_2^2 = \varepsilon^2 - k_{2,s}^2$$

p_2 has the same form as the depth function of the shear potential in a straight edge, but the shear potential is represented by the Airy integral.

In transforming the term Y of equation (5.18) into the form shown in equation (5.19), the asymptotic relations of the Airy function[38] can be used. In this case, as $\Omega_2 > n$, the function $A_i(Y)$ has an oscillatory behaviour for negative 'Y' with a period and amplitude which slowly diminish with increasing $|Y|$. For $\zeta \gg 1$, the following asymptotic relation is valid,

$$A_i(Y) = (-Y)^{-1/4} \sin\left(\zeta + \frac{\pi}{4}\right) \left[1 - \frac{\zeta_2}{\zeta^2} + \frac{\zeta_4}{\zeta^4} \cdots \right]$$

$$- (-Y)^{-1/4} \cos\left(\zeta + \frac{\pi}{4}\right) \left[\frac{\zeta_1}{\zeta} - \frac{\zeta_3}{\zeta^3} + \frac{\zeta_5}{\zeta^5} \cdots \right] \qquad (5.20)$$

where $\zeta = \frac{2}{3}(-Y)^{3/2}$

and $\zeta_1 = \frac{5}{72}$, $\qquad \zeta_2 = \frac{(5.11) \cdot 7}{1 \cdot 2 \cdot (72)^2}$

$$\zeta_n = \frac{5.11 \ldots (6n-1) \cdot 7 \cdot 13 \ldots (6n-5)}{1.2 \ldots n(72)^n}$$

The properties of the Airy functions are fully described in reference (39).

The ψ_m (m$\geqslant$2) oscillates away from the boundary and is not confined to the edge.

For the wave potential of the longitudinal component ϕ_2, equation (5.17) is still valid as $\frac{\Omega_2}{\bar{a}} < n$, therefore

$$\phi_2 \simeq B_2 \, \hat{\phi}_2 \, \exp(in\theta) \qquad\qquad (5.21)$$

where $\hat{\phi}_2 = J_n(k_{2,\ell} r) = \dfrac{\exp(g_2 a)}{(2\pi g_2 a)^{\frac{1}{2}}} \exp(-g_2 z)$

and $\quad g_2^2 = \epsilon^2 - k_{2,\ell}^2$

This is similar to the classical Rayleigh wave function which has an exponentially decaying motion and can be considered as a wave near the edge but with a smaller decaying rate as $g_2 < g_1$.

The above analysis for a disk thus identifies another type of wave termed second surface wave mode which travel faster than the shear wave. The ϕ_2 component behaves as the normal Rayleigh mode, but ψ_2 oscillates away from the boundary. The higher order modes (m$>$3) are not considered in detail since $\frac{\Omega_m}{\bar{a}} > n$ and neither of the components ϕ_m and ψ_m

will have exponentially decaying motion so that a surface wave mode in this case is not feasible. Table 5.1 shows the calculated value of Ω_1, Ω_2 and Ω_3 for $\sigma = 0.34$ with 'n' up to 100. The phase and group velocities for each case are also included.

5.4 Comparison with Experiments

The characteristics of the first and second normal wave modes both of which are assumed to be excited by the line drive enable a theory for the oscillatory nature of signal amplitude to be developed. The two types of wave propagate along the surface of the circular disk but with different velocities, the longitudinal echo amplitudes E_1 and E_2 at receiving position θ and $(2\pi-\theta)$ for lossless medium are designated as:

$$E_1 = \left[U_1 \cos(v_1\theta) - U_2 \cos(v_2\theta) \right] \exp(in\theta) \qquad (5.22)$$

$$E_2 = \left[U_1 \cos(v_1(2\pi-\theta)) - U_2 \cos(v_2(2\pi-\theta)) \right] \exp(in\theta)$$
$$(5.23)$$

where U_1 and U_2 are the amplitude constants of the first and second surface wave modes as excited by the drive. The ratio of U_2/U_1 is assumed to be frequency independent and has a value of less than one,

and
$$v_1 = \frac{\omega a}{R_1 C_s} = \frac{\Omega_1}{R_1}$$

$$v_2 = \frac{\omega a}{R_2 C_s} = \frac{\Omega_2}{R_2}$$

In retaining the first linear term, R_1 and R_2 can be expressed as

$$\left. \begin{array}{l} R_1 = R_o \left(1 + \dfrac{k_1}{n}\right) \\[2mm] R_2 = R_o \left(1 + \dfrac{k_2}{n}\right) \end{array} \right\} \qquad (5.23a)$$

where k_1 and k_2 are determined by the best straight line fit program and found to be 1.7885 and 9.4773 respectively (for $\sigma = 0.34$).

Substituting equation (5.23a) into expression v_1 and v_2 yields

$$v_1 = \frac{\omega a}{C_{1R}} - 1.7885$$

$$\left.\right\}$$ (5.23b)

$$v_2 = \frac{\omega a}{C_s} - 9.4773$$

In so doing, equation (5.22) can be expressed as

$$E_1 = U_1\{1+U^2-2U\cos|(v_1-v_2)\theta|\}\cos(v_1\theta+e_1) \qquad (5.24)$$

where $\quad e_1 = \dfrac{\sin v_1\theta - U\sin v_2\theta}{\cos v_1\theta - U\cos v_2\theta} \qquad$ and $\quad U = \dfrac{U_2}{U_1}$

Since v_1 and v_2 are unequal, the amplitude of first and second surface mode continually shifts in relative phase as the waves travel. After a propagation distance $L=\pi d\theta$ such that $\left[\dfrac{f}{C_{1R}} - \dfrac{f}{C_s} + \dfrac{7.6888}{\pi d}\right] L = 2\pi$, they are in antiphase. Because of this beating effect, E_1 will have a periodic value along the propagation distance. The 'beat wavelength' λ_b, the length of one spatial period of the waves between an in-phase and anit-phase condition, is

$$\lambda_b = \frac{2 R_1}{(1-R_1)}\lambda \qquad (5.24a)$$

For aluminium, $R_1 = 0.92$, $\lambda_b = 11\lambda$.

Because the input amplitude is arbitrary, the normalisation of the echo amplitude E_1 is necessary. Since there is no interference between the amplitude E_1 and E_2, the ratio of E_2/E_1 can be expressed as:

$$\frac{E_2}{E_1} = \left[\frac{1 + U^2 - 2U\cos\left[(v_1+v_2)(2\pi-\theta)\right]}{1 + U^2 - 2U\cos\left[(v_1+v_2)\theta\right]} \right]^{\frac{1}{2}} \qquad (5.25)$$

From equation (5.25), it also follows that the echo ratio E_2/E_1 is not only a function of frequency and receiving position θ, but also the disk diameter.

The two wire experiments were then carried out on two thin aluminium disks of diameter 308 mm, 185.16 mm and thickness 1 mm. To minimize the effect arising from attenuation, the receiving positions were chosen at $\theta \geqslant 90^\circ$. Therefore a short burst of frequency 'f' was launched along the edge in both directions and the echo amplitudes E_1 and E_2 which travel a distance of $a\theta$ and $a(2\pi-\theta)$ were measured carefully. Fig. 5.8a shows the experimental echo ratio E_2/E_1 as a function of the launched frequency 'f' from a 185.16 mm diameter disk, θ being 120°; the calculated curve in using equation (5.25) is also shown in Fig. 5.8b where U is assumed to be 0.3. For the receiving position $\theta=90^\circ$, Figs. 5.9a and 5.9b give the corresponding experimental and calculated results. To demonstrate the effect of disk diameter on E_2/E_1, Figs 5.10a and 5.10b show the results on a 308 mm diameter disk with $\theta=120^\circ$.

Examination of the graphs showsquite good qualitative
agreement between theory and experiment but the correspondence
is not complete. The deviations could arise from:

(1) Only the second surface wave is considered and all the
     other high surface wave modes are ignored.

(2) The energy of high surface wave modes will only confine
     to the edge when λ/a is very small. This explains why
     the experimental result of E_2/E_1 is approximately one
     when $f \leqslant 500$ kHz.

(3) The attenuation of the surface waves is neglected in the
     theory and this would cause error particularly when λ/a
     is very small. Care was taken to minimize the scattering
     by polishing the edges.

(4) The spurious signals arising from the supports, joints
     eventually limit the accuracy in experiments.

A further refinement of the theory would require the
exact information of the field distribution on the first and
the higher surface wave modes. Moreover, the attenuation
should be included.

The oscillatory nature of the signal amplitude is
evident in both theory and experiments. The periodicity
changes considerably with disk diameter and both theory and
experiments show this change. It is considered that the
phenomenon observed experimentally has been confirmed by the
analysis and improves the understanding of the propagation
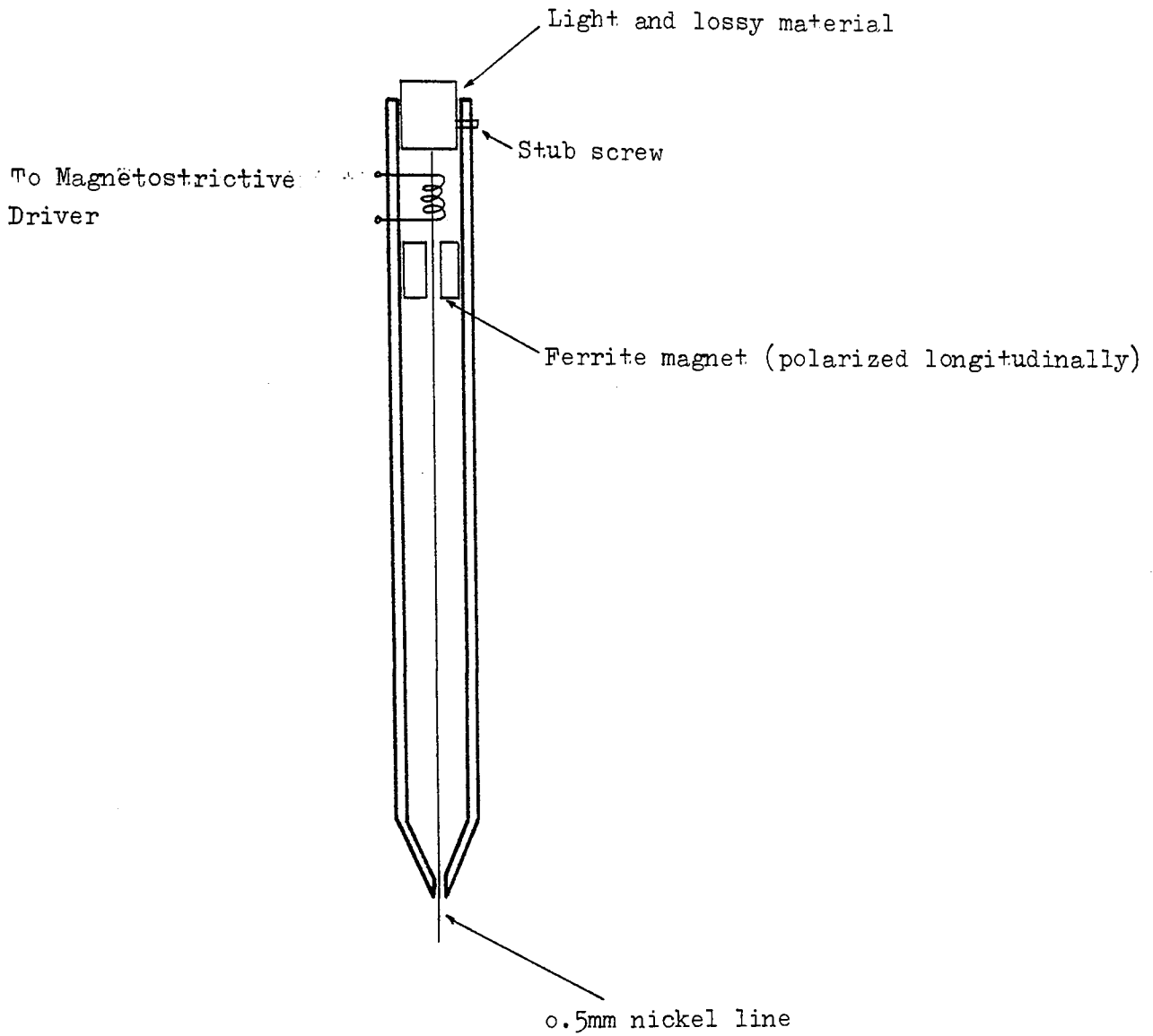of waves on a curved surface.

Light and lossy material

Stub screw

To Magnetostrictive
Driver

Ferrite magnet (polarized longitudinally)

o.5mm nickel line

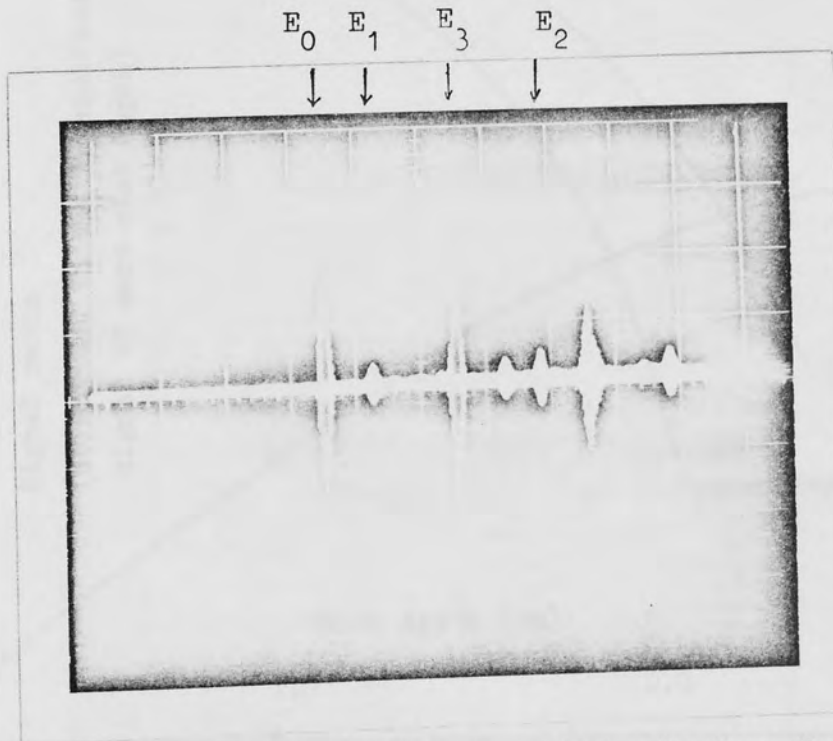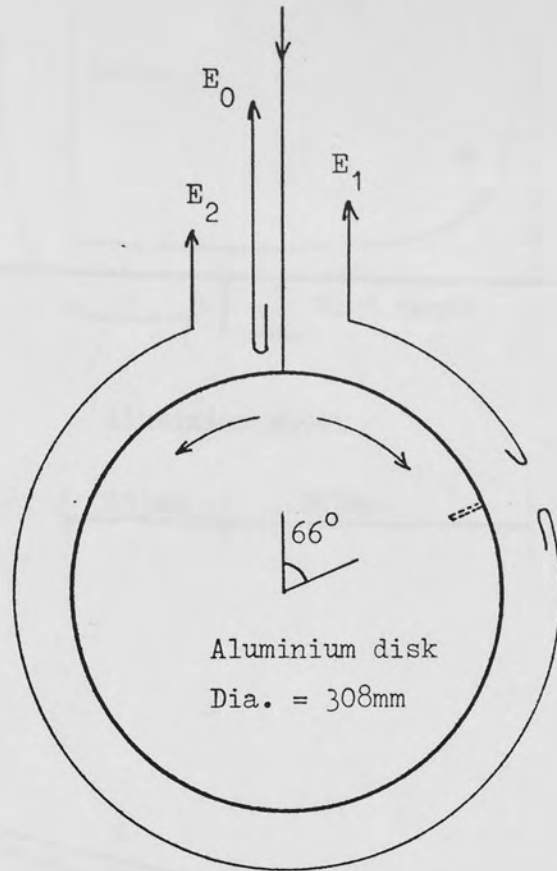Figure 5.1 Cross section of a surface wave probe

Figure 5.2 E_o is the mismatched echo from the drive point.

E_1 and E_2 are the reflected echoes from the defect (a 0.5mm

dia. hole and 1.5mm deep) but surprisingly $E_2 > E_1$.

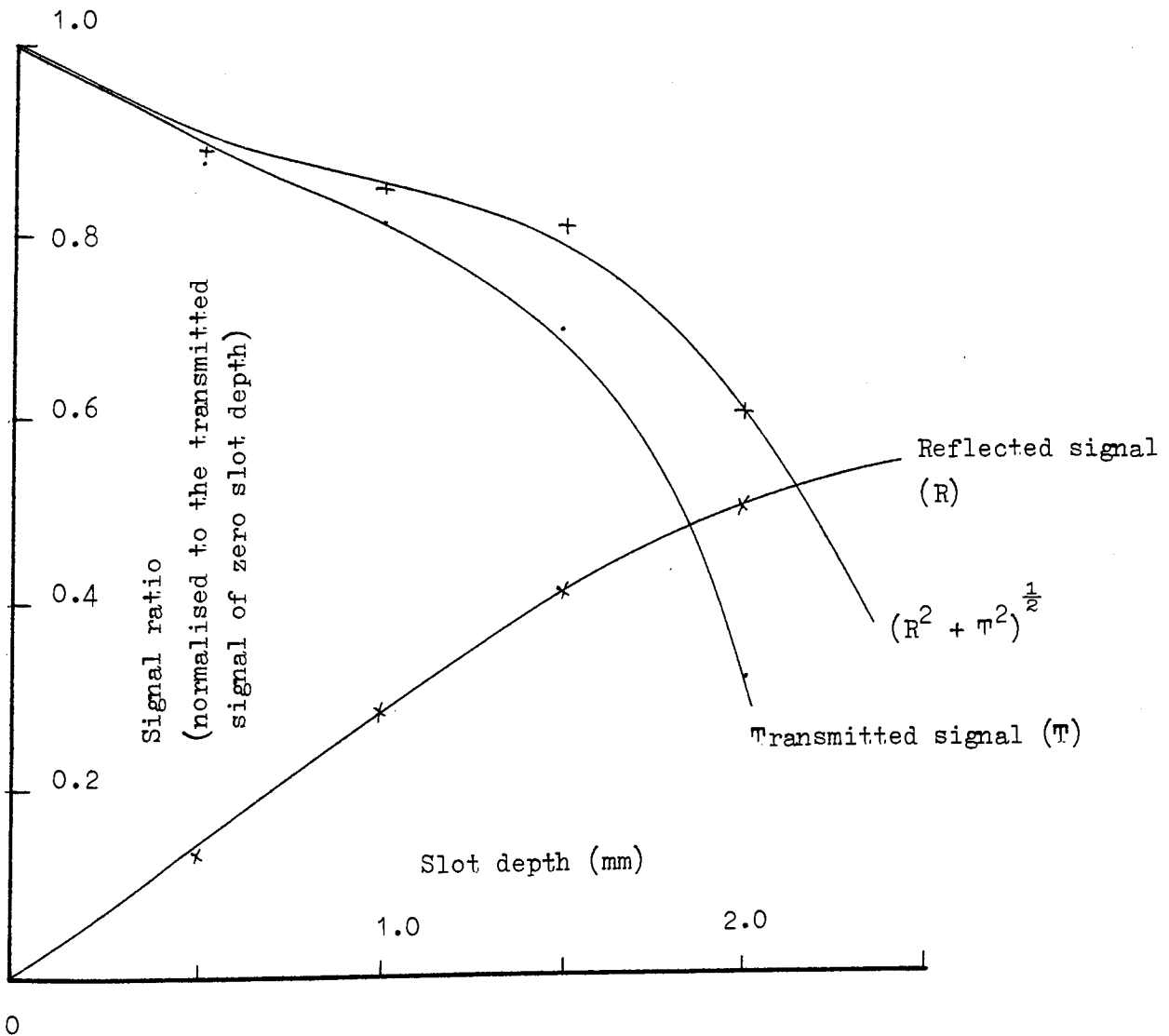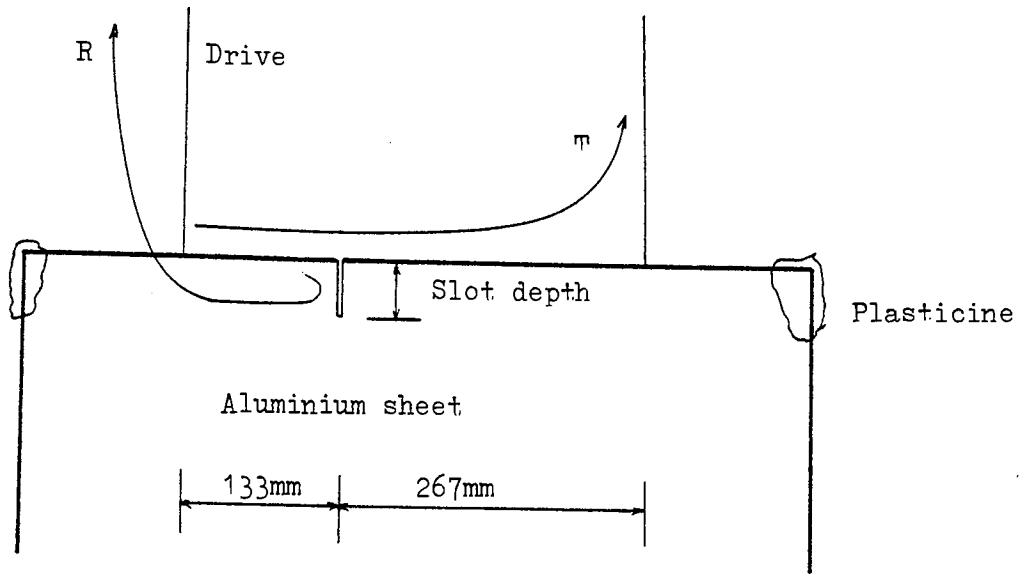E_3 has travelled completely round the circuit.

Figure 5.3 Signal ratio against the slot depth with the experimental arrangement shown above. Mode conversion had taken place on the slot since $(R^2 + T^2)^{\frac{1}{2}} < 1$.
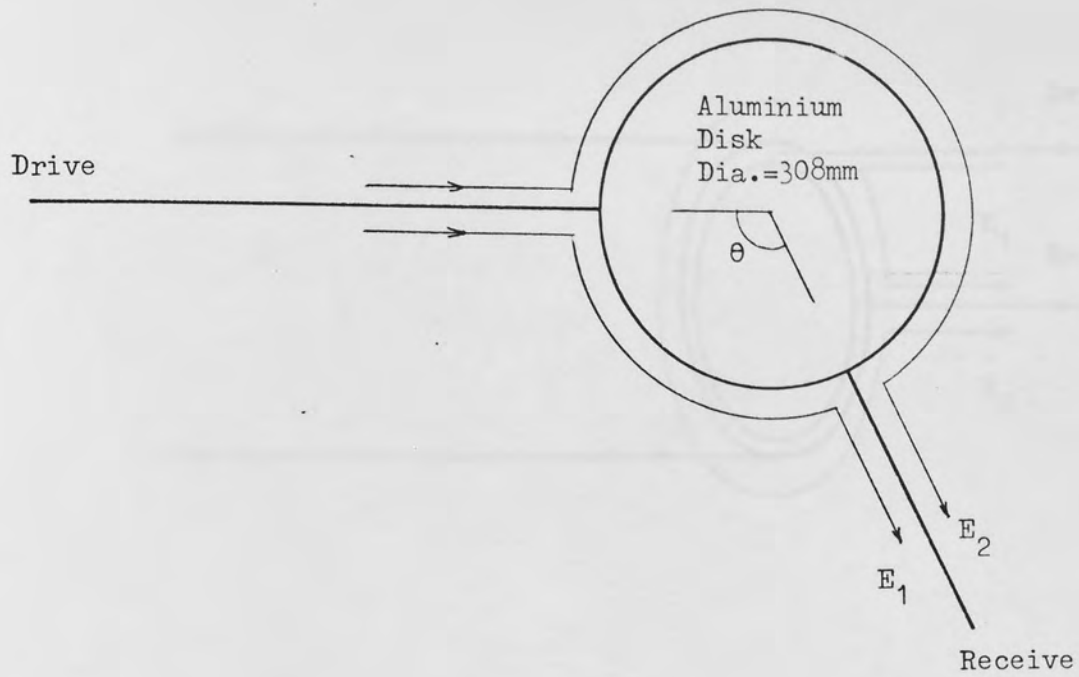
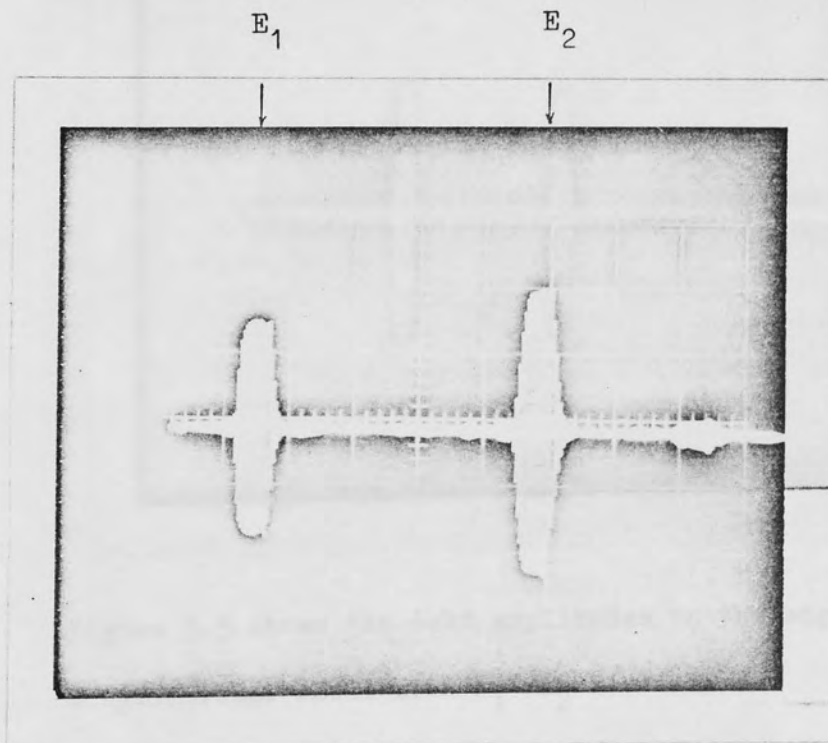Figure 5.4 The arrangement of two wire experiment.

Figure 5.4a shows the anomalous echo amplitudes with

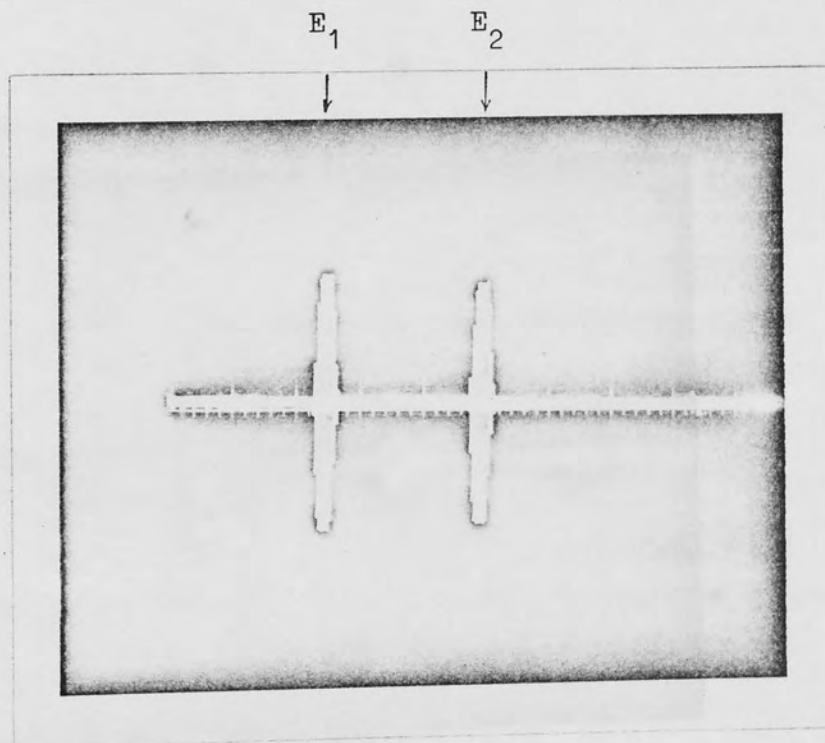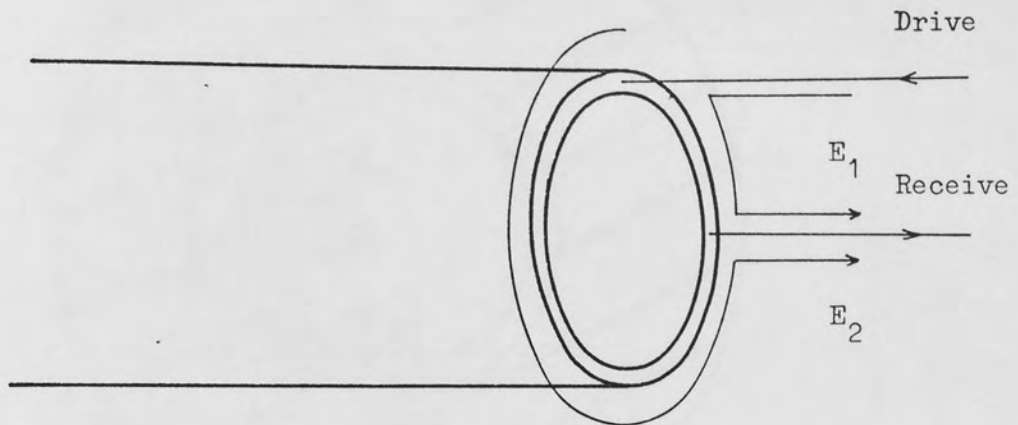$E_2 > E_1$. Frequency = 540 kHz and $\theta = 120^\circ$.

Figure 5.5 shows the echo amplitudes on the edge of a cylindrical shell with $E_1 \simeq E_2$.
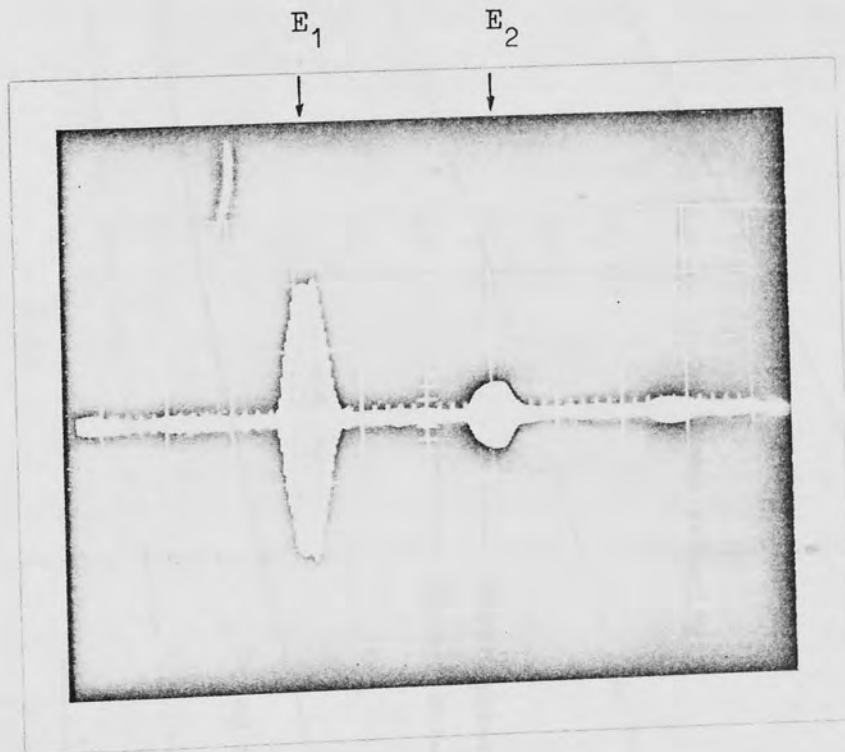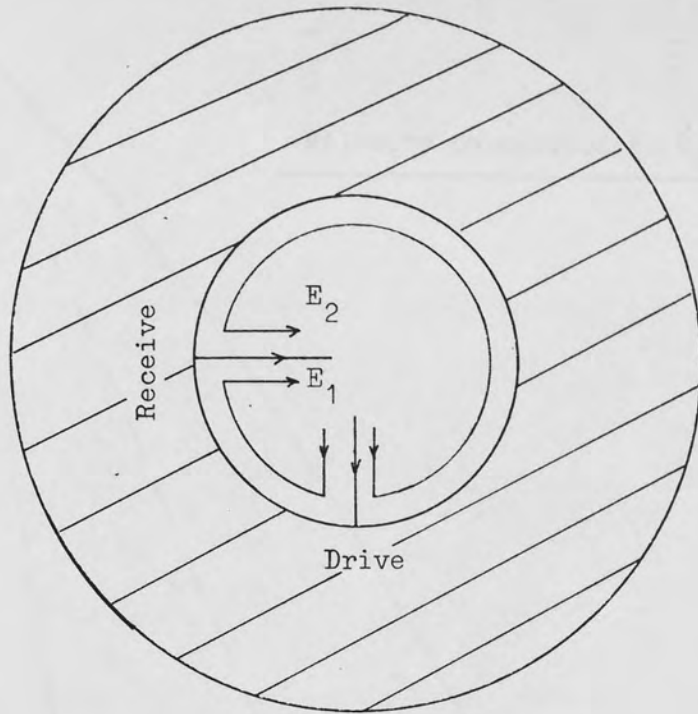
Figure 5.6 shows the echo amplitudes on a 152.4mm diameter hole with E_2 E_1 . The echo (E_2) travelling a longer distance is heavily attenuated. Frequency = 500kHz and $\theta = 135^{\circ}$. The two mode phenomenon is no longer apparent.
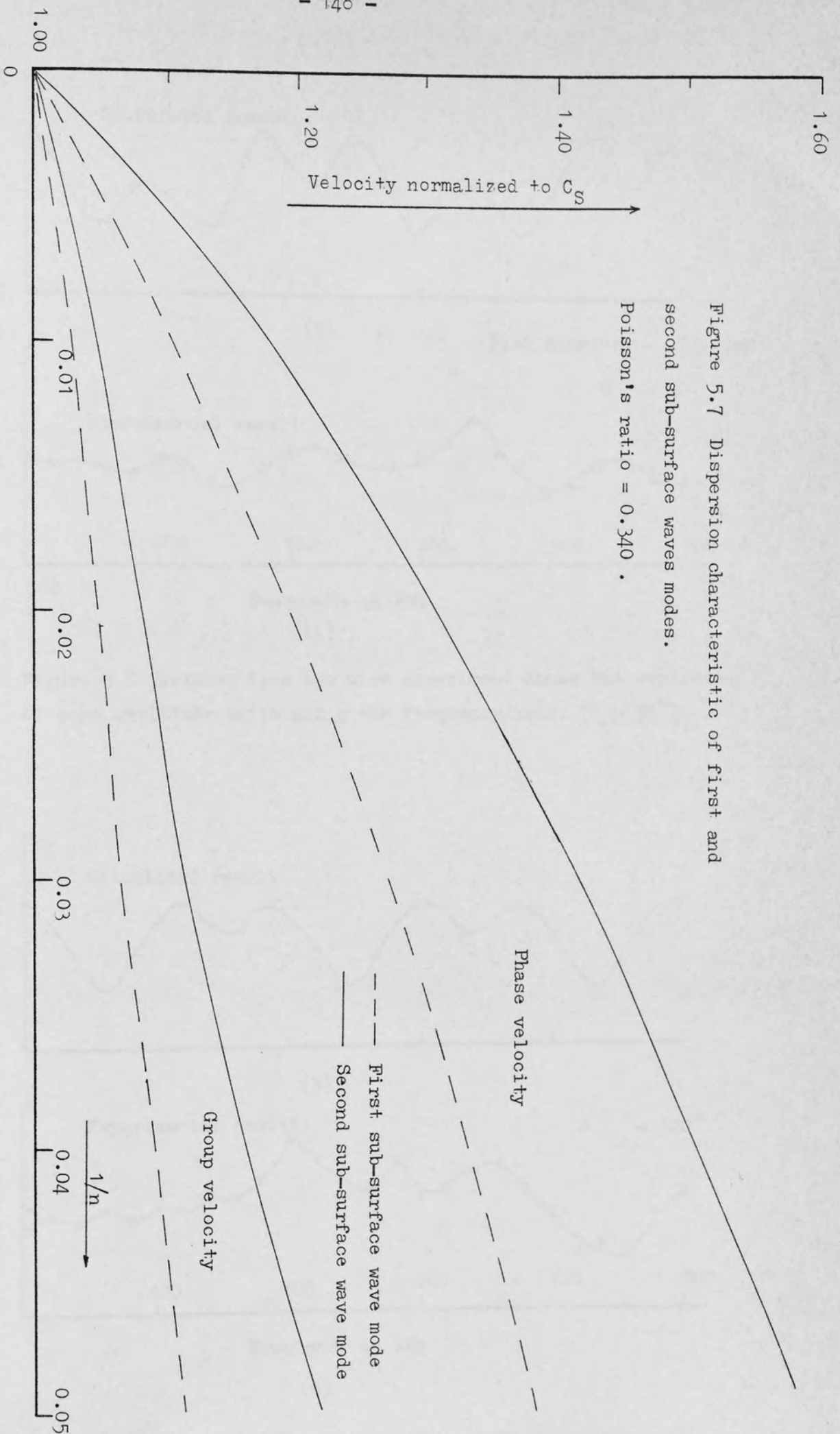
Figure 5.7 Dispersion characteristic of first and second sub-surface waves modes.

Poisson's ratio = 0.340 .
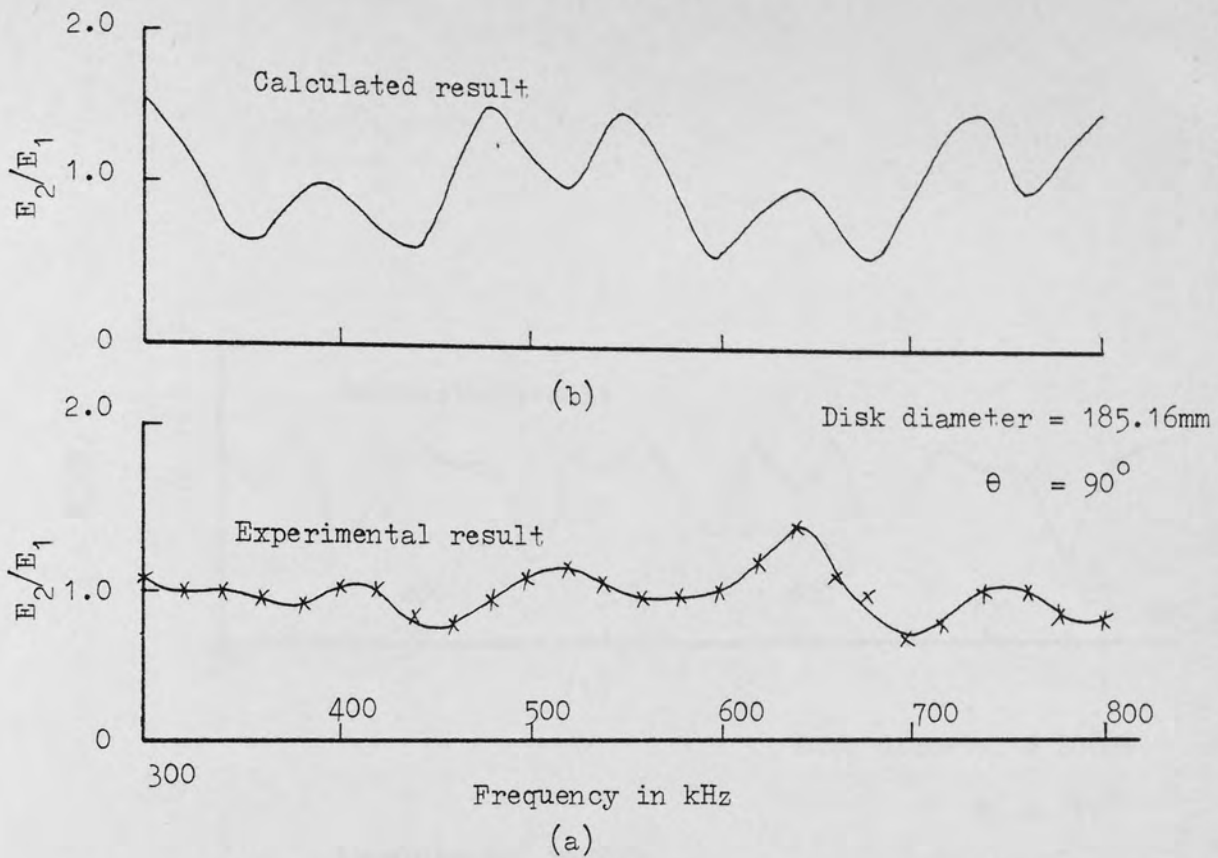
Figure 5.8 Results from two wire experiment shows the variation of echo amplitude ratio along the frequency axis. (θ = 90°)
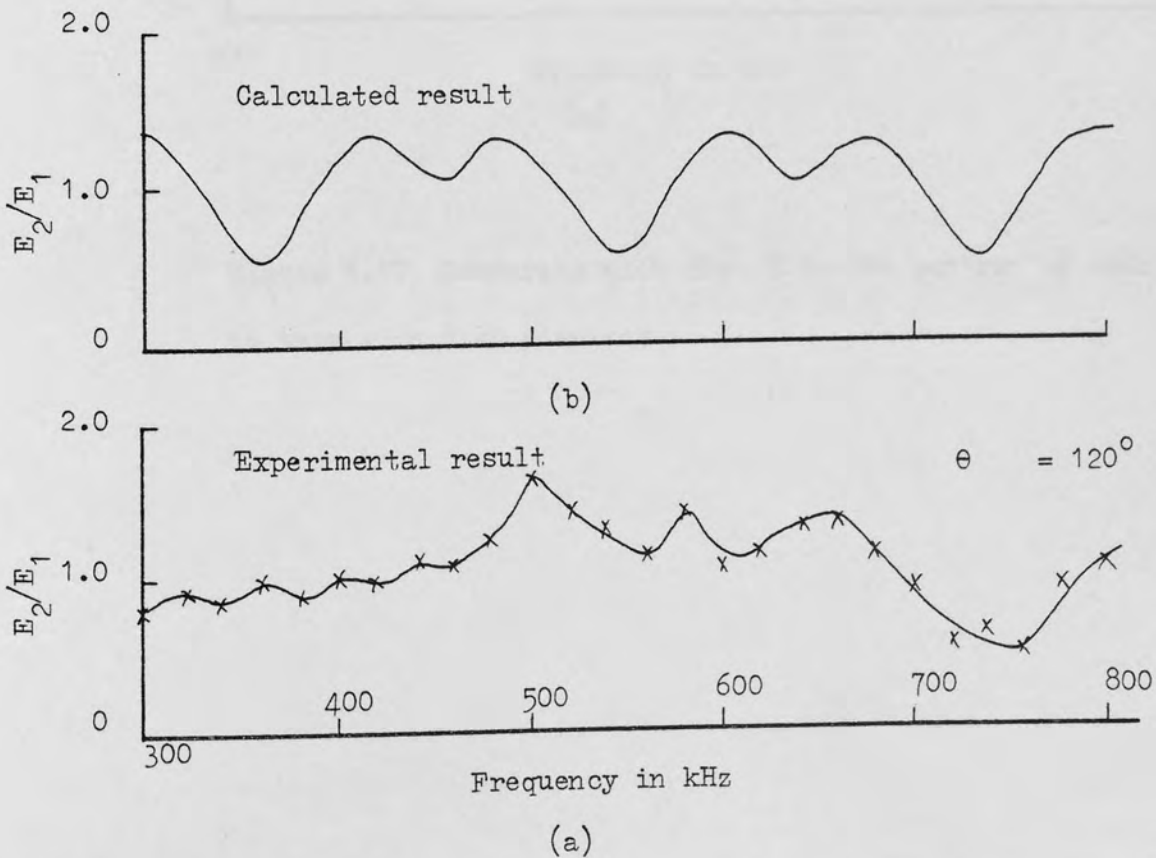

Figure 5.9 This shows the corresponding results for θ = 120°.
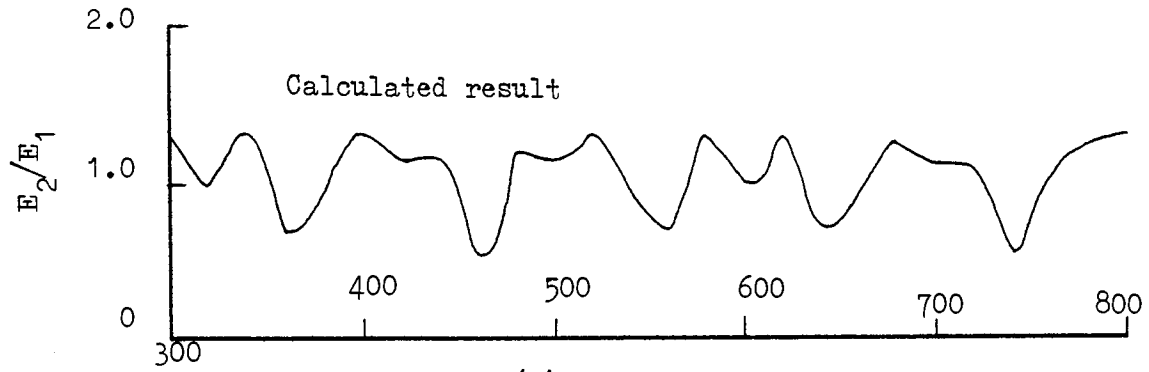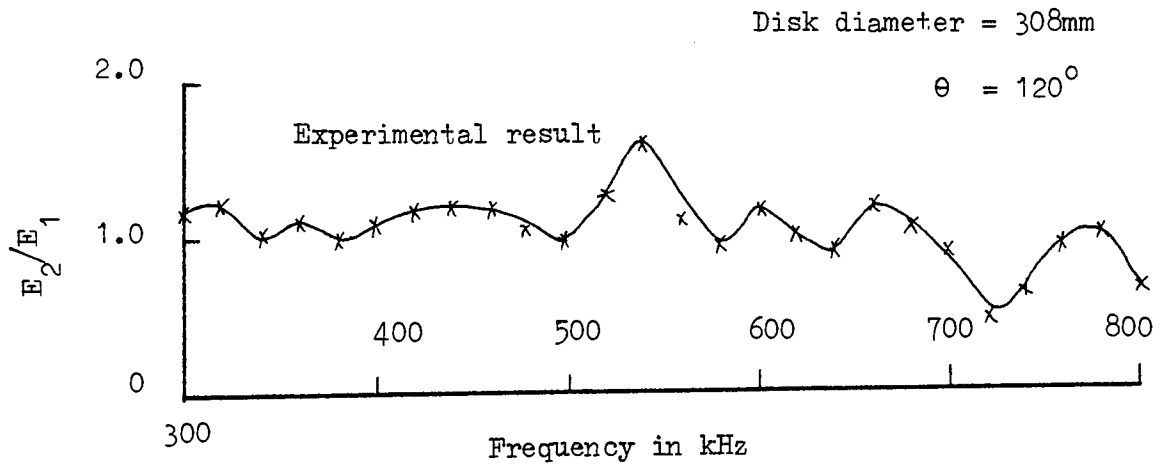
Figure 5.10 Comparing with fig. 5.9, the pattern is seen to vary with disk diameter.

n	$\frac{\Omega_1}{n}$	$\frac{d\Omega_1}{dn}$	$\frac{\Omega_2}{n}$	$\frac{d\Omega_2}{dn}$	$\frac{\Omega_3}{n}$	$\frac{d\Omega_3}{dn}$
20	0.99482	0.93037	1.38175	1.12010	1.58715	1.22618
30	0.97196	0.92500	1.28303	1.07470	1.44102	1.12781
40	0.95991	0.92313	1.22847	1.05861	1.35748	1.09735
50	0.95243	0.92216	1.19350	1.04998	1.30355	1.08195
60	0.94733	0.92153	1.16897	1.04274	1.26563	1.07327
80	0.94081	0.92104	1.13652	1.03595	1.21538	1.05951
100	0.93681	—	1.11576	—	1.18319	—

Table 5.1 Phase and group velocities of first normal Rayleigh
mode, first and second sub-surface waves modes as a function
of 'n' .

(Ω/n = ratio of phase velocity to the shear and

   $\frac{d\Omega}{dn}$ = ratio of group velocity to the shear.)

CHAPTER 6

ELASTIC CONSTANT MEASUREMENTS AT HIGH TEMPERATURE

CHAPTER 6

ELASTIC CONSTANT MEASUREMENTS AT HIGH TEMPERATURE

6.1 Introduction

The elasticities and internal energy loss of solids are
of great importance in engineering as they are necessary as
design parameters. In high temperature applications such as
rocket motors the refractory throat materials tungsten,
graphite composites and refractory oxides and nitrides are
bonded to a cooled former. A full stress analysis requires
knowledge of the various elastic constants over the working
temperature range. Measurements on small quantity of
materials can be used for quality control and in the
development of improved materials.

Where possible, the resonance method described in Chapter
2 has been used. This requires the losses to be small
giving at Q of, say 20. In practice, a higher loss than this
would probably mean that the material was beyond its useful
temperature limit. A wide choice of resonators and modes of
vibration is available. Typically rods in longitudinal and
torsional vibrational modes give Young's modulus and the
shear respectively. Young's modulus and Poisson's ratio are
usually used in engineering design as the latter varies only
slightly with temperature. Thin disks are particularly
suitable for high temperatures as the spectrum at once gives
both elastic moduli. Other modes such as end and shear

resonance in strips have been investigated but are not practicable at high temperature. The wire drive has the advantage that the transducer will separate from the resonator. The echo observation enables the frequency and internal friction to be measured concurrently. This gives useful NDT information.

For very high internal friction, resonance methods cannot be used and the velocity is best determined by the Sing-round[40] or Double-Pulse Superposition[41][42] methods. The pulse attenuation method[43] gives the internal friction.

In the furnace arrangement, the resonator is situated into the bottom of a furnace tube and heated by convection. The Argon or Helium gas was flowing into the bottom at a slow rate; a chromel-alumel or platinum thermocouple is located near the resonator for temperature measurement. Alternatively, the transducer and the resonator are situated into the vacuum furnace tube. Only the transducer section of the line need be of magnetostrictive material and situated inside the low temperature section and the rest of the line is integral with the resonator so the high temperature joint is removed.

6.2 Various Driving Techniques

The degree of coupling to a particular resonance depends
on the resonator parameters, line impedance and the direction
of vibration at the point of drive. Four drive techniques
have been developed, these are shown in Fig. 6.1.

In the first, thin disks and plates can be driven into
a wide variety of modes both in plane and flexural. The
coupling is most efficient when the drive is at an antinode.
In the second, axial drive excites longitudinal modes in
rods and strips. Torsional mode in rods can also be exicted
if the wire is polarized circumferentially and in the third,
a tangential drive excites torsional waves in rods and disks.
A 45° drive to the width end of a strip excites the end
resonances[44] strongly. The use of a double wire is rather
cumbersome but by using "push-pull" or "push-push" can excite
modes selectively. The phase relationships are determined by
adjusting the position of the coil to make the line lengths
either equal for in phase (push-push) or different by $\frac{\lambda}{2}$ for
anti-phase (push-pull). For both ends of line driving
tangentially at opposite ends of a rod, the torsional mode is
more efficiently excited than the simple tangential wire.

Amongst the four drive techniques, the normal and axial
drives are frequently used at high temperature measurements.

6.3 Rods and Strips

The rods sustain longitudinal vibration. For the diameter is very small compared to wavelength, the governing modulus is E and simply

$$E = (\frac{f_n}{n})^2 4L^2 \rho \qquad (6.1)$$

where   L   : the length of the rod

ρ : the density

f_n : resonant frequency of mode order n.

As $\frac{\lambda}{a}$ decreases, the resonant frequency of a given mode decreases. Lord Rayleigh[44] introduced the transverse dilatational correction which is given as:

$$E = (\frac{f_n}{n})^2 4L^2 \rho [1 + \frac{\pi^2 \sigma^2 a^2}{2L^2} + \frac{\pi^4 \sigma^4 a^4}{16L^4}] \qquad (6.2)$$

This is only valid for a large value of $\frac{\lambda}{a}$.

A more rigorous mathematical analysis is the use of the Pochhammer[45] and Chree[46] equation, many authors have studied the problem. The numerical reslults obtained by Bancroft[47] has proved to be accurate to large values of $\frac{\lambda}{a}$ and are used in the rod application. He presented the results in the form of a table giving the value of $\frac{C_{ph}}{C_o}$ against two variables $\frac{\lambda}{a}$ and σ where C_{ph} is the phase longitudinal wave vleocity derived from the experiments. Using the Bancroft correction (B_c),

$$E = \left(\frac{f}{nB_c}\right)^2 4L^2 \rho \tag{6.3}$$

and

$$C_o = \frac{f}{B_c} \frac{2L}{n} \tag{6.4}$$

This is much more accurate than the Rayleigh equation.

When the vibration spectrum is known, a curve fitting procedure may be used to determine the Poisson's ratio. The ratio of $\frac{f}{nB_c}$ is a constant with 'n' if σ is postulated correctly. This also provides a check on the degree of isotropy and constancy of elastic constant over a wide frequency range. Materials were selected with this feature in mind.

In experiments, a rod of poco graphite, a very fine grained material recently developed by National Bureau of Standards was measured. Only the rod sample was available. A curve fitting procedure on the longitudinal vibration spectrum yields a Poisson's ratio of 0.25 which is high compared to ordinary graphite. The ratio of $\frac{f}{nB_c}$ with n for $\sigma = 0.25$ remains constant with a standard deviation of 0.07% only. Fig. 6.2 shows the result and the constancy demonstrates the high isotropy of poco graphite. To compare the relative isotropy, several nominally isotropic rods of known Poisson's ratio have been measured over a wide frequency range. The deviation of $\frac{f}{nB_c}$ value with mode n for aluminium, brass, silicon nitride and poco graphite rods are shown in Fig. 6.3. The fluctuation from the reference line (0%) representing a

perfectly isotropic material gives useful information on
non-destructive material evaluation (NDE). From Fig. 6.3,
the silicon nitride is relatively more isotropic than other
specimens but the constancy of elastic behaviour of poco
graphite is comparable to the highly isotropic material,
aluminium.

Fig. 6.4 shows the high temperature measurement on the
poco graphite rod. The internal friction up to 1000°C was
not apparent. Like the ordinary graphite, it exhibited a
minimum velocity at about 200°C and then increased with the
temperature. When velocity and expansion data are available,
Fig. 6.5 shows the result on a four axis logarithmic graph[48],
this gives comprehensive data display.

A hot pressed silicon nitride rod was also measured.
Fig. 6.6 shows the result with temperatures up to 800°C. A
very high bar velocity ($\simeq 10,000$ m/sec) was experienced
indicating a very high elasticity material (31.767×10^{10} n-m^2).
The temperature coefficient was only 17.1 p.p.m/Kelvin.

An analytical solution has not been found for the free
rectangular strips while the solution does exist for the
cylindrical solution. But an exact solution on end resonances
of strips had been obtained. In end resonances, the energy
of vibration is confined to a region near the boundary which
has a similar characteristic to the surface waves. They are
first explained by Folk[49] and Mindlin[50] and associated
with cut-off modes in an isotropic plate which have complex

wave numbers and occurred in conjugate pair. The precise eigenvalues (Ω_e) of end resonances on strips have been obtained by Bell and Karlmarczie[44] and they can be represented by a quadratic equation as shown in equation (6.5).

$$\Omega_e = 1.9860 + 0.899\sigma + 0.31\sigma^2 \qquad (6.5)$$

where $\Omega_e = \dfrac{\omega_e b}{C_S}$

and ω_e = angular end resonant frequency

2b = width of strips.

A 90° drive to the width end of strips excites the end resonance mode and the plate wave mode (with one nodal line along the length) efficiently. If the ratio of length to width is greater than 10, the latter mode essentially propagates at plate velocity (C_p)[51] with wavelength of 4b. By comparing the frequencies of end resonance (f_e) and the plate wave (f_p), the Poisson's ratio of a rectangular strip can be determined experimentally. Table 6.1 gives the results of (f_p/f_e) against Poisson's ratio which are also shown graphically in Fig. 6.7.

Several strips of known Poisson's ratio have been measured and Table 6.2 shows the experimental results for strips of brass, aluminium, steel and nuclear graphite. The results are consistent to the known values and accurate better than 3% which is the limit arising from variation in material properties and experimental errors.

6.4 Disk Resonators

For a circular disk, the theoretical analysis for extensional and flexural vibrations are well established. They are, in effect, the corresponding in-plane and the Chladni's plate[52] vibration. For elasticity measurements, only the low order modes need to be considered.

For disks vibrating in out of plane flexural modes, the classical theory of Poisson and Kirchoff[53] is valid only for a disk with a very small thickness to diameter ratio. A more rigorous differential equation has been derived including the influence of shear and rotary inertia by Ufyand[54] and Mindlin[55]. Martincek[56] has made use of flexural vibration to determine the Poisson's ratio of a disk, but no report of its use are known because it requires different arrangements to excite a pair of flexural resonances and not preferable in temperature measurement. The flexural mode vibration has more applications in mechanical filters[57][58] rather than the elasticity measurement.

For in-plane vibration of a disk, the frequency equation was derived by Love[12]. Onoe[9] and Holland[10] have completed the theoretical analysis of the low order resonant spectrum. The frequency equations of distortion, radial and tangential modes were shown in equation (4.1), (2.23a) and (2.23b) respectively. The distortion modes are governed by shear modulus, the radial mode is more dependent on Young's modulus. This is understandable as the area change in the

former group is small, while in the latter it is large.
Fig. 6.8 shows the first four mode patterns. A single radial
drive will efficiently excite the distortion and the radial
modes. A frequency ratio of the pure radial mode ($f_{1,R}$) and
three nodal diameters ($f_{1,3}$), $f_{2,1}$ and $f_{1,5}$, $f_{2,R}$ and $f_{1,9}$ gives
Poisson's ratio with good sensitivity. The Poisson's ratio for
the value of the above frequency ratio concerned, can be read
from the nomogram shown in Fig. 6.9. The plate velocity is
obtainable from one of the mode frequencies. The frequency
ratio is not sensitive to the thickness, Ambati[59] has shown
the correction for thickness as, in virtually all modes,
unnecessary for diameter to thickness ratio greater than 10.
The only dimension to be measured is the diameter which can
be machined with high precision.

Hot pressed silicon nitride is typical of the materials
investigated. They are used on the structures of gas turbines,[60]
because of their high resistance to corrosion and stable
thermophysical properties. Three disks of 38.1mm diameter
from same batch were measured. The disk was fixed radially to
a 0.7mm nickel line with a high temperature adhesive
'Autostick'. Readings of $f_{1,R}$ and $f_{1,3}$ and thermocouple mV were
taken. A least-square curve fitting is necessary to smooth
out the raw data. The Poisson's ratio then can be calculated
from frequency $f_{1,R}/f_{1,3}$ at selected intervals of
temperature. The internal friction at high temperature (1000°C)
to the limit of the experiment was very low. Fig. 6.10 shows
the variation of Poisson's ratio from three disks against
temperature. All disks show very similar characteristics,

a fall in Poisson's ratio which is the reverse of most metals. There was a conspicuous difference in Poisson's ratio and velocity even from the same batch which suggests that the measurements could be very sensitive to the degree of nitriding.

The refractory material silica is of great interest. A disk of 50mm diameter was fused to a 1mm silica tube about 600mm long. The tube was then joined to a magnetostrictive line of diameter giving a good acoustic match. The disk was then located in the hot region of a furnace. The silica tube being in the region of the temperature gradient thus kept the magnetostrictive joint at room temperature . The $f_{1,3}$ and $f_{1,R}$ were measured as the disk temperature was slowly cycled. Fig. 6.11 shows the variation of Poisson's ratio and the plate velocity with temperature. Unlike the silicon nitride, the Poisson's ratio increases with the temperature but most surprisingly the velocity increases with the temperature and reaches a maximum as the melting point approaches.

A variety of graphites including isotatically pressed, extruded, pyrolytic (the orthotropic form) and carbon fibre and carbon-fibre-carbon composites are potentially useable in the throat of rocket motors, high power internal combustion engines and nuclear reactors. Stress analysis of these structures over the operational temperature range is necessary and the data obtained in these measurements along with other thermophysical data enable this to be carried out. Figures

6.12 and 6.13 show the change of elasticity and Poisson's ratio with temperature on materials which were made from powdered coke, extruded with a tar binder and then graphitised. The variation in Poisson's ratio with temperature is consistently small but there is a wide difference between specimens. The large difference in Poisson's ratio for graphite can have a large effect on manufacturing.

The annealling has significant effect on elastic constants of most metals. A test was carried out on an aluminium disk. The disk is spot butt welded to a 0.7mm line. On the initial run, the readings of $f_{2,1}$ and $f_{1,5}$ for temperature up to $600^{\circ}C$ were measured. The disk was allowed to cool down at ambient temperatures. A second run was then carried out by similar procedure. Figure 6.14 shows the change in Poisson's ratio of the temperature on the initial and second runs. The change in Poisson's ratio in the two runs is very large. Initially, a rise in Poisson's ratio to 0.42 at temperature $500^{\circ}C$ was noted and this suddenly fell to 0.38 as the temperature was further increased. The second run generally has a similar temperature coefficient but the peaking is removed by the first annealling run. An appreciable change in internal friction at high temperature was observed, the variation on loss (Q_m^{-1}) has been shown previously in Fig. 2.33. The disk was cycled a number of times and the results showed very similar characteristic to that of the second run.

The work has extended to investigate the disk of simple
anisotropy empirically. Moderate anisotropy occurs in rolled
metal where the maximum and minimum elasticities are
perpendicular. It is evident only at the lowest mode, that
with two nodal diameters, the elasticity removes the mode
degeneracy and the mode splits. In one, the nodal diameters
are symmetrical about the elastic axis and in the other they
are aligned. As the wire drive has maximum coupling at an
antinode, placing the drive at an elastic axis excites only
the symmetrical modes. As it is moved to the 45 degree
position, the second mode appears. An arbitrary 's' plane
model may be used to resolve the resonant frequencies, the
separation of frequencies was as large as 4% for rolled
aluminium disk. This is an indication on the degree of
anisotropy. Annealling has been found effective in weakening
the mode degeneracy and the separation on frequencies
becomes smaller.

6.5 Conclusion

The pulse-echo technique developed can be used to examine the spectrum of a large number of solid structures. An important application is the characterisation of materials in which elasticity and Poisson's ratio can be measured over a wide range of temperature. The technique has been extended to identify anisotropy on materials.

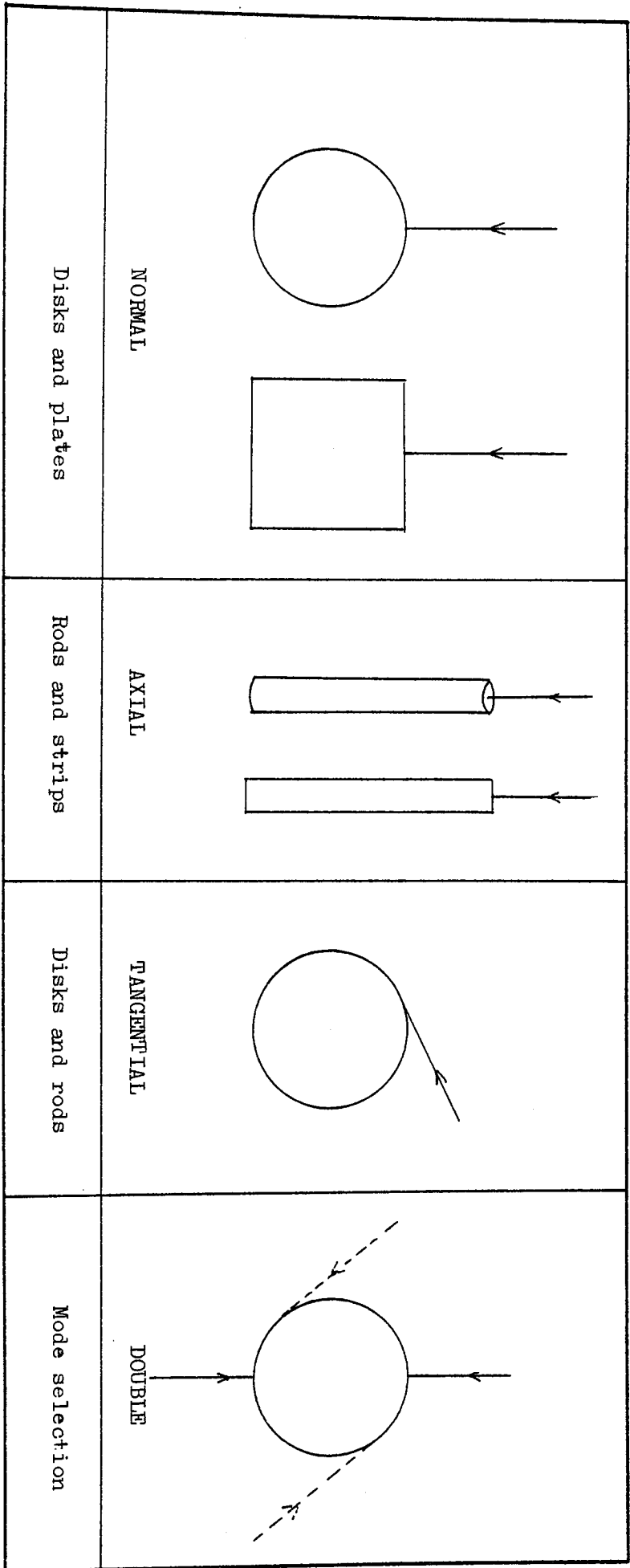| Disks and plates	Rods and strips	Disks and rods	Mode selection
NORMAL	AXIAL	TANGENTIAL	DOUBLE

Figure 6.1 Wire drive techniques. The drives were selected either to maximize

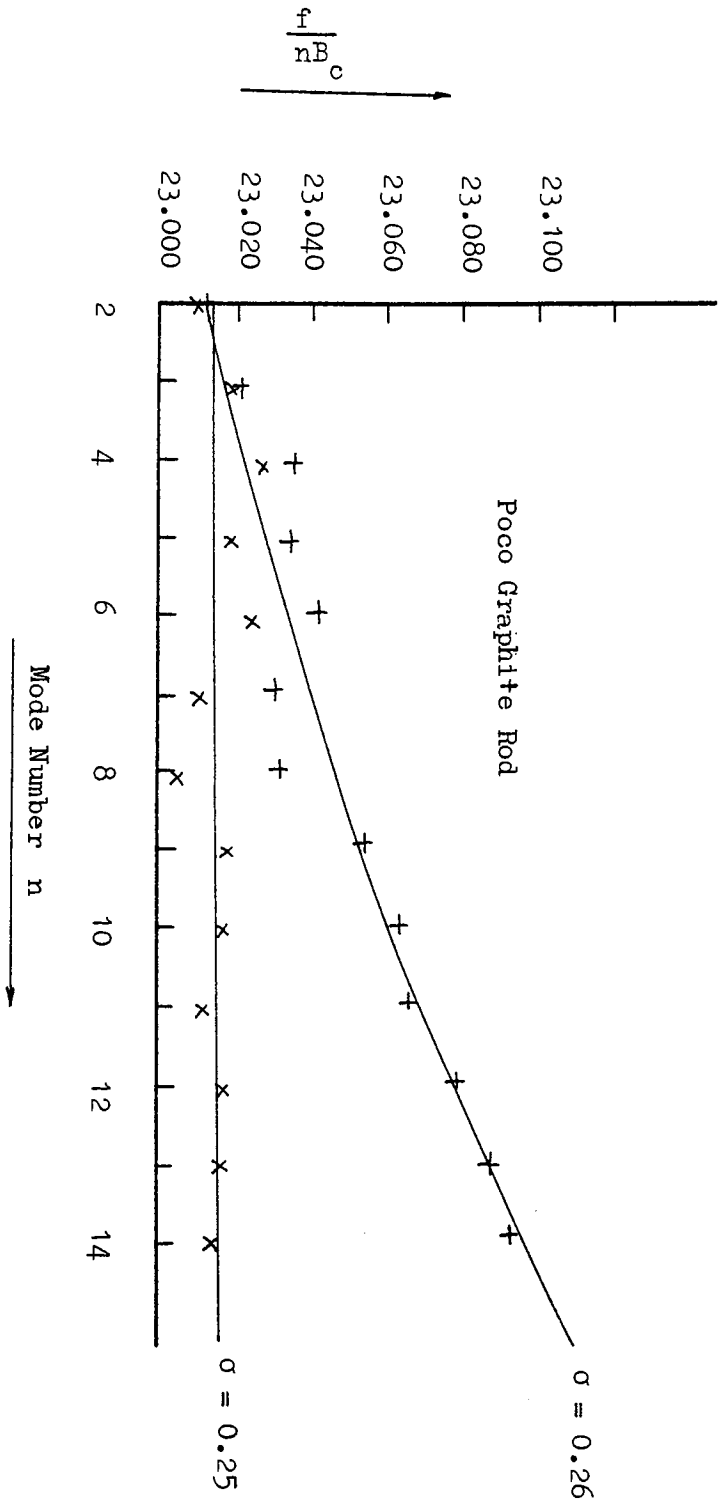the coupling or to select a particular mode.

Figure 6.2 shows the variations in $\frac{f}{nB_c}$ against the mode number n
using two different Poisson's ratio values. It is apparent that
$\sigma = 0.25$ is the better postulated value for poco graphite.

% Shift →

-0.02   -0.01   0.00   0.01   0.02

Poisson's Ratio

- – – – Silicon Nitride   0.264
- —— Aluminium   0.345
- – – Poco Graphite   0.250
- —— Brass   0.350

Mode Number n →

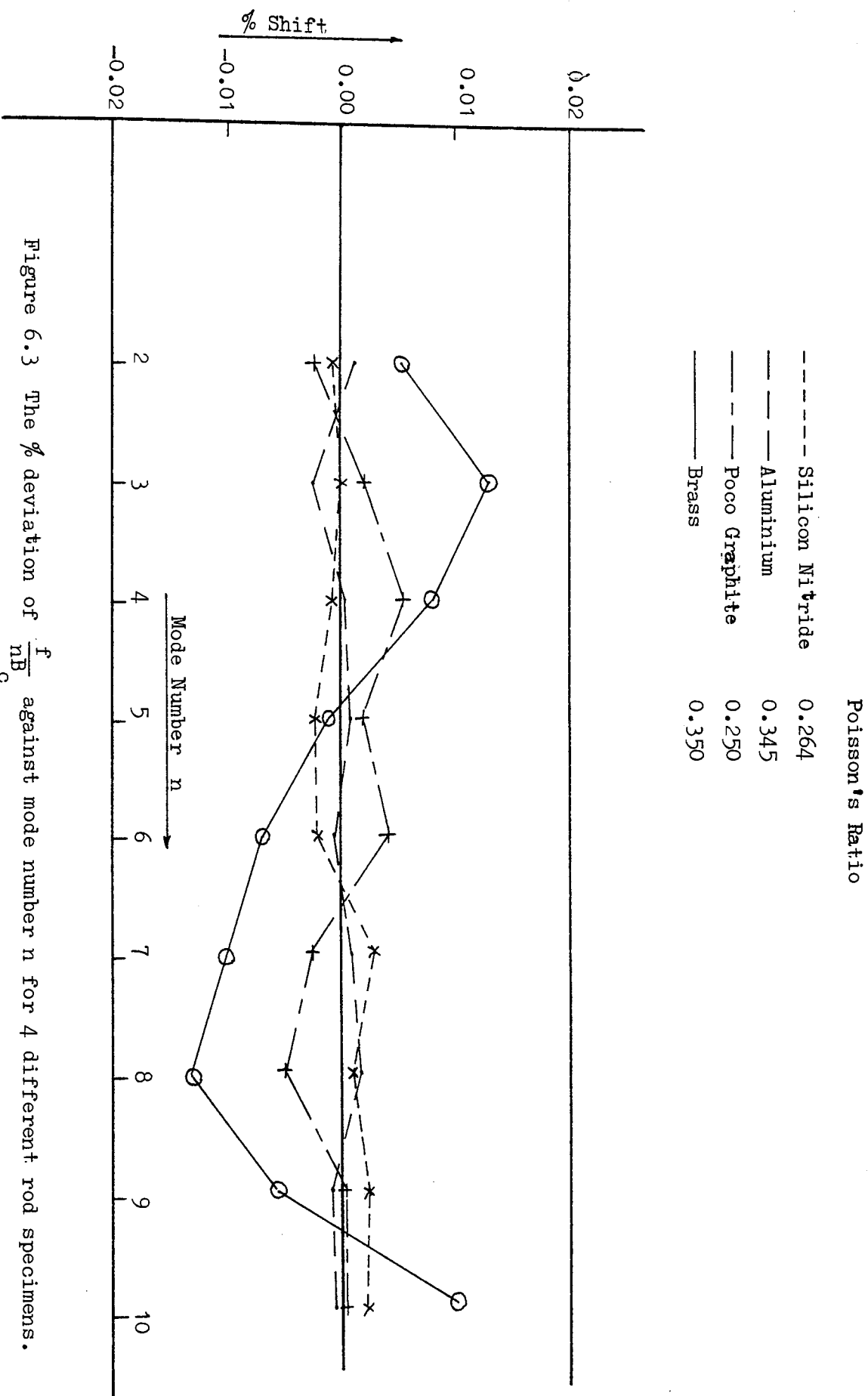2   3   4   5   6   7   8   9   10

Figure 6.3 The % deviation of $\frac{f}{nB_c}$ against mode number n for 4 different rod specimens. This provides a check on the constancy of the elastic behaviour and the degree of isotropy of the specimens.
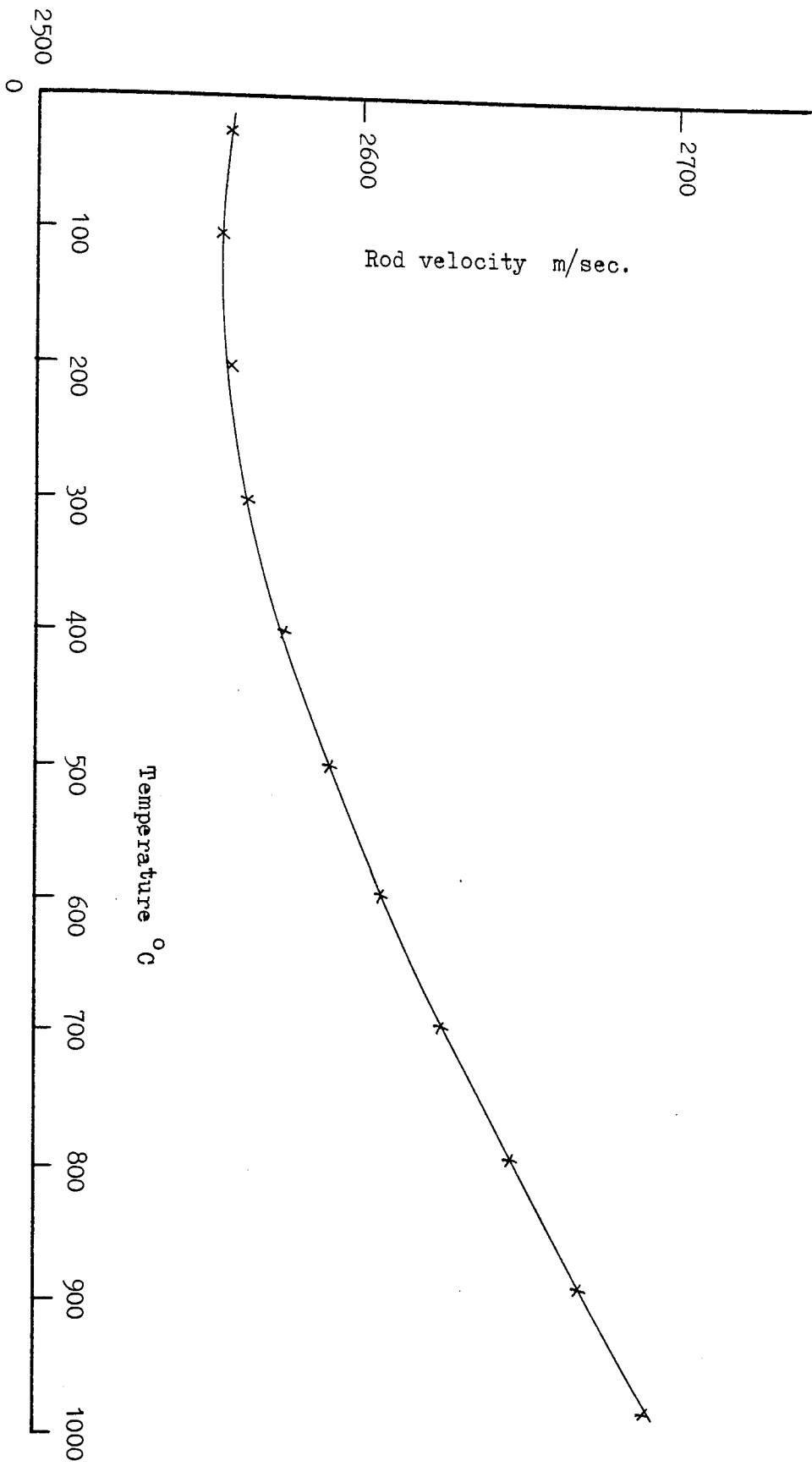
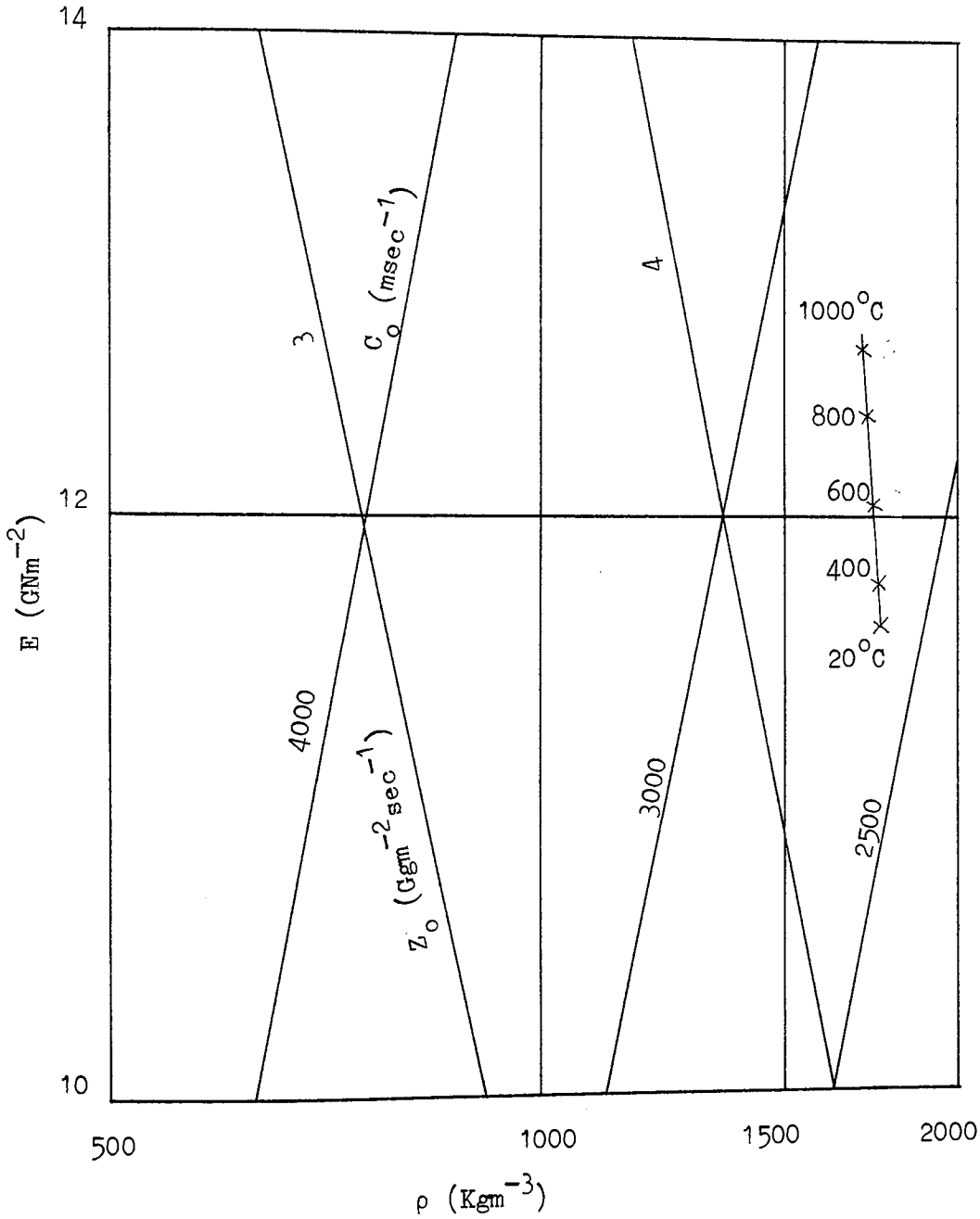Figure 6.4 Resultant curve from temperature run on poco graphite.
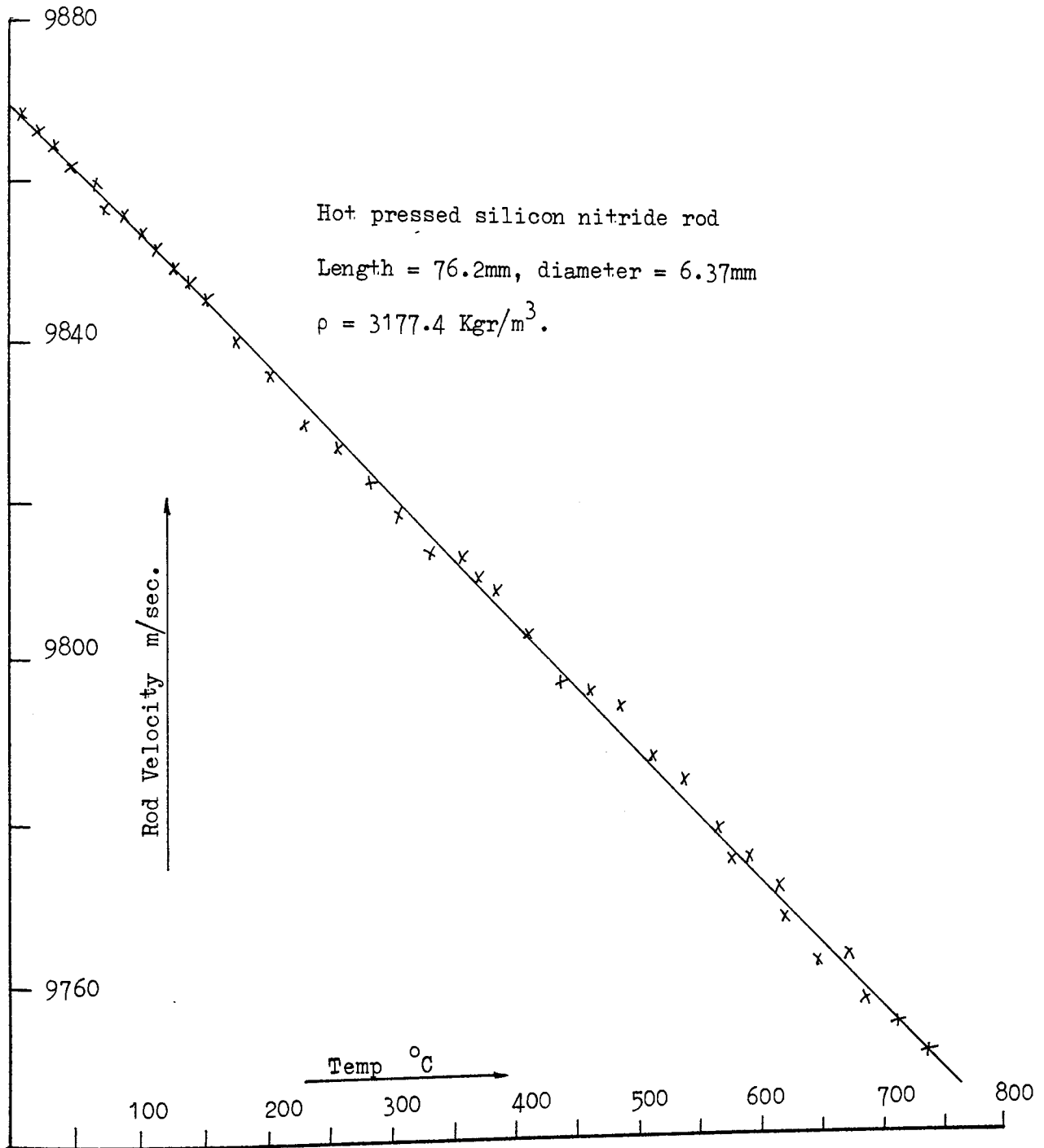
Figure 6.5 shows the comprehensive temperature run data on poco graphite. The bar velocity (C_o), Young's modulus $(E=\rho C_o^2)$ and the characteristic impedance $(Z_o=\rho C_o)$ are displayed on one graph only.

Figure 6.6   Data on hot pressed silicon nitride. The temperature coefficient is only 17.1 p.p.m/k, this indicates this material has a very stable thermophysical properties at high temperatures.
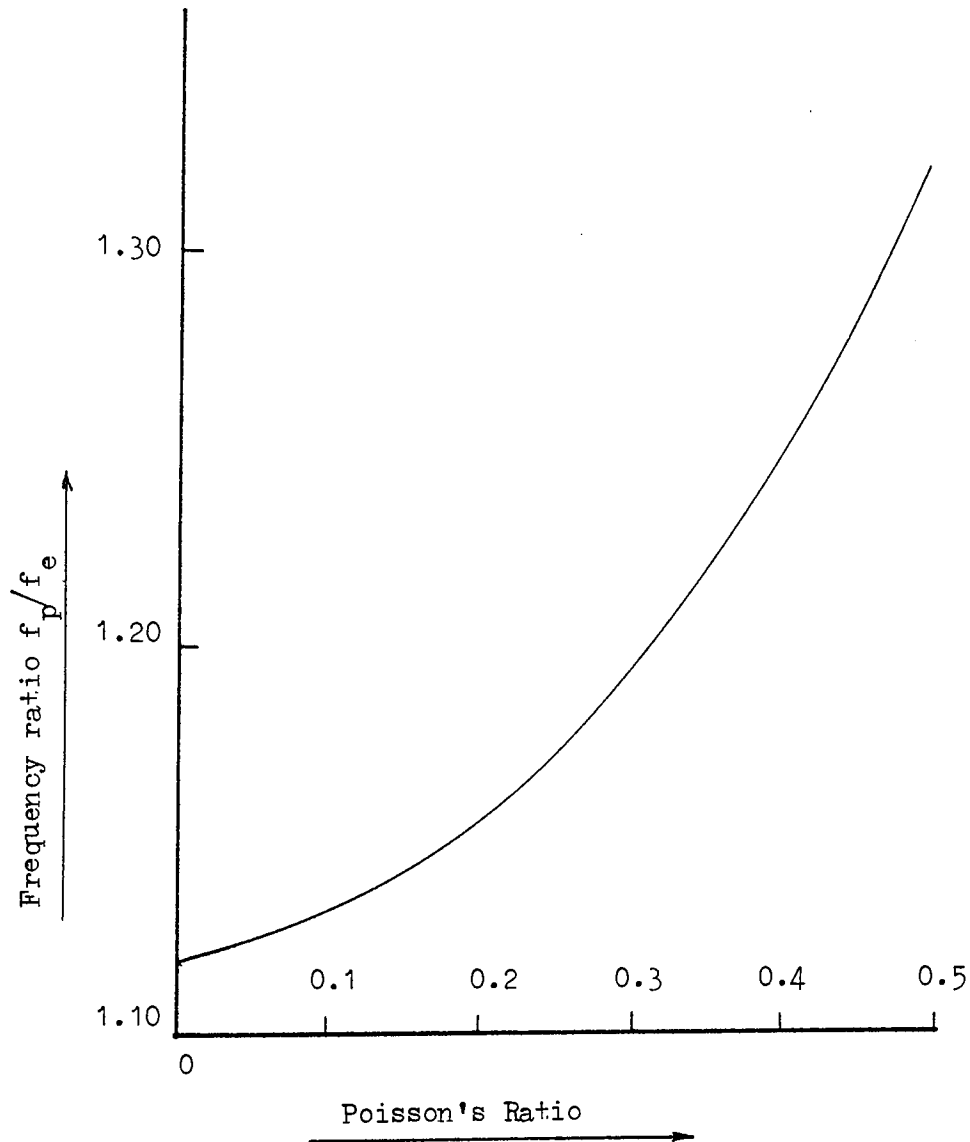
Figure 6.7 shows the sensitivity of f_p/f_e against Poisson's ratio.

A measure of sensitivity is $\dfrac{f_e}{f_p} \dfrac{d(f_p/f_e)}{d\sigma}$. Using this expression,

the sensitivities are 0.1 and 0.5 for $\sigma = 0.05$ and 0.35 respectively.

The sensitivity is good enough for most metals.
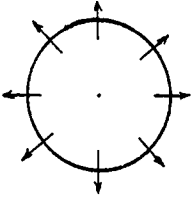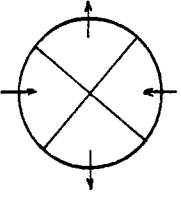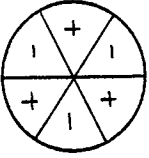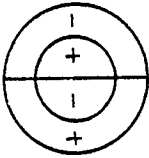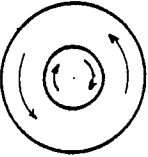
DIAMETERS	Ø	2	3	1	FIRST SHEAR MODE
CIRCLES	1	1	1	2	
SYMBOLS	1,R	1,2	1,3	2,1	
NODAL PATTERN					

Figure 6.8 Nomenclature of the principle modes used. The first shear mode has an antinode (maximum rotation) at the centre. All the others have central nodes which are classified as circles.

$\dfrac{f_{1R}}{f_{13}}$ σ

0.70   0.75   0.80   0.85   0.90   0.95   1.00   1.05

-0.10   -0.05   0.00   0.05   0.10   0.15   0.20   0.25   0.30   0.35   0.40

$\dfrac{f_{21}}{f_{15}}$

0.90   0.95   1.00   1.05   1.10

-0.10   -0.05   0.00   0.05   0.10   0.15   0.20   0.25   0.30   0.35   0.40 σ

$\dfrac{f_{2R}}{f_{19}}$

0.80   0.85   0.90   0.95   1.00

-0.10   -0.05   0.00   0.05   0.10   0.15   0.20   0.25   0.30   0.35   0.40 σ
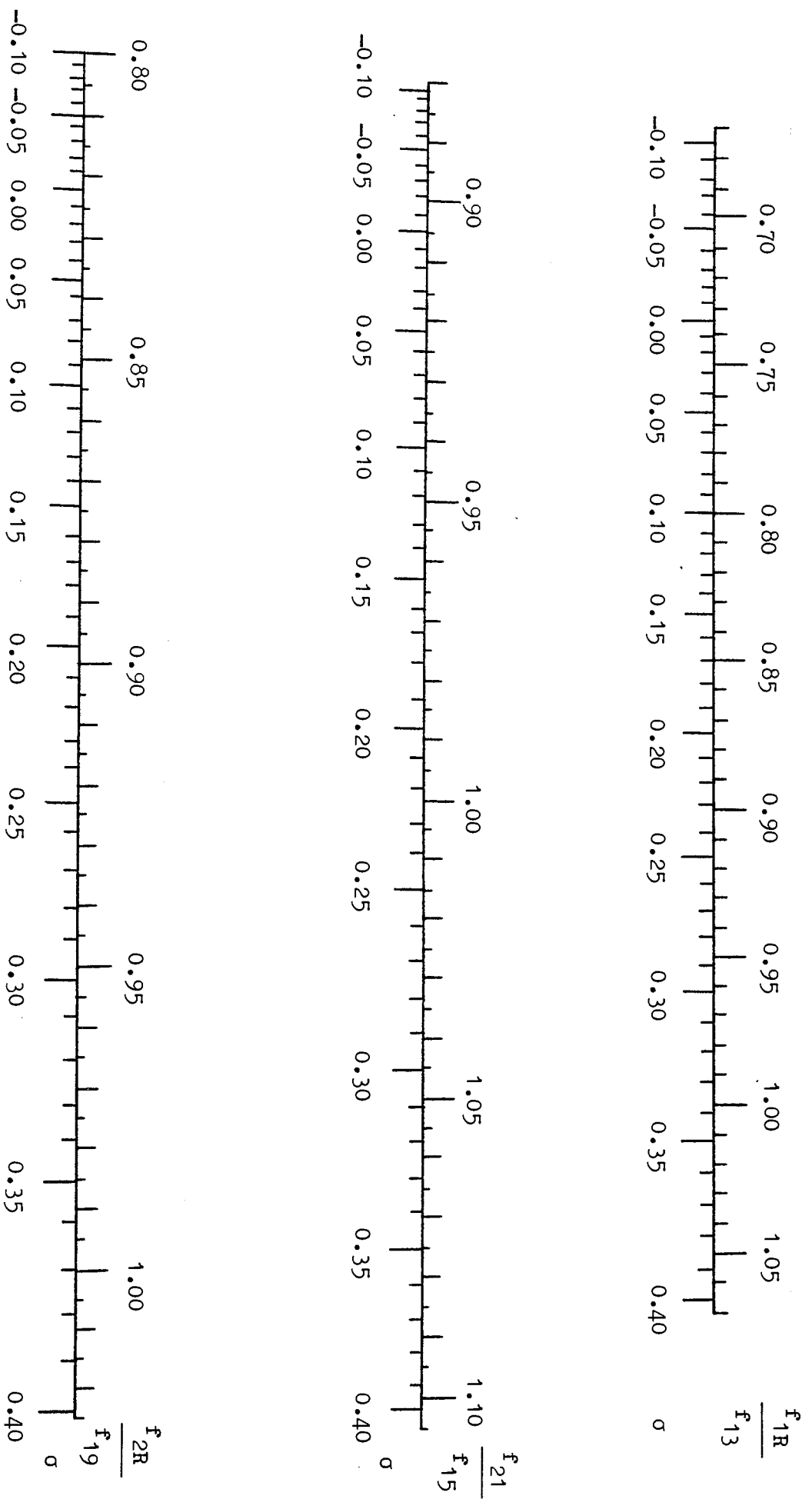
Figure 6.9   Nomogram giving Poisson's ratio in terms of the frequency ratio. The sensitivities

for $\dfrac{f_{1R}}{f_{13}}$, $\dfrac{f_{21}}{f_{15}}$ and $\dfrac{f_{2R}}{f_{19}}$ respectively are 1.0, 0.6 and 0.65 for $\sigma = 0.3$.
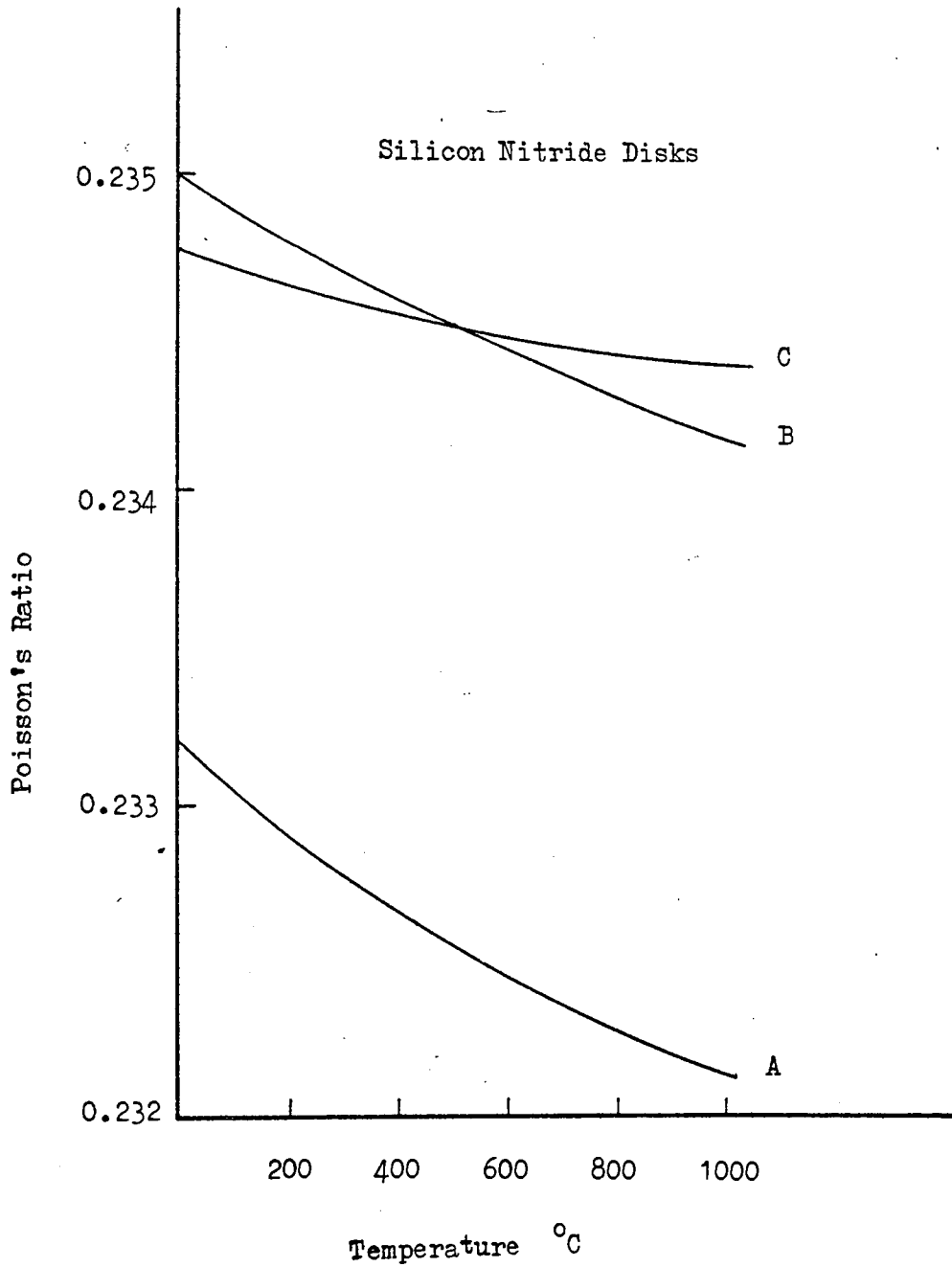
Fig. 6.10   All three disks are from the same batch.
The Poisson's ratios are virtually identical but
the specimen variations exceed the temperature
effect.
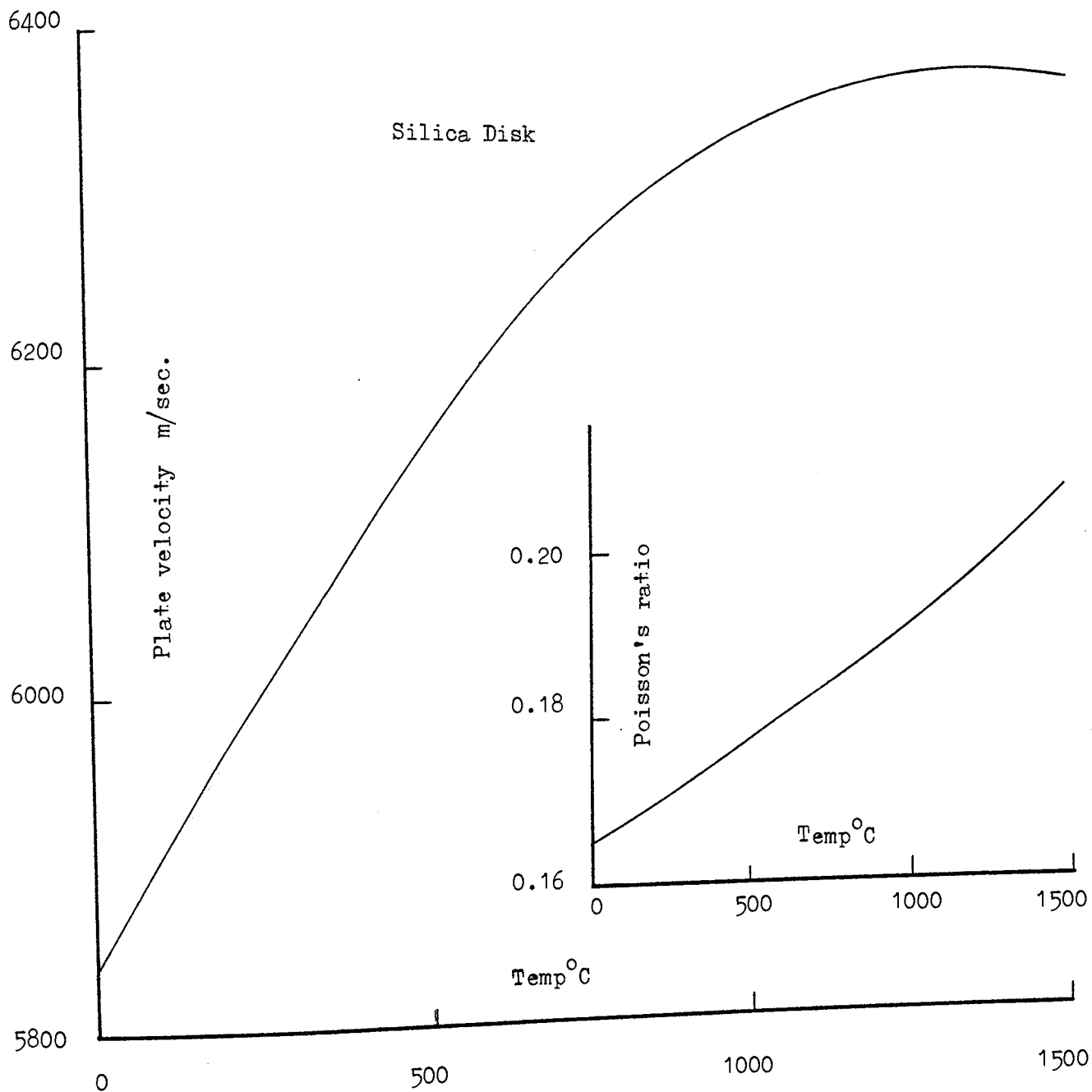
Figure 6.11 Temperature run data on silica. Poisson's ratio increases nearly linearly with temperature. The maximum velocity is reached at the surprisingly high temperature of about 1250°C above which the material begins to soften.
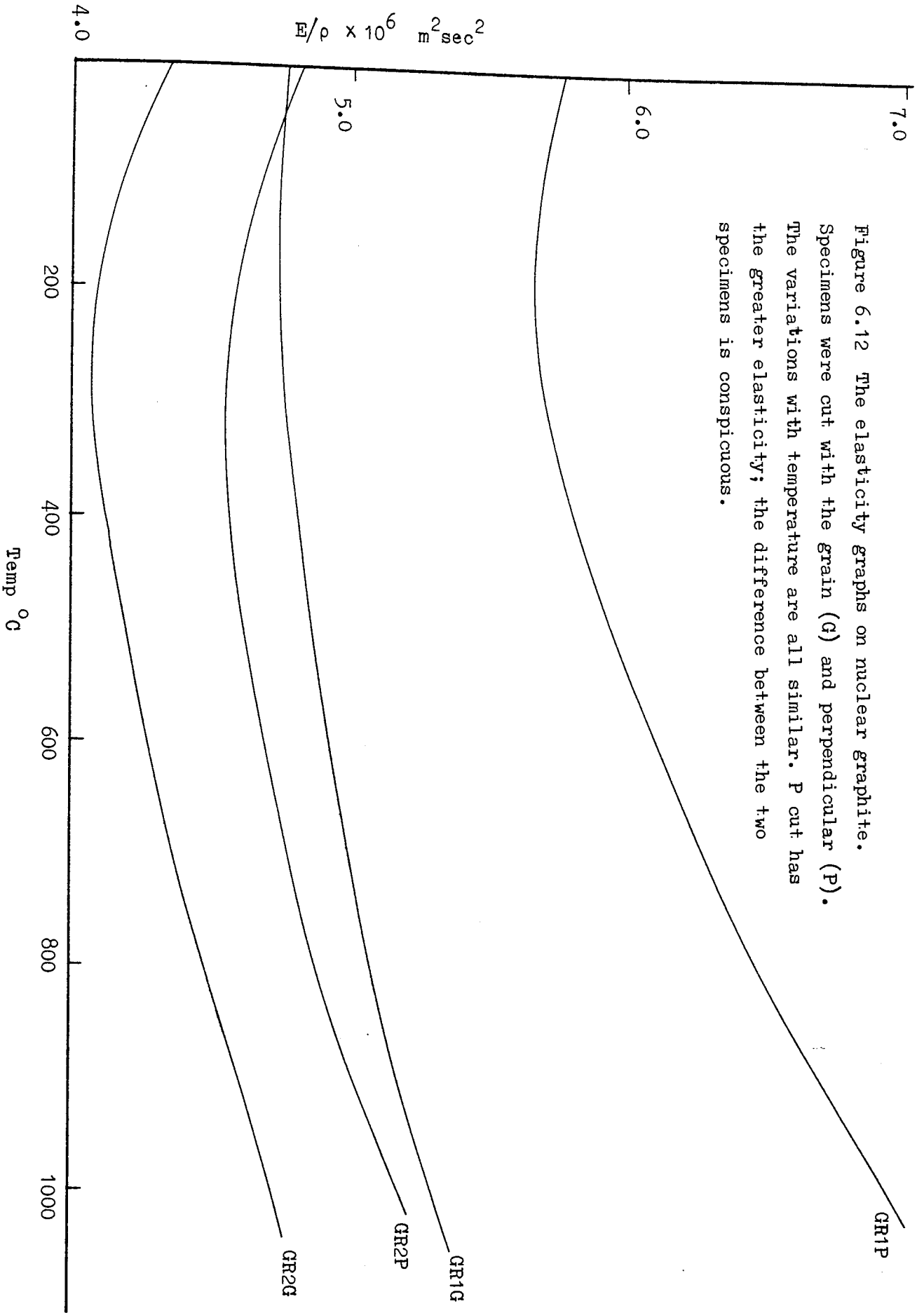
Figure 6.12 The elasticity graphs on nuclear graphite. Specimens were cut with the grain (G) and perpendicular (P). The variations with temperature are all similar. P cut has the greater elasticity; the difference between the two specimens is conspicuous.
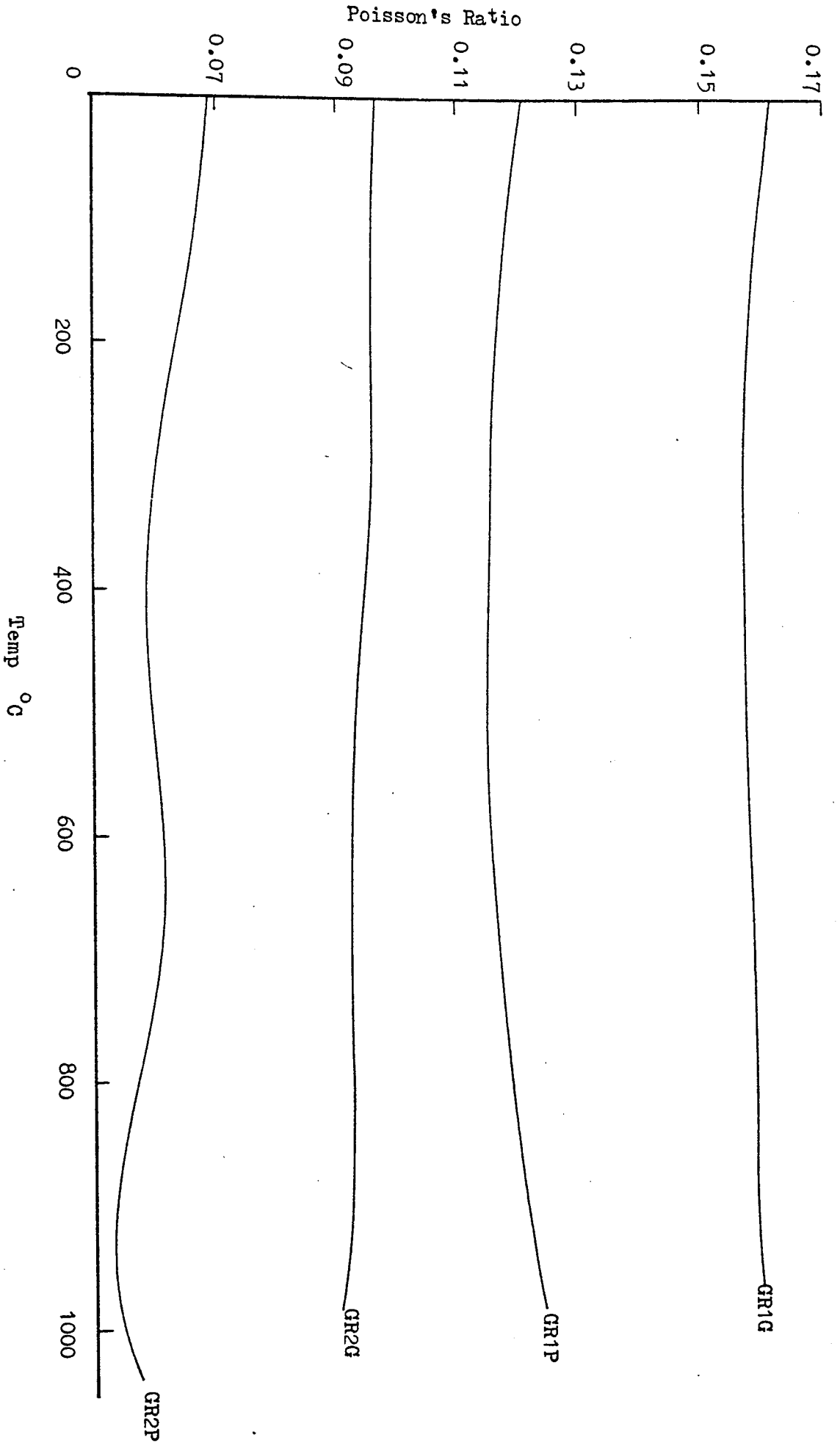
Fig. 6.13 As in fig. 6.12, the graph shows the variation in Poisson's ratio with temperature. P cut specimen has a lower Poisson's ratio.
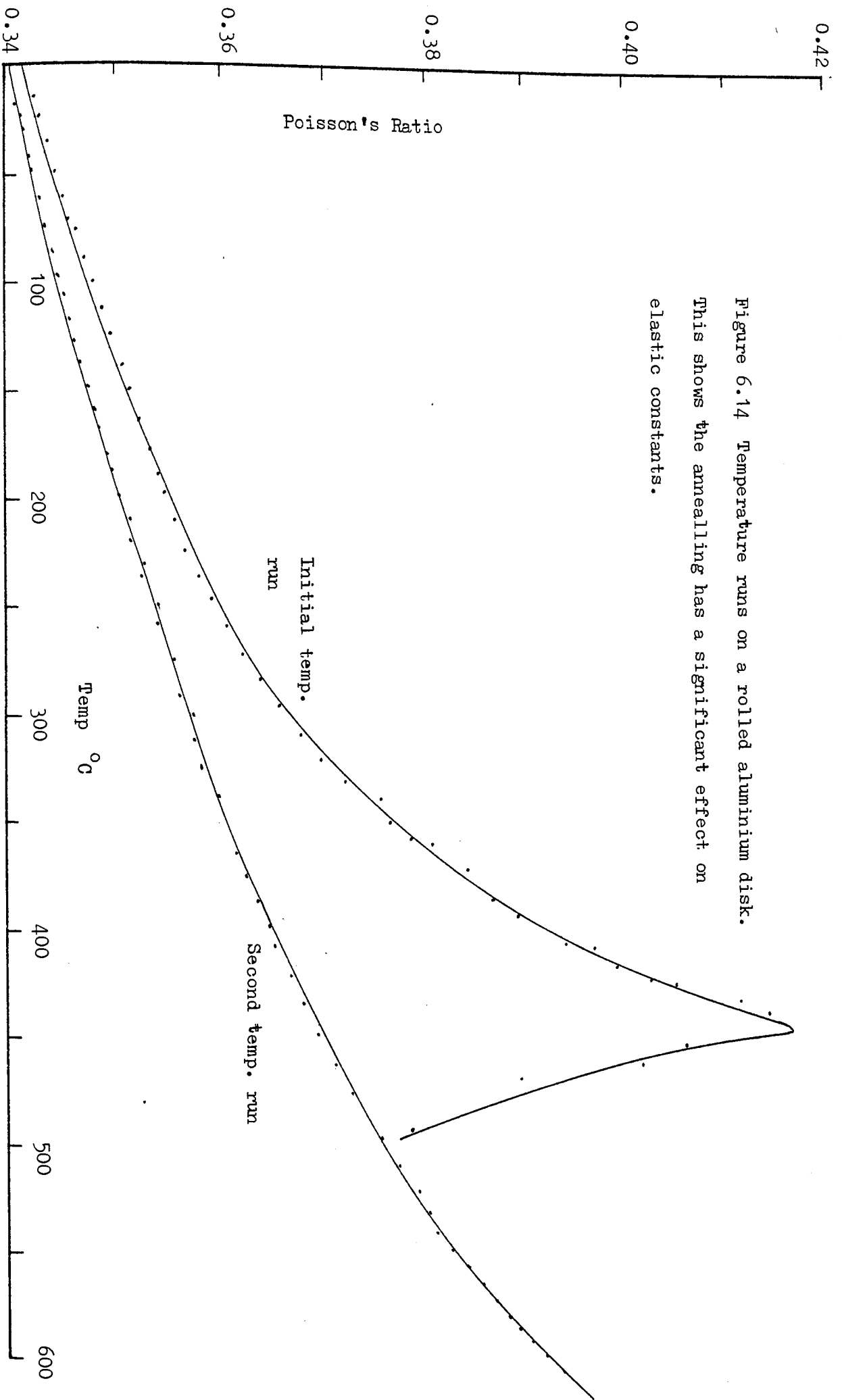
Figure 6.14 Temperature runs on a rolled aluminium disk. This shows the annealling has a significant effect on elastic constants.

Poisson's Ratio	0	0.05	0.10	0.15	0.20	0.25	0.30	0.35	0.40	0.45	0.50
Ω_e	1.9870	2.0302	2.0728	2.1139	2.1534	2.1914	2.2278	2.2627	2.2960	2.3278	2.3580
f_p / f_e	1.1180	1.1226	1.1297	1.1398	1.1533	1.1705	1.1918	1.2177	1.2491	1.2868	1.3323
Ω_e / R_0	2.2735	2.2987	2.3253	2.3522	2.3789	2.4055	2.4316	2.4571	2.4816	2.5057	2.5287

Table 6.1 The ratios of f_p / f_e and Ω_e / R_0 against Poisson's ratio.
The Poisson's ratio of a long strip can be found by measuring two frequencies and the shear velocity can be determined from Ω_e once the Poisson's ratio is known. When normalised to the Rayleigh wave velocity the parameter is much less dependent on Poisson's ratio than the shear normalised values. This indicates that a physical picture of the end resonance is that of standing surface waves.

Materials	Width (mm)	f_e (kHz)	f_p (kHz)	f_p/f_e	Poisson's ratio
Brass	57.5	27.346	33.390	1.2210	0.355
Aluminium	48.0	47.038	56.402	1.1991	0.336
Steel	51.2	45.204	53.487	1.1832	0.280
Nuclear Graphite	25.4	30.820	34.950	1.1337	0.120

Table 6.2 shows the experimentally measured Poisson's ratio on strips. The results are in close agreement with the known values.

LIST OF SYMBOLS

a	:	disk radius
a_{ij}	:	elements of determinant
A_i	:	Airy function
A_o	:	initial echo amplitude
A_∞	:	steady state echo amplitude
b	:	half width of strips
B_c	:	Bancroft correction
C_ϕ	:	phase velocity
C_g	:	group velocity
C_R	:	Rayleigh velocity
C_O	:	rod velocity $= (E/\rho)^{\frac{1}{2}}$
C_P	:	plate velocity $= C_O/(1 - \sigma^2)^{\frac{1}{2}}$
C_S	:	shear velocity $= C_O/(2(1 + \sigma))^{\frac{1}{2}}$
C_B	:	bulk velocity $= \dfrac{(1 - \sigma)^{\frac{1}{2}} C_O}{(1 - 2\sigma)^{\frac{1}{2}}(1 + \sigma)^{\frac{1}{2}}}$
E	:	Young's modulus
g, p	:	depth functions
$H(t)$	:	Heaviside transform
$H_n(x)$	:	Hankel function of first kind
i	:	$(-1)^{\frac{1}{2}}$
$J_n(x)$	:	Bessel function of first kind
$M_n(x)$	:	$x\,\dfrac{J_{n-1}(x)}{J_n(x)}$
M_{eq}	:	edge equivalent mass
M	:	static mass
n	:	mode number
$n_x,\ n_{xm}$	:	number of oscillation to crossover in lossless and lossy resonators respectively

Q_c	:	coupling Q factor
Q_m	:	material Q factor
Q_T	:	total Q factor
r, θ	:	polar co-ordinates
R_i	:	velocity ratio normalised to shear where i=0,1,h,s for straight edge, disk, hole and shell respectively
s	:	Laplace variable
t	:	time
T	:	burst duration
u	:	displacement function
$\dot{x}$	:	$\dfrac{dx}{dt}$
$x'(u)$	:	$\dfrac{dx}{du}$
$x!$	:	factorial x
$Y_n(x)$	:	Bessel function of second kind
z_0	:	characteristic impedance
z_ℓ	:	acoustic line impedance
α	:	relaxation term accounts for material loss
β	:	coupling term for rods
β_d	:	coupling term for disks
ω_s	:	transmitted angular frequency
ω_n	:	resonant angular frequency
ρ	:	density
η^2	:	$2/(1 - \sigma)$
σ	:	Poisson's ratio
σ_1^2	:	$\dfrac{(2 + \sigma)}{24(1 - \sigma)}$
λ	:	wavelength
ε	:	propagation constant $2\pi/\lambda$
e_{ij}	:	strain

σ_{ij} :   plane stress

T_{ij} :   shear stress

ϕ, ψ :   longitudinal and shear potentials respectively

K :   eigenvalues of disk $= \dfrac{\omega a}{C_P}$

Ω_l :   eigenvalues of disk $= \dfrac{\omega a}{C_S}$

Ω_e :   eigenvalues of end resonance on strips $= \dfrac{\omega b}{C_S}$

REFERENCES

1. J. F. W. Bell, "A solid acoustic thermometer", Ultrasonic, 6, 11-14, (1968).

2. J. F. W. Bell and J. C. K. Sharp, "The precision measurement of elastic constants of isotropic solids over wide temperature ranges", Rev. Int. Htes. Temp. et. Refract., 12, 40-43, (1975).

3. J. C. K. Sharp, "A theoretical and experimental investigation into the spectra of selected resonators", Ph.D. Thesis, Department of Elec. and Elect. Eng., University of Aston in Birmingham, (1974).

4. Lord Rayleigh, "Theory of sound", 2nd edition, Vol. 1, 262-265, Dover publication, N.Y., (1945).

5. Sir George Stokes, Camb. Maths. Trans., (1845).

6. H. F. Pollard, "Resonant behaviour of an acoustic transmission line", Aust. J. Physics, 15, 513-526, (1962).

7. J. F. W. Bell, J. Y. F. Chen and K. R. Chaplain, "The elastic constants of refractory materials at high temperatures", the American Soc. for NDT, to be published, (June 1979).

8. R. Holland, "Numerical studies of elastic-disk contour modes lacking axial symmetry", J. Acous. Soc. of America, 1051-1057, (1966).

9. M. Onoe, "Contour vibration of isotropic circular plates", J. Acou. Soc. of America, 28, 1158-62, (1956).

10. Y. L. Luke, "Integrals of Bessel functions", McGraw Hill Book Co., Inc., N.Y. (1962).

11. R. Holland, "Application of Green's functions and eigenmodes in the design of piezoelectric ceramic devices", Ph.D. thesis, Mass. Inst. Tech, (1966).

12. A. E. H. Love, "A treatise on the mathematical theory of elasticity", 497-498, 4th Edition, Camb. Univ. Press., (1927).

13. J. F. W. Bell, and J. M. Pelmore, "An instrument for internal friction measurement", J. App. Phy. E., 10, 1-5, (1977).

14. Lord Rayleigh, "On waves propagated along the plane surfaces of an elastic solid", Proc. London. Math. Soc., 17, 4-11, (1855).

15. R. M. White, "Surface elastic wave", Proc. IEEE, 58, 1238-76, (1970).

16. Ultrasonic Symp. Proc. IEEE, (1972-1977).

17. Surface Wave Abstracts, Multi-Science Publishing Co. Ltd.

18. I. M. Mason, E. A. Ash, P. E. Lagasse, De La Rue and R. M. Schmidt, "Ridge guides for acoustic surface waves", Electronic Letters, 7, 395-397, (1971).

19. A. C. M. Li, H. L. Bertoni, A. A. Oliner and S. Markman, "Propagation characteristic of the pseudo-Rayleigh mode of the ridge guides for SAW", Electronic Letters, 8, No.9, 220-221, (1972).

20. H. Kolsky, "Stress waves in solid", 4-15, Dover publication, (1965).

21. P. M. Morse, and H. Freshbach, "Method for theoretical physics", McGraw Hill, N.Y. (1953).

22. Lord Rayleigh, "On the free vibrations of an infinite plate of homogeneous isotropic elastic matter", Proc. London Math. Soc., 20, 225-234, (1889).

23. H. Lamb, "On waves in an elastic plate", Proc. Roy. Soc. London, Serial A, No. 93, 114, (1971).

24. I. A. Viktorov, "Rayleigh and Lamb waves", Plenium Press, N.Y., (1967).

25. M. Onoe, "Formulae and tables, modified quotients of cylinder functions", Report of Inst. of Ind. Science, Univ. of Tokyo, 32, (1955).

26. E. E. Allen, Math. Tables Aids Comput., 8, 240-241, (1954).

27. G. N. Watson, "Theory of Bessel function", Camb. Press, N.Y., (1962).

28. N. W. MacLachlan, "Bessel functions for engineers", Oxford Press, 59, (1955).

29. A. E. H. Love, "A treatise on mathematical theory of elasticity", Camb. Univ. Press, 4th Edition, 544-545, (1927).

30. D. Ensminger, Ultrasonics, the low and high intensity applications, M. Dekker Inc. N.Y., 169, (1973).

31. D. Ensminger, Ultrasonics, the low and high intensity applications, M. Dekker Inc. N.Y., 182-197, (1973).

32. H. S. Tuan and C. M. Li, "Rayliegh wave reflection from groove and step discontinuities", J. Acou. Soc. Am., 55, 1212-1217, (1974).

33. H. S. Tuan, "On bulk waves excited at a groove by Rayleigh waves", J. App. Physics, 46, No. 1, 36-41, (1975).

34. W. Lehfeldt, "Ultrasonic testing of sheet material with Lamb waves", Material Evaluation, 4, No. 9, 331-337, (1962).

35. A. S. Matveev and M. F. Krakovyak, "New apparatus for ultrasonic flaw detection in thin walled tubing", Trudy Tsentr. Nauchro. Issled. Inst. Tekhn. Mash, 33, 26-37 (1962).

36. W. P. Mason and R. N. Thurston, Physical Acoustics, Acad. Press, Vol. X, 17, (1973).

37. L. M. Brekhovskikh, Waves in layered media, Acad. Press, 486-488, (1960).

38. L. M. Brekhovskikh, "Surface waves confined to the curvature of the boundary in solids", Sov. Phy. Acoustic, 13, No. 4, 462-472, (1968).

39. M. Abramowitz and I. A. Stegun, Handbook of Mathematical Functions, Dover Publication, (1972).

40. B. Chick, G. Anderson and J. Truell, "Ultrasonic attenuation unit and its use in measuring attenuation in alkali halides", J. Acou. Soc. Am., 32, 186-193, (1960).

41. E. P. Papadakis, In "Physical acoustics", (W. P. Mason and R. N. Thurston eds.), Vol.XII, 278-289, (1976).

42. K. R. Chaplain, "Elastic constant measurements at high temperatures", Ph.D. Thesis, Dept. of Elec. and Elect. Eng., University of Aston in Birmingham, (to be submitted).

43. J. F. W. Bell, "The velocity of sound in metals at high temperatures", Phil. Mag., 2, 1113, (1957).

44. J. F. W. Bell and P. J. Kalmarczie, "The end resonance of strips and plates", Physics Letters, 61A, No. 2, 91-93, (1977).

45. L. Pochhammer, "Uber die Fortpflanzungsgeschwindigkeiten Kleiner Schwingungen in einem unbergerenzten isotropen Kreizytinden", J. f. d. reine u. angew Math., Vol.81, 324-326, (1876).

46. C. Chree, "The equation of an isotropic elastic solid in polar and cylindrical co-ordinates", Trans. Camb. Phil. Soc., 14, 250-369, (1889).

47. D. Bancroft, "The velocity of longitudinal waves in cylindrical bars", Physical Review, 59, 588-593, (1941).

48. J. F. W. Bell, A. E. Noble and T. N. Seth, "Graphical displays of acoustic properties of solids", Ultrasonic, 178-181, (1973).

49. R. T. Folk, "Time dependent boundary value problems in elasticity", Ph.D. thesis, Lehigh University, Bethlehem, (1958).

50. R. D. Mindlin and D. G. Gazis, "Extensional vibrations and waves in a circular disk and a semi-infinite plate", J. App. Mech., 27, 541-547, (1960).

51. R. W. Morse, "Dispersion of compressional waves in isotropic rods of rectangular cross section ", 20, 6, 833 -838, (1948).

52. M. D. Waller, "Vibration of free circular plates", Physical Soc., 50, PT.1, 70-76, (1937).

53. S. D. Poisson, "Memoire sur l'equilibre et le mouvement des corps elastiques", Memoire de l"Academic de Paris, Vol. 8, (1829).

54. J. S. Uflÿand, "Rasprostranenie voln pri poperetchnydeh kolebaniyakh streshney i plastin", Prickel Mat. Mech., 12, 287, (1948).

55. R. D. Mindlin, "Influence of rotary inertia and shear on flexural motion of isotropic elastic plates", App. Mech., 18, 1, (1951).

56. G. Martincek, "The determination of Poisson's ratio and the dynamic modulus of elasticity from the frequencies of natural vibration in thick circular plates", J. Sound. Vib., 2, 116-127, (1965).

57. W. P. Mason, "Electromechanical transducers and wave filters", D. Van Nostrand Co. Inc., N.Y., (1948).

58. R. A. Johnson and R. S. Teske, "A mechanical filter having general stopband characteristics", IEEE Trans. Sonics and Ultrasonics, Vol. SU-13, 41-48, (1966).

59. G. Ambati, "An experimental and theoretical investigation into the acoustic spectra of solids having cylindrical symmetry", Ph.D. thesis, Dept. of Elec. and Elect. Eng., University of Aston in Birmingham, (1976).

60. D. S. Kupperman and D. Yuhas, "Evaluation of ceramic turbine blades with an acoustic microscope", The Am. Soc. for NDT, (to be published June 1979).

APPENDIX 1

This section describes an electronic system to identify the nodes along the edges of a strip resulting from the standing waves.

A magnetostrictive wire probe is used to observe the signal along the edge and is connected to the 'x' input of an oscilloscope. A delay and sample circuit is used to gate part of the echo decrement signal which is applied to the 'y' input of the oscilloscope. This gives a 'clean' Lissajou figure on the display. As the probe samples the signal across a node, the signal falls to zero and then reverses phase. Thus by counting the number of phase changes along the edge, the number of nodes is determined. Precise tuning is necessary to make phases and zeros well defined.

The operation of the electronic circuit will not be described in detail, however, the schematic circuit diagram and the waveform at various points are shown in Figures A.1 and A.2, respectively.
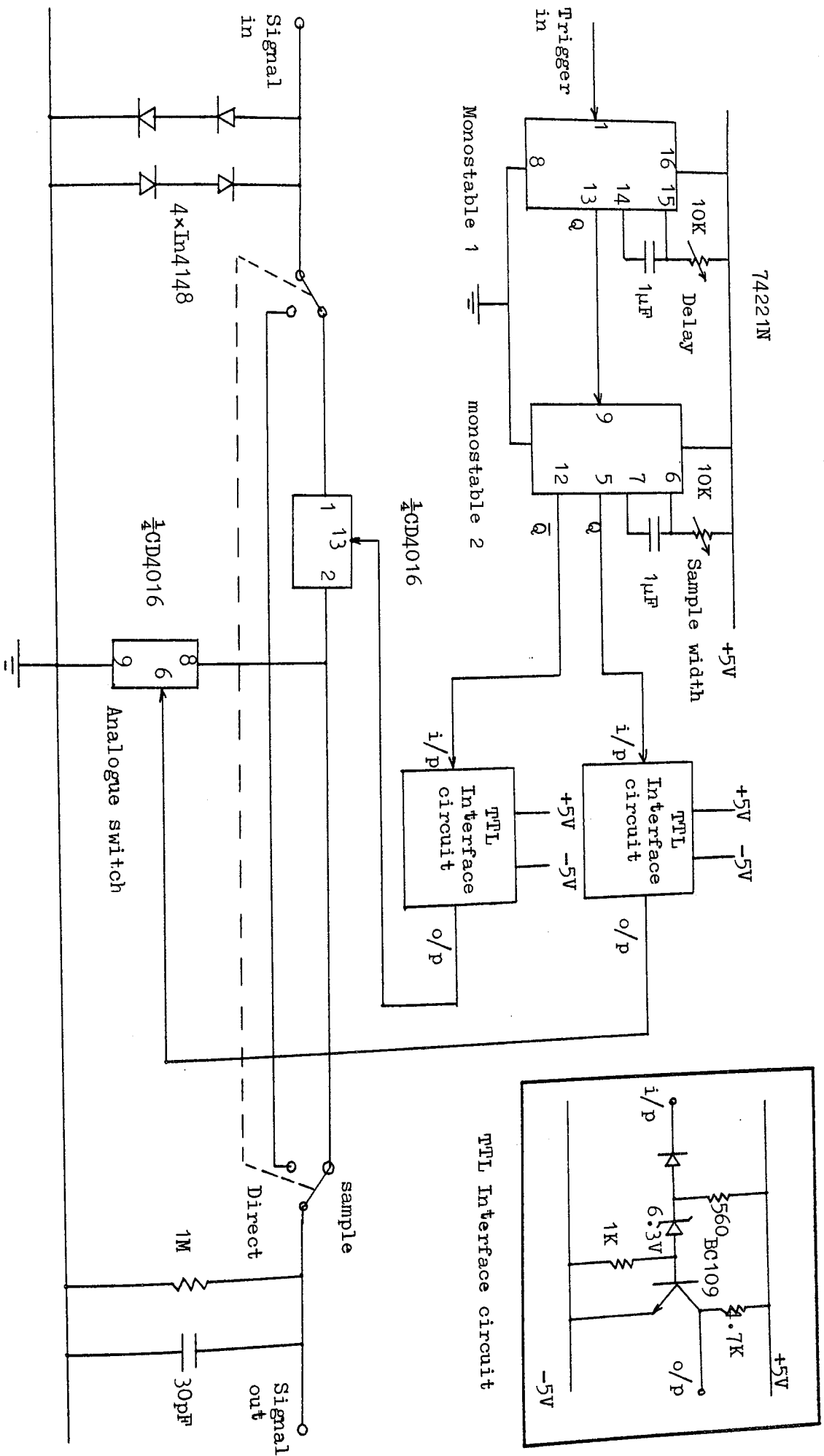
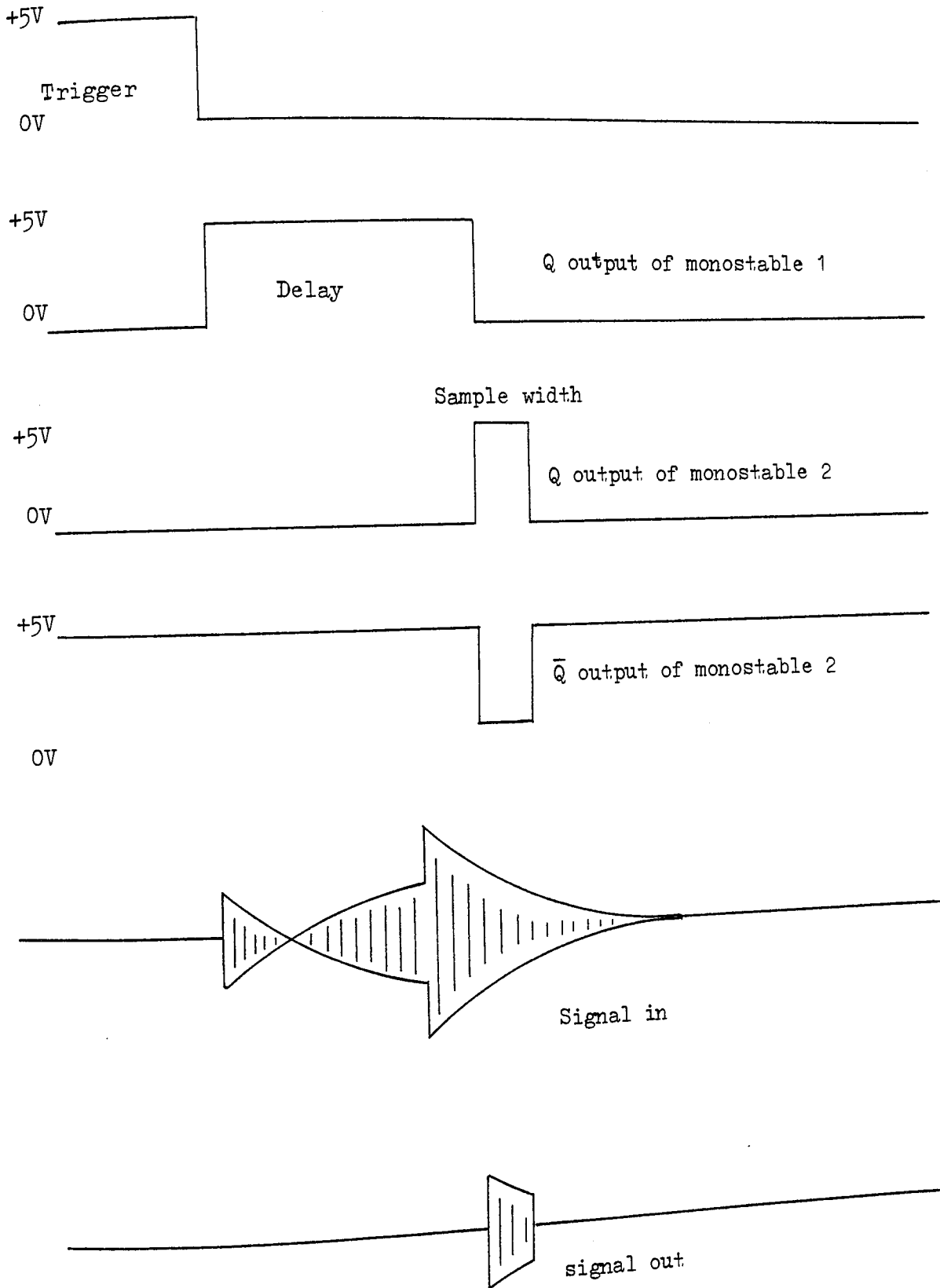Figure A1.1 Circuit diagram of the gate and sample system.

+5V

Trigger

0V

+5V

Delay   Q output of monostable 1

0V

Sample width

+5V

Q output of monostable 2

0V

+5V

$\bar{Q}$ output of monostable 2

0V

Signal in

signal out

Figure A1.2   Waveforms at various points of the circuit shown in fig. A1.2.

APPENDIX 2

From equation (4.10)

$$\frac{M_n(\Omega_1)}{n} \simeq (1+\mu_o) \exp(-\mu_o) \exp\{-n(\mu_o-\mu_1-\alpha_o+\alpha_1)\}$$

This is valid for $n > \Omega_1$ and $n \geqslant 100$ only.

Let

$$F(k) = \exp\{-n(\mu_o-\mu_1-\alpha_o+\alpha_1)\} = \exp\{G(k)\} \qquad (A2.1)$$

where $k \qquad = 1/n$

$$\cosh\alpha_o = n/\Omega_1$$

$$\cosh\alpha_1 = (n-1)/\Omega_1$$

$$\mu_o \qquad = (1-R_1^2)^{\frac{1}{2}}$$

$$\mu_1 \qquad = \frac{(n^2\mu_o-2n+1)^{\frac{1}{2}}}{n-1}$$

$$\alpha_o \qquad = \log_e(\frac{1+\mu_o}{R_1})$$

$$\alpha_1 \qquad = \log_e\{\frac{n-1}{nR_1} + \frac{(n^2\mu_o^2-2n+1)}{nR_1}\}$$

The function $G(k)$ will have a Maclaurin's series and can be expressed as

$$\delta_o+\delta_1 k+\delta_2 k^2+\ldots\ldots\ldots$$

Therefore

$$\mu_1-\mu_o+\alpha_o-\alpha_1 = \delta_o k+\delta_1 k^2+\delta_2 k^3+\ldots\ldots\ldots \qquad (A2.2)$$

The coefficients δ_0, δ_1, δ_2,...... can be obtained by successive differentiation in equation (A2.2) with respect to k and taking the limit k→0. This produces

$$\delta_0 = \mu_0$$

$$\delta_1 = \mu_0 - \frac{1}{2\mu_0} \qquad\qquad (A2.3)$$

$$\delta_2 = \mu_0 - \frac{1}{2\mu_0} - \frac{1}{6\mu_0^3}$$

Substituting equation (A2.3) in (A2.1) gives

$$F(k) = \exp(\mu_0)\,\exp(\delta_1 k + \delta_2 k^2)$$

$$\qquad\qquad (A.24)$$

$$\simeq \exp(\mu_0)\,(1 + \delta_1 k + \delta_2 k^2 \ldots\ldots)$$

Therefore $\dfrac{M_n(\Omega_1)}{n}$ can be expressed into a polynominal form by putting equation (A2.4) in (4.10), this gives

$$\frac{M_n(\Omega_1)}{n} \simeq (1+\mu_0)\left(1 + \frac{\delta_1}{n} + \frac{\delta_2}{n^2} + \ldots\ldots\right)$$